DETECTION OF ULTRASONIC LAMB WAVES IN PAPER USING AN OPTICAL MEMS MICROPHONE

A Thesis
Presented to
The Academic Faculty

by

Uri Rainisch

In Partial Fulfillment
Of the Requirements for the Degree
Master of Science in Mechanical Engineering

Georgia Institute of Technology

August 2004

DETECTION OF ULTRASONIC LAMB WAVES IN PAPER USING AN OPTICAL MEMS MICROPHONE

Approved by:

Dr. Yves H. Berthelot, Advisor

Dr. F. Levent Degertekin

Dr. Emmanuel Lafond

Date Approved: August 10, 2004

ACKNOWLEDGEMENTS

I wish to express my deepest gratitude to Dr. Yves Berthelot, for being an incredibly dedicated thesis advisor and a truly inspirational mentor. The lessons I have learned from you go far beyond the scope of this work and will always guide me in my professional Engineering career. Thank you for your dedication and candor – they have been very much appreciated. To Neal Hall, extending your knowledge of the subject matter to me and your many hours of assistance in the lab I am especially grateful for. I wish you the best in all your future endeavors. I would also like to thank my beautiful parents, their nurturing support have given me the confidence to challenge myself. My greatest dream is to make you proud of me. Thank you for devoting every waking moment to your children – you have given us more than you can ever imagine. I must also thank my brother Gabi and sister Vered. Thank you for motivating me to complete this work.

TABLE OF CONTENTS

LIST OF FIGURES

SUMMARY

Laser ultrasonics has been used to measure the bending stiffness of paper products by measuring the dispersion of ultrasonic plate waves. In laser ultrasonics, ultrasound can be generated by absorption of pulsed laser spot while detection can be carried out by Laser Doppler Interferometry. The research presented in this paper describes a new method to detect ultrasonic plate waves using a recently developed acoustic transducer, more specifically an optical Micro ElectroMechanical System (MEMS) microphone with broadband capability. The MEMS device operates as a non-contact proximity probe placed less than ¼ of a millimeter away from the plate. The signals are detected with a capacitive micromachined ultrasonic transducer (cMUT) in which the back electrode of the capacitive transducer on a transparent substrate is shaped as an optical diffraction grating. The displacement of the transducer membrane is determined using an optical interferometer. By applying voltage to deflect the membrane electrostatically, the detection sensitivity is kept at an optimum level.

The main purpose of the research presented herein was to test this MEMS's ability to detect ultrasonic waves propagating through paper, to increase the signal-to-noise ratio (SNR), and to calibrate the device in order to quantify the limitations on sensitivity in the context of the detection of ultrasound in paper. Similar tests were conducted for comparison with a modified Mach-Zehnder Interferometer, a more traditional method used for laser ultrasonic detection, and its results are presented in this paper.

CHAPTER 1

INTRODUCTION

Non-contact measurements of ultrasound in paper have been made in the past using laser ultrasonics. [1][2][5][19][34] Laser Interferometry and other optical techniques for detection of ultrasound is however expensive and delicate. Recently, capacitive micro-machined ultrasonic transducers (cMUTs) have become a viable alternative to piezoelectric devices for nondestructive testing and medical ultrasound imaging applications. [3][4][45] In this paper, we assess the potential of using cMUTs as an alternative to laser detection of ultrasound.

In capacitive microphone applications, capacitance change is measured under constant charge conditions using high input impedance amplifiers. Although this approach provides a detection scheme that is sensitive in the audio range, the electronic noise generated is a major limitation for ultrasonic frequencies. Dr Degertekin, at The Georgia Institute of Technology has developed recently a low noise optical microphone using cMUT technology. [3][4] This new device appears to be very promising in the context of ultrasonic detection of Lamb waves. The displacement of the microphone diaphragm is measured optically within the device by means of a diffraction grating.

The potential for such a transducer is enormous because of the large number of sensors that can be put on a single MEMS wafer. At ultrasonic frequencies, each transducer would be able to sample spatially the ultrasonic field. Array processing would offer rich information extracted from an ultrasonic field. Paper manufacturers and other industries producing planar material such as sheet metal or composites could benefit from

such a transducer. Currently paper quality is measured off the assembly line in a destructive process, which is notoriously unreliable at low basis weights (<100 g/m^2). If this process could be done online and nondestructively, adjustments in the manufacturing process could be made quicker and at lower cost.

To test this device an experimental setup and procedure was undertaken by Uri Rainisch in Dr. Yves H. Berthelot's Laser Ultrasonics Laboratory in the School of Mechanical Engineering of the Georgia Institute of Technology from February 2003 through May 2004. The experimental setup used a Nd: YAG pulsed laser for wave generation in paper. The resulting out-of-plane motion was optically detected by a cMUT and Helium-Neon laser. Data was collected from the broadband microphone at various stand-off distances from the paper surface and at various source-to-receiver distances from the generation point. Similar tests were conducted for comparison using a more traditional method of interferometric ultrasonic detection, specifically a modified Mach-Zehnder Interferometer, with an Argon-Ion Laser.

These results and experimental procedure are presented in this thesis which is organized as follows. Chapter 2 will discuss Lamb waves, non-contact transducers, and introduce the optical MEMS sensor that was tested. Chapter 3 describes the experimental setup and procedure to test the MEMS device and the experimental arrangement used to detect Lamb waves using the laser interferometer. Chapter 4 presents results obtained from both the MEMS and Interferometer testing and compares the two. Finally, Chapter 5 provides conclusions and recommendations for future work.

CHAPTER 2

BACKGROUND INFORMATION

2.1. Lamb Waves In Paper

Lamb waves are elastic waves in plates. The propagation of Lamb waves in plates is in general very complicated. [14][38][46] When the plate thickness is less than the wavelength propagating through the plate only two types of Lamb waves are present. [40][44] These two basic types of Lamb-wave modes are symmetrical and antisymmetrical. They are referred to as S_0-mode and the A_0-mode, respectively. In the S_0 mode, the normal displacement at the free boundaries is symmetric with respect to the midline; in the A_0-mode, the normal displacement is antisymmetric with respect to the midline. Figure 2.1.1 shows illustrations of these two modes.

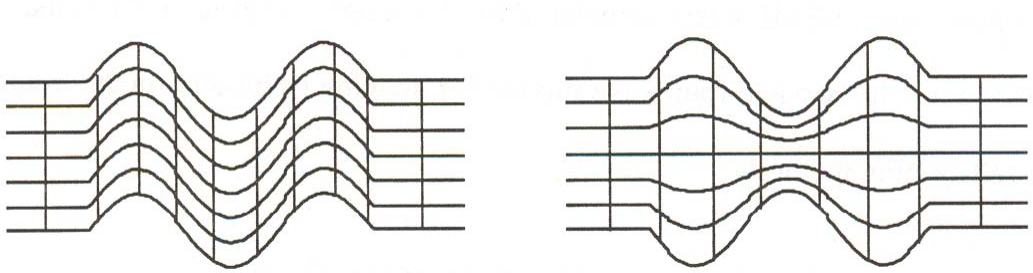

Figure 2.1.1 Illustrations of the two basic types of Lamb Waves: A_0 and S_0, and their behavior with respect to the midline of planar material they propagate in. [10]

The S_0-mode is characteristic of a compressional wave whereas the A_0-mode corresponds to a flexural wave or bending wave. The S_0-mode propagates at a fast,

constant velocity in a non-dispersive manner, and the A_0-mode propagates dispersively at a velocity that increases with frequency, as seen in Figure 2.1.2. More complicated modes, or higher order modes, of propagation can exist when the plate becomes thick in comparison to the wavelengths of the Lamb waves propagating in the plate. [41][43] In the work reported in this paper we are interested in showing a capacitive micro-machined ultrasonic transducer's ability to detect both the S_0-mode and the A_0-mode Lamb waves in paper. Figure 2.1.2 demonstrates Lamb wave velocity curves obtained in research performed by the Institute of Paper Science and Technology of the Georgia Institute of Technology in 1998. The results in Figure 2.1.2 were obtained using plate theory, for the same type of paper (Raw Stock 59) used in the research that will be presented in this thesis.

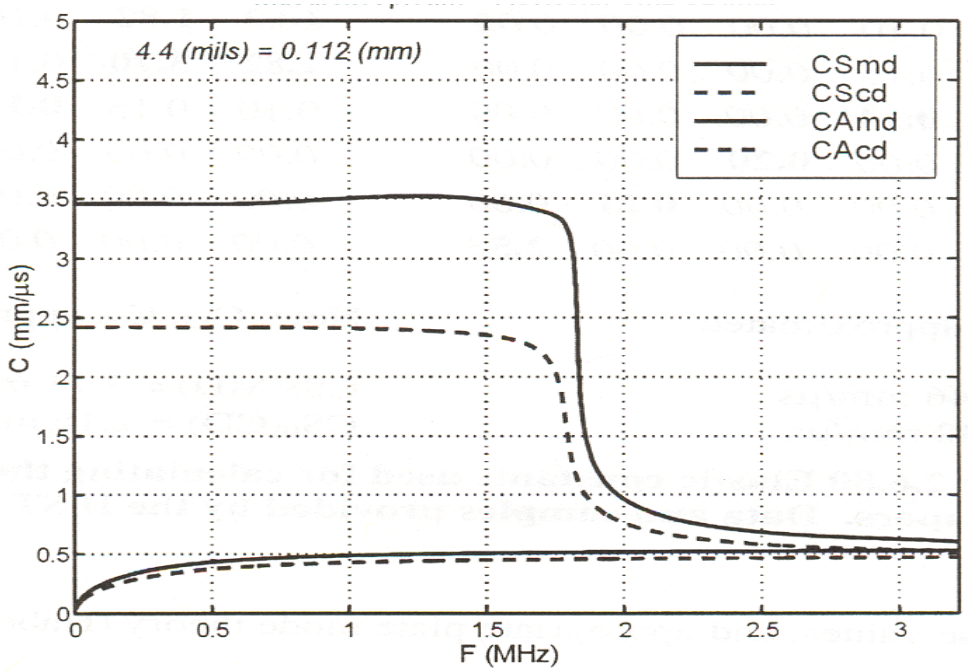

Figure 2.1.2. Calculated A_0 and S_0 mode velocities for Raw Stock Paper 59 in the machine direction and cross direction from research performed in 1998 by the IPST of the Georgia Institute of Technology. [10]

During paper production there can be local variations in density, thickness, and occasional cases of fiber clusters. All of these trends have a significant effect on the variability of ultrasonic waveforms in paper. Using plate mode theory however, paper can be modeled as an orthotropic plate and the phase velocity curves of the various modes can be calculated. [11][25][31] The model involves nine elastic constants, which can be expressed in terms of a Young's modulus, a shear modulus, and a Poisson ratio in each of the three principal directions, machine direction (MD), cross direction (CD), and thickness direction (ZD). [29][30][32][33] The MD is the direction the paper traveled when it was manufactured in the paper machine. The ZD crosses through the plane in which the paper lies and the CD direction is perpendicular to both the MD and ZD.

In this thesis, we consider only wave propagation in the MD direction. Most of the wood fibers in paper are arranged in the machine direction; therefore, both compressional waves and flexural waves will propagate more easily and faster in this direction. [35] This phenomenon of higher propagation velocities for both the A_0 and S_0 modes in the machine direction is depicted in Figure 2.1.2.

Despite the A_0 mode's slow propagation speed with respect to the S_0 mode, the A_0 mode is more easily detected than the S_0 mode. The reason for this is that the A_0 mode has much more Lamb wave energy and generates very large out-of-plane displacements in comparison to the S_0 mode, which exhibits smaller amplitude waveforms. [23][42]

The equation used to predict the phase velocity of an A_0 mode Lamb wave in paper is given in [11] as:

$$C_{ph}^{\ 4} + \omega^2 (D/SR) C_{ph}^{\ 2} - \omega^2 (D/BW) = 0 \qquad (2.1)$$

where,

C_{ph} = phase velocity

ω = Angular frequency

BW = basis weight (mass/area)

D = flexural rigidity (Nm)

SR = shear rigidity (N/m).

Equation 2.1 assumes that the plate behaves in simple bending only, without rotary inertia. The group velocity is the speed at which energy in a group of waves, centered at given frequency, travels. [24] The phase velocity C_{ph} is defined as ω / k, where k is the wave number. The group velocity is defined as $C_{gr} = d\omega / dk$. [8] By replacing phase velocity in equation 2.1 with ω / k and using the following substitutions: a=BW/D, b=BW/SR, one can rewrite the dispersion equation as:

$$k^4 - k^2\omega^2 b - a\omega^2 = 0 \tag{2.2}$$

Using the quadratic equation to find k^2, and solving for the positive root, one arrives at the solution for k:

$$k = \sqrt{.5(b\omega^2 + \sqrt{b^2\omega^4 + 4a\omega^2})} \tag{2.3}$$

Differentiating with respect to ω and inverting the solution one obtains the group velocity:

$$C_{gr} = \frac{d\omega}{dk} = \frac{\sqrt{2}\sqrt{b\omega^2 + \sqrt{b^2\omega^4 + 4a\omega^2}}}{\omega b + \dfrac{b^2\omega^3 + 2a\omega}{\sqrt{b^2\omega^4 + 4a\omega^2}}} \tag{2.4}$$

Taking the limit as the frequency gets small, equation 2.4 reduces to:

$$C_{gr}\Big|_{\omega\to 0} \propto \frac{2\sqrt{\omega}}{a^{1/4}} = 2\sqrt{\omega}\left(\frac{D}{BW}\right)^{1/4} \tag{2.5}$$

Equation 2.5 approximates a pure bending wave which has a square root dependency on frequency. Figure 2.1.3 presents the group phase velocities of equation 2.4 and 2.5. The phase velocity curves of Figure 2.1.3 were calculated using the same material properties of the paper (raw stock 5914-3) that was used for testing in this research. This type of paper has a flexural rigidity of 8.67×10^{-4} Nm in the MD, a shear rigidity of 26,200 N/m in the MD, and a basis weight of .087 kg/m^2. Figure 2.1.3 is therefore a good predictor for the type of A_0 Lamb wave behavior one might expect to see for this type of paper used in our experimental trials. The difference between the group velocities of equations 2.4 and 2.5 only begin at a frequency of about 20 kHz. Making use of equation 2.5 for further analysis at low frequencies in this thesis is quite suitable.

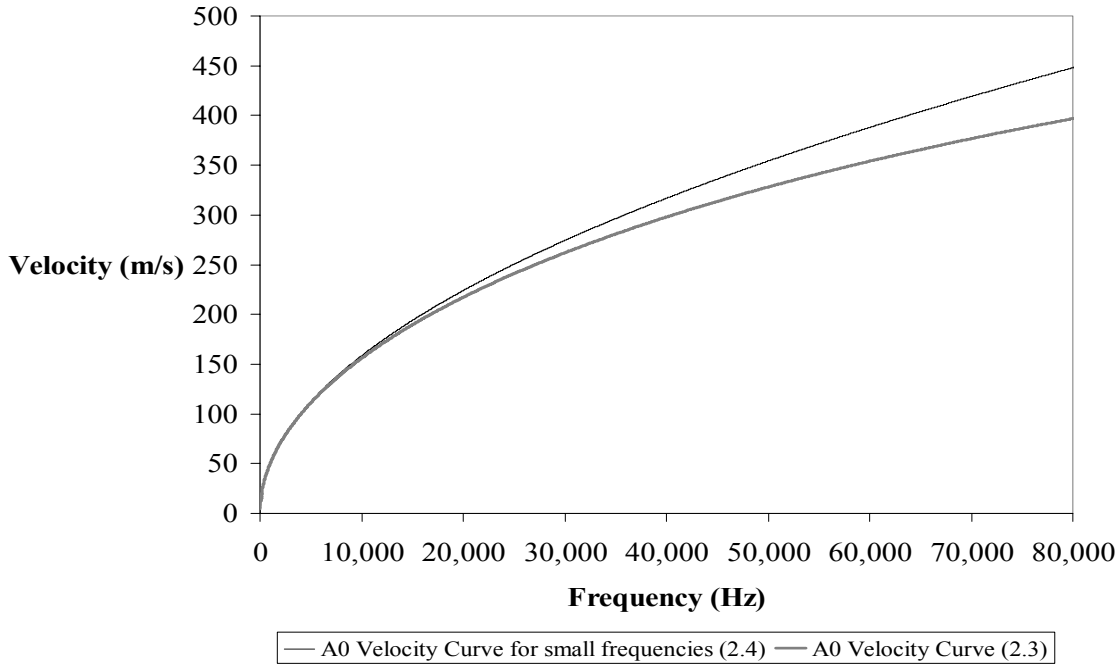

Figure 2.1.3. Calculated A_0 group velocity curves in the MD based on equations 2.4 and 2.5, assuming simple bending for raw stock paper 5914-3.

Plate wave theory states that the wave equation which governs the dynamic behavior of a flat plate is a fourth order differential equation spatially and second order temporally, as written in equation 2.6.

$$\frac{\partial^4 w}{\partial x^4} + \alpha^2 \frac{\partial^2 w}{\partial t^2} = 0 \tag{2.6}$$

where: $\alpha = \dfrac{12}{h^2 C_l^{\,2}}$

where, $h =$ plate thickness

$$C_l = \sqrt{\frac{E}{\rho(1-\upsilon)^2}}$$

where, $E =$ plate Young Modulus

$\rho =$ plate density

$\upsilon =$ plate Poisson ratio.

When trial solutions of the form $e^{\pm i\omega t}$ are plugged into equation 2.6 one arrives at a solution: equation 2.7, which is a solution only when the relationship for β, equation 2.5, is true.

$$W(x,t) = W_0 e^{i(\omega(t - x/\beta))} \tag{2.7}$$

where: $W_0 =$ wave amplitude at time zero

$\omega =$ angular frequency

$t =$ time

$x =$ distance wave propagates

$\beta = \sqrt{\omega}\left(\dfrac{D}{BW}\right)^{1/4} =$ phase velocity

Predicted A_0 Lamb Waveforms in Paper

Equation 2.7 can be used to predict A_0 Lamb wave behavior as a function of time, t, and at some arbitrary distance, x, from the point at which the wave was generated. Appendix A contains the computer program developed in Matlab to create A_0 Lamb waveform models.

Two assumptions were made generating predicted A_0 waveform models, both of which involve the input signal. First, the input signal was assumed to be a half cycle of a sine wave, of a 5 μs duration. There is no point in digitizing the signal at higher time step interval since a time scale of 5 μs corresponds to a frequency scale of 200 kHz which is already beyond the frequency range of interest. The second assumption regarding the input signal was that it is made up of sine waves with frequencies from 3 kHz to 500 kHz that are multiples of 3 kHz. All the input frequencies were given the same magnitude. The first assumption is reasonable because the actual input signal to the paper during experimental testing was provided by a laser pulse that released a laser beam in the form of a step function. The second assumption is very questionable. What frequencies and their corresponding amplitudes were created on the paper at the point where the input signal impinged the paper could not be determined. Cutting off the input frequency at 500 kHz was necessary to reduce computation time and is a reasonable cutoff because an A_0 wave signal at a frequency greater than 500 kHz propagates at roughly the same velocity as an A_0 wave at 500 kHz, as seen in Figure 2.1.2.

Figure 2.1.4 presents a predicted A_0 Lamb waveform in Raw Stock 5914-3 paper based on equation 2.7. This Lamb wave in Figure 2.4 is a waveform that would result at

a propagation distance of 26 mm. The non-zero early part of the waveform is a non-physical artifact of the method used to synthesize the signal via Fourier Transform and inverse Fourier Transform. Predicted A_0 waveforms at other propagation distances were generated using the same computer program and are included in Appendix B. The frequency arrival time plot, Figure 2.1.5, of the waveform in Figure 2.1.4 shows that the higher frequencies travel at a faster velocity, and arrive at the receiver before lower frequencies.

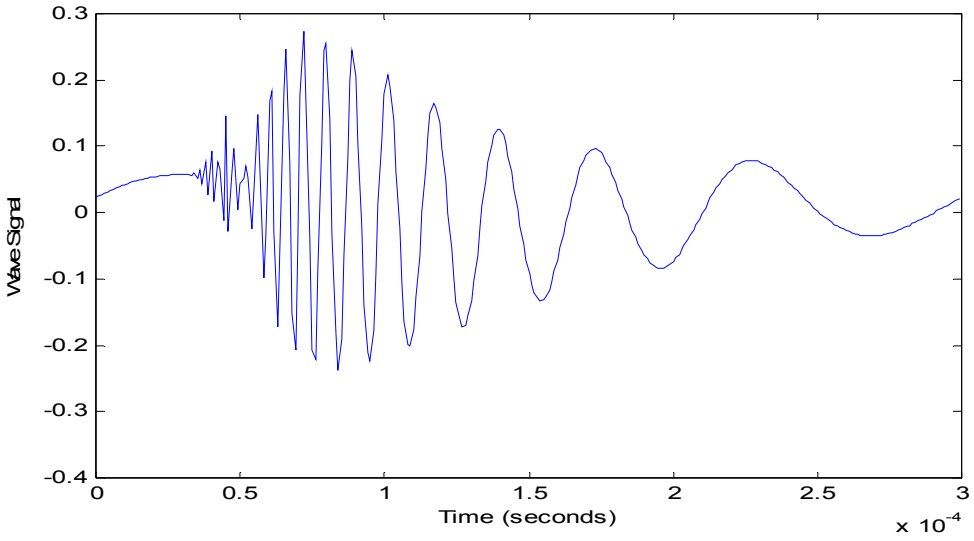

Figure 2.1.4. Predicted A_0 Lamb wave in Raw Stock 5914-3 paper at a propagation distance of 26 mm. This waveform was based on equation 2.7 and was formulated by use of a Matlab program, see Appendix A.

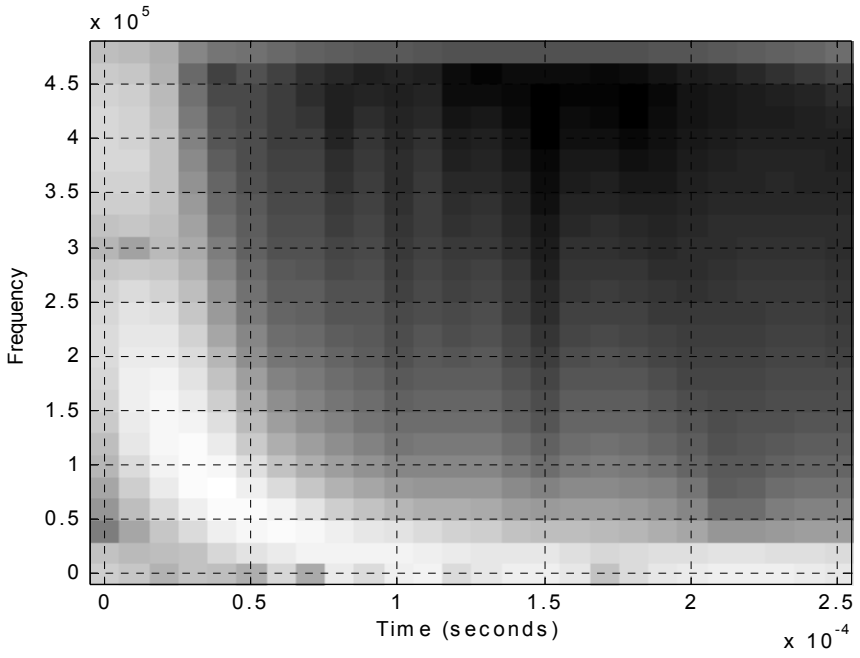

Figure 2.1.5. Frequency arrival time for A_0 Lamb wave, presented in Figure 2.1.4, for Raw Stock 5914-3 paper at a propagation distance of 26 mm. The shading indicates the presence of energy at the given frequencies: where the color black indicates no energy and the color white indicates a high energy of a particular frequency.

2.2. Non-Contact Methods for Lamb Wave Detection

In the past, off line mechanical testing of paper production has been considered an adequate method for quality control. There is however a growing awareness of the need to introduce continuous on-line monitoring of product quality in order to improve the process of the paper making machine. Lamb wave detection is one methodology to continuously monitor paper quality. [26][27][28] The three predominant techniques used to generate and detect Lamb waves in paper have been: contact transducers, laser interferometry, and non-contact transducers. Despite their high sensitivity Contact transducers, such as piezoelectric devices, suffer from the fact that in some cases they

cause damage to the paper sample being tested (i.e. leaving marks). Our research focuses on characterizing one type of non-contact transducer and comparing its capabilities with a laser interferometer, more specifically a Mach-Zehnder interferometer.

Laser interferometry does not adversely affect the dynamics of the system it is testing. This is particularly useful when the attachment of a transducer to a test specimen is not practical due to heat, distance, motion, etc. Another benefit of laser interferometry is that the measurement point may be moved rapidly without the need of removing and reattaching a transducer to the test specimen. Light beams used with the laser interferometers can be made extremely small to give good access in confined spaces. Small laser spots also give laser interferometers an exceptionally high resolution, both spatially and temporally. Nevertheless, further work is being done to improve the sensitivity of laser techniques for measuring ultrasonic fields and waves. Smaller size lasers, higher powers, greater stability, longer coherence, and a larger choice of wavelengths are many of the enhancements laser interferometric systems are going through to improve their performance [5][22].

Electromagnetic acoustic transducers (EMATS) are one form of non-contact transducers. A current is induced to flow in a coil in the surface of the EMAT transducer. A solenoid is also placed at the surface of the transducer to generate a magnetic field perpendicular to the flow of the current. A force is thus exerted on the coil carrying the current. This localized stress field is arranged so that movement of the surface being tested causes an electromagnetic force to be induced in the sensing coil. EMATS are sensitive to velocity rather than displacement. Two negative aspects of EMATS are one, that they suffer from resonance and narrow bandwidth problems; because the transmitter

and receiver coils are inductive their impedance increases with frequency, making them more difficult to use above a few megahertz. Two, EMATS are restricted to testing surface layers that are conductive due to the electromagnetic forces required to induce the sensing coil. Paper does not offer a highly conductive testing surface.

Another form of non-contact transducers used for Lamb wave detection in paper are capacitive transducers [3][20][21]. These transducers are perhaps the most closely comparable in performance with laser interferometers. Capacitive transducers and EMATS may be non-contact transducers, but they must be very close to the surface being tested, less than a millimeter in some cases. Capacitive transducers consist of a conducting plate placed very close to the surface to form an electric capacitor, whose capacitance depends upon the separation of the plate from the test surface. For a constant charge, the voltage across the capacitor varies with the separation distance between the paper sample and the transducer, thus measuring the movement of the surface being tested. These transducers are mainly limited by the often poor coupling of energy between the transducer and the paper due to the large air and paper impedance mismatch. This problem is augmented even more with papers of thickness less than .4 mm. [5]

2.3. Optical MEMS Sensor

In the research presented in this thesis a non-contact acoustic transducer designed and built in Dr. Degertekin's lab was used to detect ultrasonic Lamb waves in paper. This acoustic transducer was a type of MEMS device, specifically a capacitive micromachined ultrasonic transducer (cMUT). The cMUT uses a phase-sensitive

diffraction grating embedded on the back side of the transducer to relay detection information, see Figure 2.3.1. The bottom electrode on the substrate forms the reference fingers, the membrane serves as the ultrasonic wave detector and as the reflector for the incident laser beam, illustrated in Figure 2.3.2.

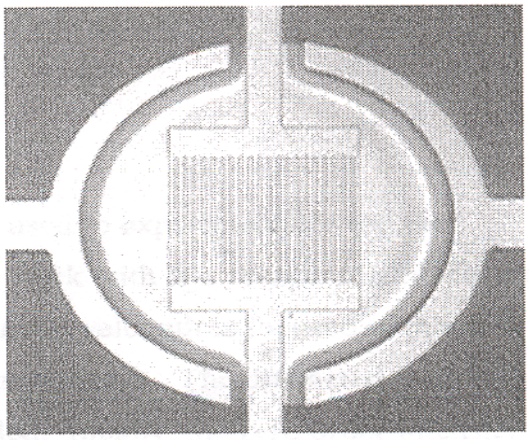

Figure 2.3.1. The backside view of a 200 μm diameter cMUT with integrated diffraction gratings. The grating has ten fingers, one every 4 μm. Each finger is 2 μm wide.

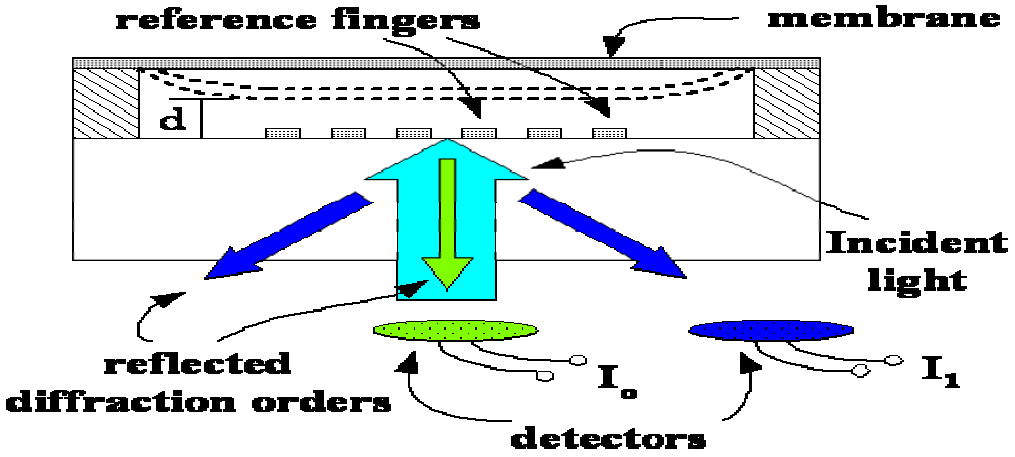

Figure 2.3.2. Side view illustration of a cMUT demonstrating the optical technique used for acoustic detection. The varying gap height between the detection membrane and the diffraction fingers is denoted by the letter, d, and the dotted lines represent the possible positions the detection membrane may move to due to either acoustic or electrostatic actuation.

Since the substrate is transparent, the grating can be illuminated from the backside allowing the integration of optoelectronics. When a coherent light source illuminates the backside of the cMUT through the transparent substrate the reflected field will split into odd diffraction orders due to light amplification and cancellation. [39] When the vertical distance between the reference and moving grating fingers is an odd multiple of $\lambda/8$, where λ is the optical wavelength in air, optimal interferometric sensitivity is reached. The zero order beam acts like a perfect mirror for an incident beam when the gap distance is an even multiple of $\lambda/4$. For this reason optical information was not gathered from the zero order beam, but from the first order beam. Other higher order beams could have been used for detection during experimentation, but because the first order beam had the greatest intensity next to the zero order beam, the first order beam could be more easily detected by the photodetector during experimentation. To further increase the SNR of the device by decreasing the laser noise, one could also use differential balanced detection scheme where the 0^{th} order diffraction beam is collected and subtracted from the 1^{st} order diffraction beam. According to scalar diffraction theory the intensity of the zero and first order beam, I_0 and I_1 can be expressed as [13]:

$$I_0 = I_{in}\cos^2\left(\frac{2\pi d}{\lambda}\right) \tag{2.3.1}$$

and

$$I_1 = \frac{4I_{in}}{\pi^2}\sin^2\left(\frac{2\pi d}{\lambda}\right) \tag{2.3.2}$$

where,

I_{in} = incident laser intensity

d = gap height

λ = optical wavelength of incident beam in air.

To achieve optimum sensitivity when collecting light from the first diffraction order, the membrane gap thickness must be an odd multiple of $\lambda/8$, according to equation 2.3.2. This phenomenon is graphically demonstrated in Figure 2.3.3. To achieve this optimum gap thickness the cMUT has the ability of being induced by an electric potential. See Figure 2.3.4. When induced by an electric potential the membrane gap height adjusts to equalize the electrostatic forces acting on the membrane and the diffraction fingers. Figure 2.3.2 also illustrates how the detection membrane behaves as a result of such an electric potential. When the electric potential results from a constant voltage, it is referred to as the "DC bias". When the proper DC bias is applied to the cMUT the gap height will reach odd multiples of $\lambda/8$ and the cMUT will exhibit optimum sensitivity.

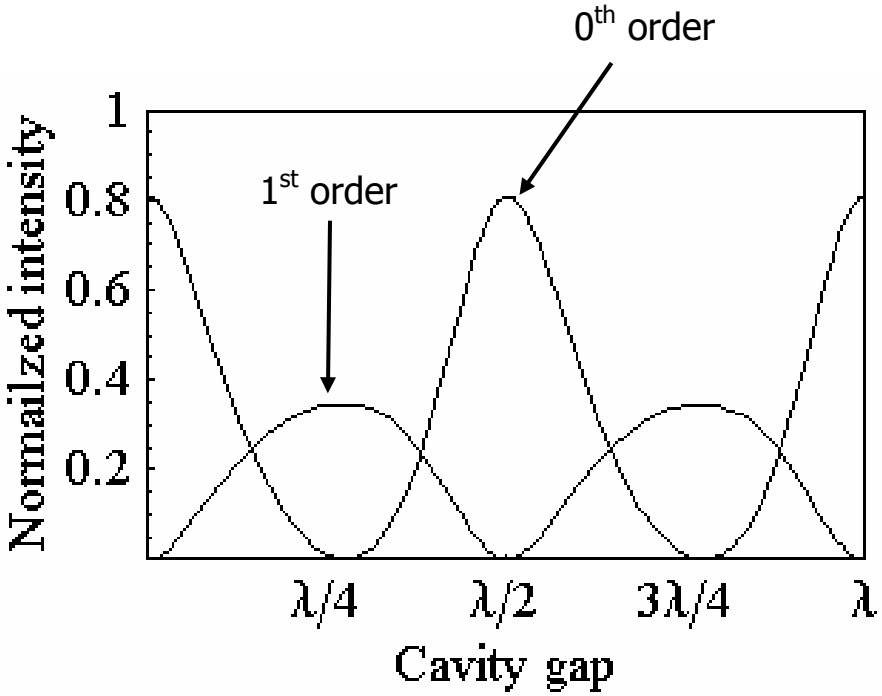

Figure 2.3.3. Intensity of the zero and first order diffraction beams normalized. The first order beam, which was the only order used in this research is maximum at gap heights that are odd multiples of $\lambda/8$.

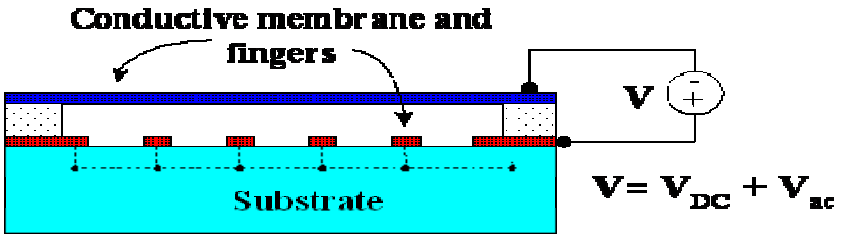

Figure 2.3.4. Side view illustration portraying how both DC bias voltage and an AC voltage can be applied to the cMUT.

The maximum DC bias permissible is limited by the gap height between the electrodes. The aluminum detection membrane would collapse if it would be displaced more than 1/3 of its fabricated gap, which is 2/3 μm, for a fabricated gap of 2 μm. [7] DC bias during testing was held under 60 Volts in order to avoid the membrane collapse.

The cMUT's electrostatic actuation capability is not only beneficial because it can bring the detection membrane to an optimum level, but also because electrostatic actuation can be used for self-calibration purposes. The calibration that was performed for this transducer will be expanded upon in Chapter 4.1 of this report.

The Lamb wave detection results were collected by a cMUT that was fabricated in March 2003 in the School of Mechanical Engineering of Georgia Institute of Technology. This cMUT was made of aluminum on a quartz substrate and placed with eight other similar transducers on a MEMS chip as seen in Figures 2.3.5 and 2.3.6. Each transducer is 160 μm in diameter and has a gap height of 2 μm between the diffraction grating and the detection membrane. The diffraction grating fingers are 2 μm wide and are spaced evenly 4 μm apart.

Epoxy 1 of 9 cMUTs Gold wire bonding

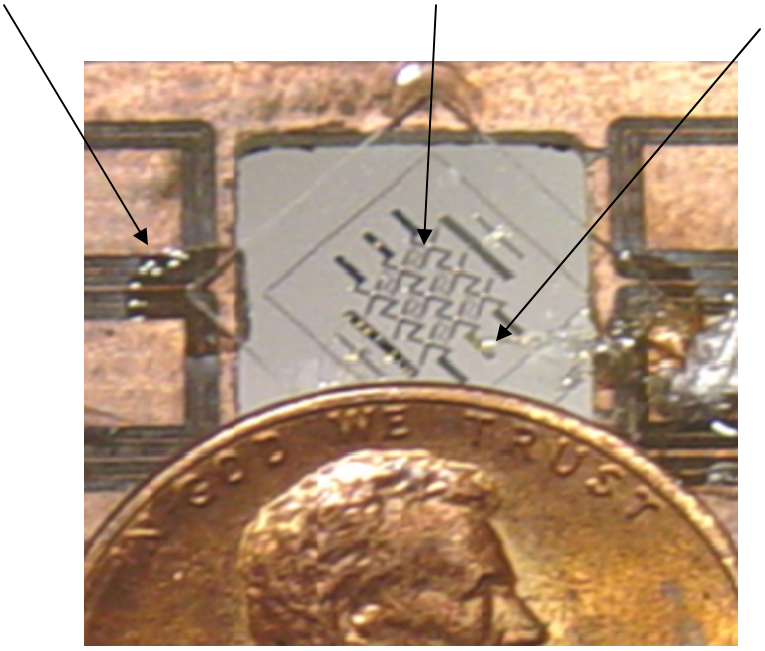

Figure 2.3.5. Front view of MEMS Chip with nine cMUTs of diameter .16mm (.0063in.).

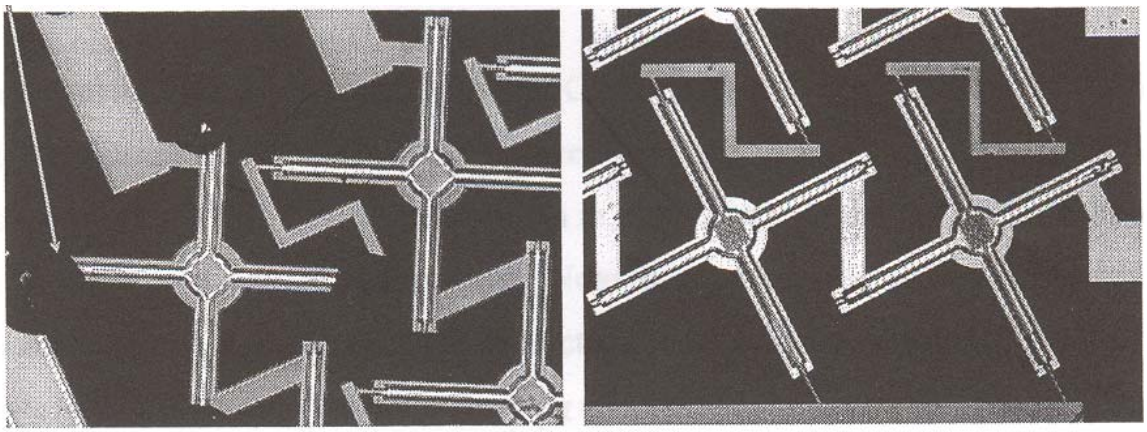

Front Back

Figure 2.3.6. Close up pictures of the front and back of 160 μm cMUTs. The lightning bolt objects connecting one cMUT's arm to another are small pieces of aluminum used to transmit electric potential to the cMUTs on the chip. [4]

CHAPTER 3

EXPERIMENTAL ARRANGEMENT

The experimental setup can be subdivided into two components: the system that generates Lamb waves, and the system that detects the resulting out-of-plane motion in paper. This chapter presents these two systems in the same order. Figure 3.1 illustrates a very simplified version of these two systems and the method used for data acquisition.

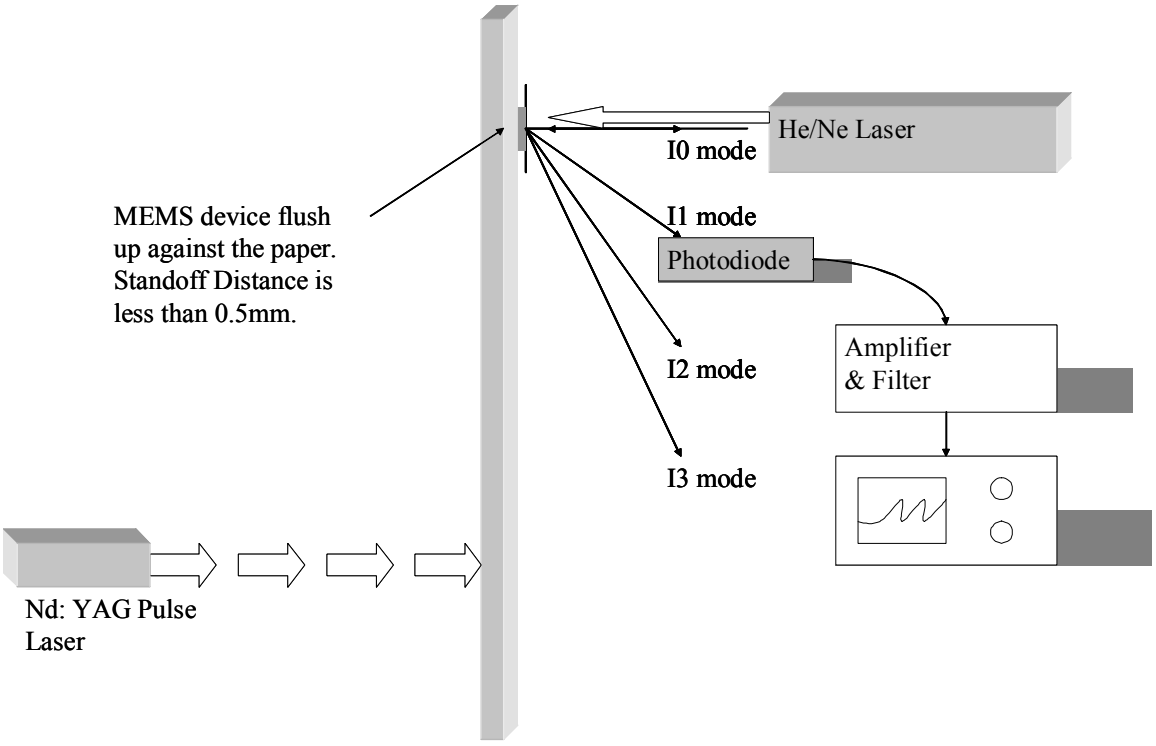

Figure 3.1. Simplified schematic of experimental setup and data acquisition method for cMUT detection of ultrasonic Lamb waves in paper.

3.1. Lamb Wave Generation

In order to induce Lamb Waves in a paper sample, a Nd: YAG, Q-switched laser with a pulse duration of 5-7 ns was used. The pulse energy at the laser head was 450 mJ at 1064 nm, with a Gaussian distribution. [36] The path the beam took once fired is depicted in Figure 3.1.1. After leaving the laser head, the beam passed through a half-wave plate, a polarizer, then bounced off two mirrors for high powered lasers until finally it passed through a convex lens, with an 8 cm focal length, that focused the beam onto the sample of paper. The second mirror for high power lasers and the focusing lens were placed on the same translation stage so that the generation spot on the paper could be moved laterally with respect to the lab bench. At the point of contact with the paper the Nd: YAG laser beam had a spot size of approximately 1 mm.

The spot size created by the Nd: YAG laser beam on the paper ranged from .9 mm to 1.3 mm in diameter. This variance was due to the necessary adjustments in the positioning of the mirrors for high powered lasers and the focusing lens to ensure that the Nd: YAG laser beam struck the paper at the same vertical position at which the cMUT was located.

Spot size was not considered a dependent variable. Many trial runs at all the previously stated spot sizes were conducted. Analysis, which will be presented later in this report show very little variance in the cMUT's detection capabilities as a result of varying Nd: YAG laser spot size.

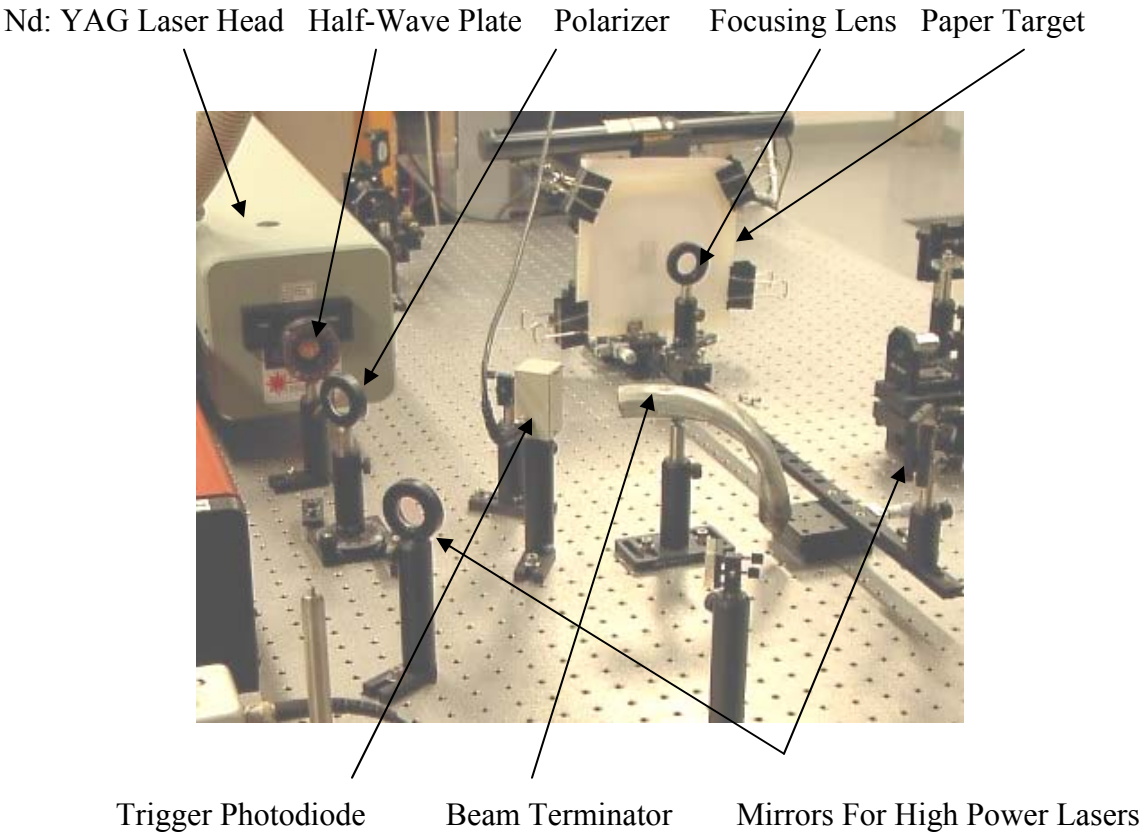

Figure 3.1.1. Experimental setup on the lab bench for ultrasonic wave generation and oscilloscope triggering.

The purpose of the polarizer and the half-wave plate was to control the amount of energy incident on the paper sample. Light leaving the laser head is horizontally polarized; rotating the half-wave plate caused a portion of the light to become vertically polarized. During this experiment the half-wave plate was rotated to 46°. The polarizer reflects any vertical component of a passing laser beam and transmits any horizontal component of a passing laser beam. [39] Without decreasing the Nd: YAG laser energy by using the polarizer and the half-wave plate, the Nd: YAG laser beam, when concentrated on a 1 mm spot on the paper, would pierce right through the paper sample.

The actual energy of the Nd: YAG laser beam just before making contact with the paper sample during experimentation was 20 mJ or 3.3 MW of power for a 6 ns pulse. This amount of energy left a mark .5 mm in diameter on the surface of the paper sample. Firing the Nd: YAG laser beam at the same point on the paper sample many times would cause the mark to grow deeper into the paper and finally after eight or more firings the laser would cut through the paper sample.

The vertical component of the laser beam that was reflected by the polarizer was directed toward a beam terminator, pointed out in Figure 3.1.1. Some of the light that traveled to the beam terminator was also scattered. A photodiode was positioned right next to the beam terminator to capture some of this scattered light. Once enough scattered light had been absorbed by the photodiode a capacitor discharge was transmitted along a BNC cable that triggered the oscilloscope to begin recording data. The remaining horizontal component of the Nd: YAG laser beam continued through the polarizer towards the paper sample.

3.2. Lamb Waves Detection with MEMS Device

Preparing the cMUT and other components involved on the optical lab bench for detecting ultrasonic Lamb waves in paper was carried out prior to aligning the Nd: YAG laser system. The reason for this order in operations was that it was easier to realign the target location and spot size of the Nd: YAG laser beam than to realign the cMUT and the incident beam upon the cMUT.

A square piece of paper, specifically raw stock 5914-3, 17 cm^2 and .11mm thick, was clamped into a plastic frame of roughly the same height and length. See Figure 3.1.1. One side of the plastic frame was then bolted onto a 13 mm translational stage so that the paper was positioned perpendicular to the movement caused by the translation stage. Because detecting Lamb waves in the MD was the objective, the paper was placed in the plastic frame so the MD of the paper was parallel to the optical lab bench. Once the paper was pulled tight and clamped within the plastic frame, the MEMS device was positioned a few millimeters from the paper sample so the front side of the cMUTs were facing and were parallel with the paper sample.

To obtain detection information from the cMUT a light source must target the membrane from the backside and reflect off the detection membrane back out the backside of the cMUT, as illustrated previously in Figure 2.3.2. A coherent light source was focused onto the backside of one of the cMUTs of the MEMS chip. The coherent light source used was a Melles Griot 30 mW He/Ne laser with a wavelength of 632 nm, specifically the 05-LHP-991 model number, pictured in Figure 3.2.1. In later versions of the MEMS device developed in Dr. Degertekin's laboratory, the illuminating laser is integrated directly onto the wafer. After reflecting off a mirror the He/Ne laser beam passed through first, an iris diaphragm, and then a convex lens, with a focal length and diameter of 1 cm. Both of these devices are pictured in Figure 3.2.2. The diaphragm and lens were used to focus the maximum amount of light directly onto one individual cMUT. The majority of our experimentation concentrated on testing the middle cMUT of the MEMS chip in Figure 2.3.6. The He/Ne laser beam had a diameter of 1.3 mm when it left the laser head. The cMUT's diameter was .16 mm. To gain the most

information from the cMUT the maximum amount of light must be directed onto the backside of the cMUT. The final spot size for the incident beam was achieved by use of an iris diaphragm and a convex, 10 mm in diameter. This implied that some of the incident beam passed around the cMUT and went through the glass substrate holding the array of cMUTs. Efforts were taken, which will be expanded upon shortly in this chapter, not to collect the light that traveled this path around the cMUT when collecting light of the 1st order diffraction beam. Light that did not enter the cMUT did not hold any useful information to collect regarding the cMUT's detection capabilities.

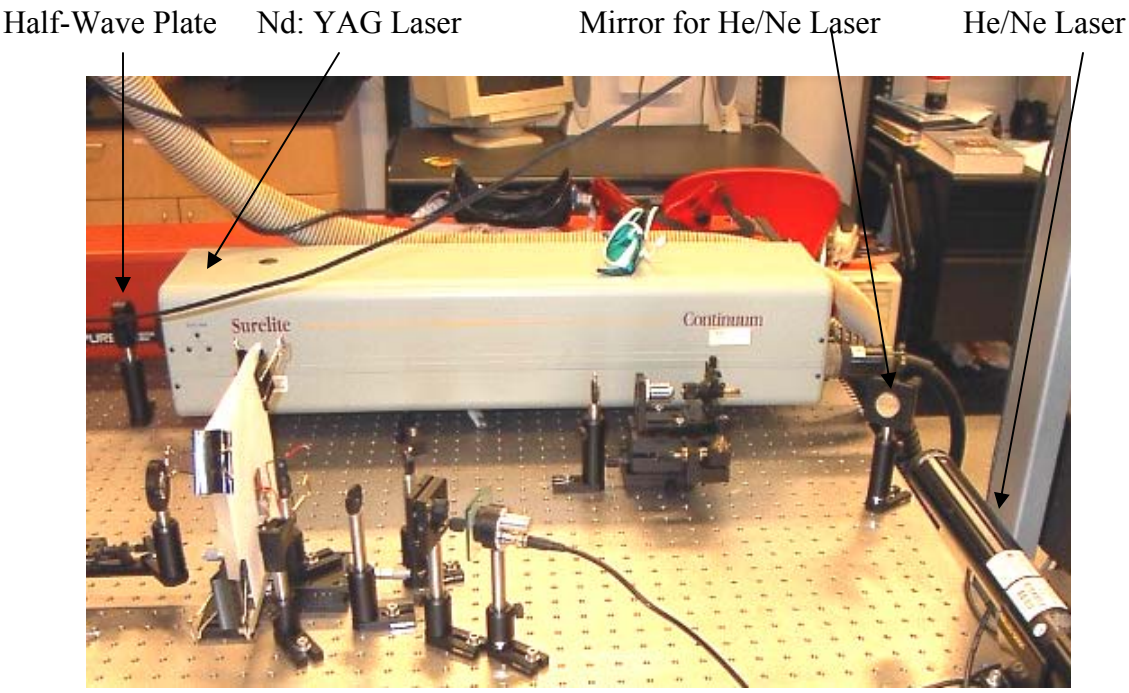

Figure 3.2.1. Experimental setup on lab bench for Lamb wave detection in paper using a cMUT and a He/Ne laser for an incident beam.

Once the incident beam was concentrated onto a specific cMUT the reflected diffraction orders became visible. As mentioned previously the first diffraction order

contained the most light intensity and made light detection by a photodetector the easiest compared to the other diffraction orders. In the path of the first diffraction order an iris diaphragm was placed to discard any scattered light that may have reflected off the MEMS chip but did not originate from the cMUT being investigated, such as light from the incident beam that passed around the cMUT. After the diaphragm, the 1st diffraction order beam was passed through a convex lens, 3 cm in diameter, with a 6 cm focal length. This lens focused the 1st order beam onto a photodetector, specifically a battery operated ThorLabs DET210 photodetector. The picture in Figure 3.2.2 shows the convex lens and photodetector used to capture the 1st order beam. Figure 3.2.2 also shows a square glass filter on the face of the photodetector which was used to block any unwanted light not of the He/Ne wavelength. Light of any wavelength above 900 nm would not be able to make its way through this filter. More specifically, the filter stopped scattered Nd: YAG laser light from entering the photodetector.

Efforts were taken to ensure that all the light reflected by the first diffraction order was concentrated onto the photodetector. The output signal from the photodetector was fed through a Low Noise Preamplifier (Standford Research Systems SR560 Model) and displayed on an oscilloscope (Tektronix TDS 420A) where the signal was analyzed and recorded.

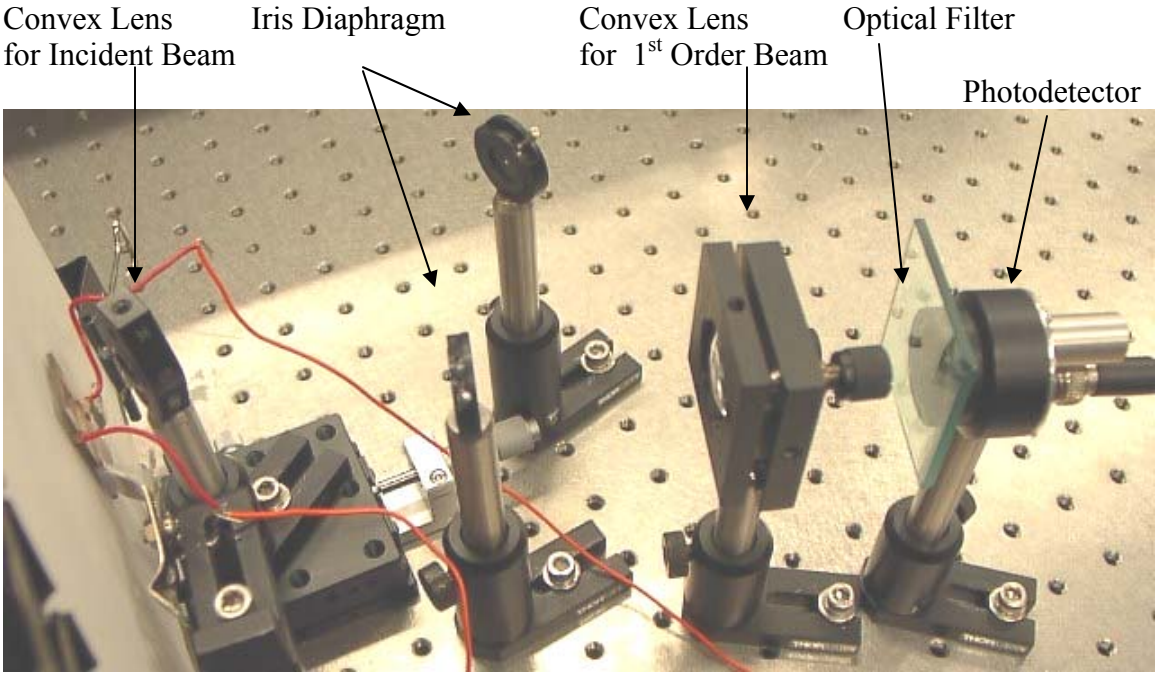

Figure 3.2.2. Experimental setup for Lamb wave detection in paper using a cMUT. Despite the appearance, the cMUT is not in contact with the paper. The MEMS to paper stand-off distance is less than .3 mm.

Combining the Lamb Wave Generation System and the cMUT Detection System

Combining the ultrasonic generation portion of the experiment and the cMUT detection system was the next step in our experimental procedure. A piece of Kodak heat sensitive paper was clamped into the plastic frame rather than a sample of raw stock paper. The translation stage holding this paper was adjusted so that the distance between the paper and the front of the MEMS chip was less than .5 mm. The Nd: YAG laser was fired and struck the light sensitive paper. The Nd: YAG laser pulse left a definitive mark on the sensitive paper. Because the light sensitive paper is not completely opaque some

of the incident He/Ne laser beam that passed around the cMUT is visible on the side of the paper in which the Nd: YAG generation laser beam has struck. This linear distance from the mark created by the Nd: YAG laser on the Kodak paper to the point at which some of the He/Ne laser light is noticeable is the source-to-receiver distance, which was measured using a digital caliper. Positioning adjustments were made to the focusing lens the Nd: YAG laser beam traveled through to ensure that the spot size was small enough to produce high energy Lamb waves and that the vertical position of the Nd: YAG beam was the same as the cMUT's vertical position to ensure wave travel in the MD only. Next, the heat sensitive paper in the plastic frame was replaced by a square piece of Raw Stock paper. The translation stage that moves the plastic frame was adjusted so there was a minimum stand-off distance between the paper and the MEMS device, less than .3 mm, as seen in Figure 3.2.3 and 3.2.4. Once both the Lamb wave generation and detection portion of the experimental setup were completed testing could proceed. Both the Lamb wave generation system and cMUT detection systems are photographically presented in Figure 3.2.5 together as they were employed during experimentation.

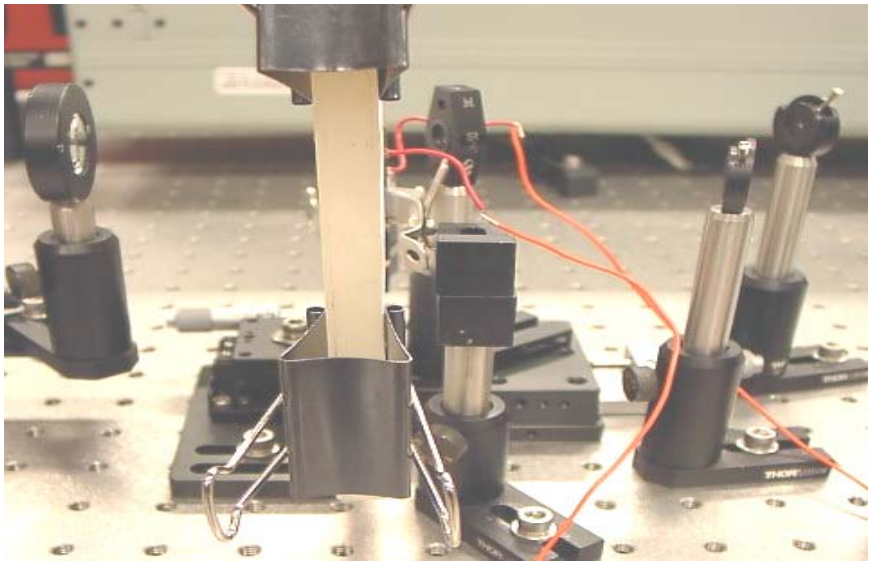

Figure 3.2.3. Experimental setup for Lamb wave detection using a cMUT. The MEMS chip holding the cMUT is not visible because the MEMS-to-paper stand-off distance is less than .3 mm. Only the wires that provide the MEMS chip with electrostatic actuation indicate that the MEMS device is present.

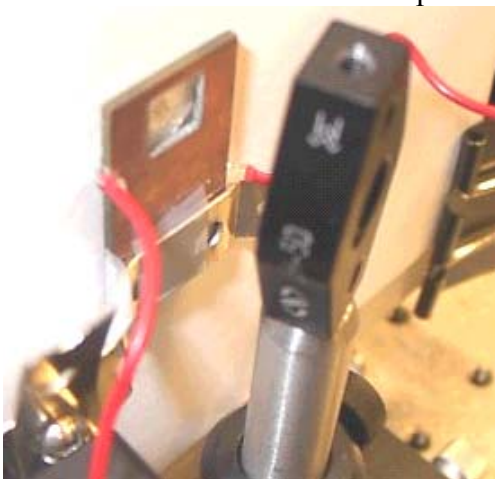

Figure 3.2.4. MEMS chip at a stand-off distance of less than .3 mm to the paper sample. The incident laser beam focusing lens is present and so are the wires that provide the MEMS chip with electrostatic actuation.

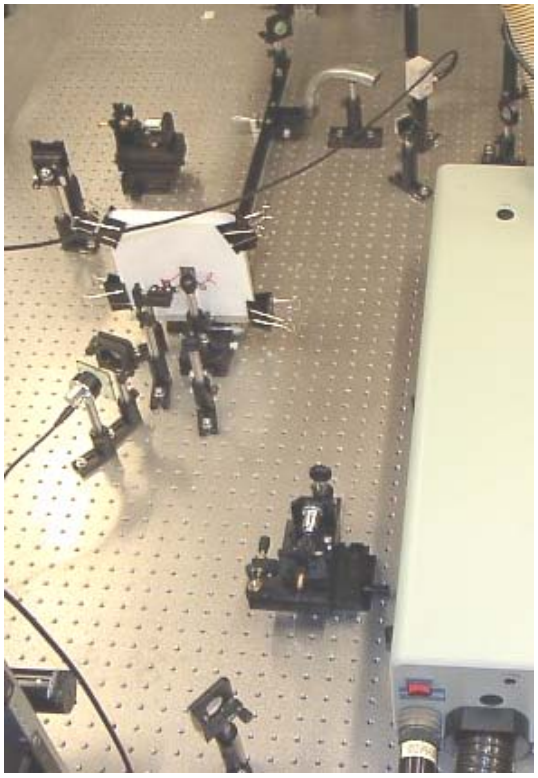

Figure 3.2.5. Photograph of both the ultrasonic Lamb wave generation system and cMUT detection system together as they were employed during experimentation on the lab bench.

3.3. Testing Procedure for cMUT Detection of Lamb Waves

After the Nd: YAG laser beam was positioned, the incident laser beam was directed onto the backside of the cMUT, and subsequently the first order of diffraction was being collected by the photodetector: testing could begin. First, the DC bias voltage was set to the optimum value of 20 Volts and the translation stage that positions the Nd: YAG laser beam was set so that the largest source-to-receiver distance would be tested first.

If the wave signal detected was satisfactory, it was recorded and the translation stage for the Nd: YAG laser beam was advanced a few millimeters laterally for a smaller

source-to-receiver distance. The reason for decreasing the source-to-receiver distance as opposed to increasing was that each time the Nd: YAG laser was fired the paper was slightly damaged. By moving this point of contact of the Nd: YAG laser beam with the paper closer to the detection point Lamb waves generated in subsequent trials would not travel through the damaged portion of the paper, thereby avoiding variations in the Lamb waves that were generated.

At this new position the Nd: YAG laser was fired and the wave signal was recorded. Four waveforms were recorded at each source-to-receiver distance. Measurements were taken at five source-to-receiver distances: 29, 26, 23, 20, and 15 mm. See Figure 3.3.1.

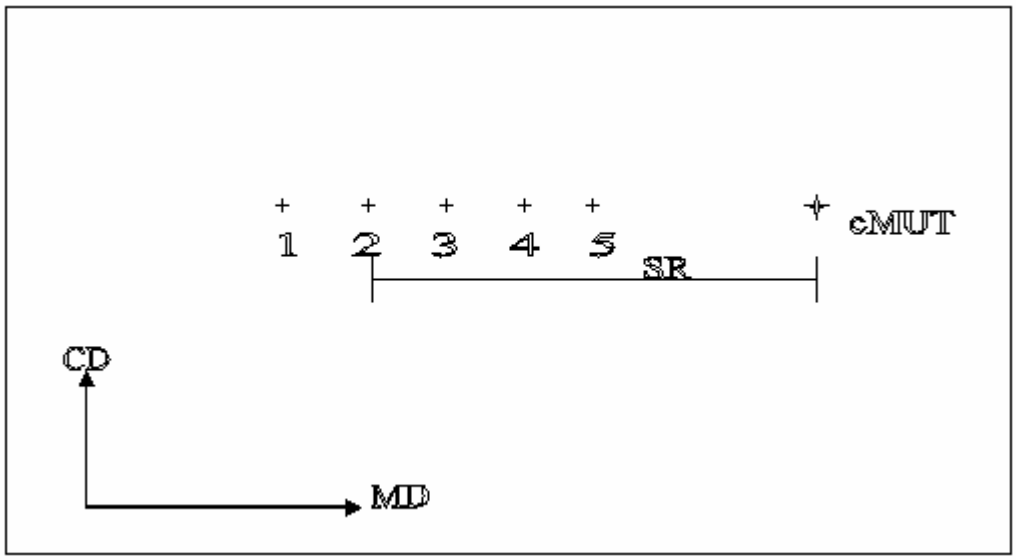

Figure 3.3.1. Illustration of a how testing would proceed from point one to five for a sample of paper. The source-to-receiver distance (SR) marked in this Figure is the linear distance between the point at which the Nd: YAG laser was fired at point two and the cMUT, depicted as a four point star.

Generally, the source-to-receiver distance was decreased from 29 mm to 15 mm in increments of 3 mm. After the last source-to-receiver point was tested the paper sample was unclamped from the plastic frame, discarded, and replaced with a brand new paper sample.

3.4. Lamb Wave Detection with Laser Interferometry

To gauge the performance of the cMUT's ability to detect Lamb waves in paper, a laser interferometer, a more customary method for detecting ultrasonic waves in paper, was tested. The laser interferometer was a modified Mach-Zehnder Interferometer that used a continuous Argon Ion laser beam.

The system is described in detail in M. Cornwell's MS thesis [16]. Figure 3.4.1 shows an overview of this system. The Argon:Ion laser, that was used was set to 3.5 W at 514 nm. After the laser beam left the laser head the laser traveled through a Bragg Cell which separated the beam into two beams. One of the beams, called the target beam, remained unchanged and this beam was eventually focused onto the paper sample being tested. The second beam was frequency shifted by 40 MHz; it is called the reference beam. The reference beam did not come in contact with the test sample, but eventually it recombined with the target beam after the target beam had reflected off the test sample.

To detect Lamb waves in paper the target beam diameter on the paper sample must be smaller than half of the wavelength of the Lamb waves that are of interest in being detected. [12][37] In this experimental setup, the interferometer target beam size was .3 mm in diameter. The Lamb waves that are of interest in being detected have a

wavelength of the range of .5 mm to 3 mm, which correspond to a 20 kHz to 250 kHz frequency range. As a result, this modified Mach-Zehnder Interferometer had Lamb wave detection capability in this frequency range.

Initially, after the laser beam exited the laser head and traveled through the Bragg cell, both beams were reflected off two mirrors and separated so that both beams could be guided into their individual fiber launchers. See Figure 3.4.2 for a photograph of the laser paths just described. After being fed into their respective fiber launchers each laser beam was focused into an optical single mode fiber cable with a glass core of 3.3 μm. The fiber was protected by cladding with a diameter of 80 μm, and an outer jacket of 200 μm in diameter.

The target beam optical fiber was positioned so the laser light exiting this fiber was directed onto the paper sample. Between the exit of this target beam fiber and paper was placed a 5 mm, ¼ pitch, gradient index (GRIN) lens and then a 20X objective lens. The GRIN lens used has an index of refraction that varies radially forcing a beam that exits the lens to be very concentrated. After leaving the GRIN lens the target beam passed through a 20X objective lens, which was positioned to focus the target beam onto the paper sample at the same vertical position as the generation spot of the Nd: YAG laser.

Once the target beam hit the paper sample the light was scattered in all directions. Some of this scattered light reenters the 20X objective lens. A portion of this scattered light that reenters the objective lens was focused onto another ¼ pitch GRIN lens, which concentrated its light into a new fiber optic cable. This new fiber cable is a multimode fiber with a diameter of 50 μm to allow enough light to be collected. After traveling

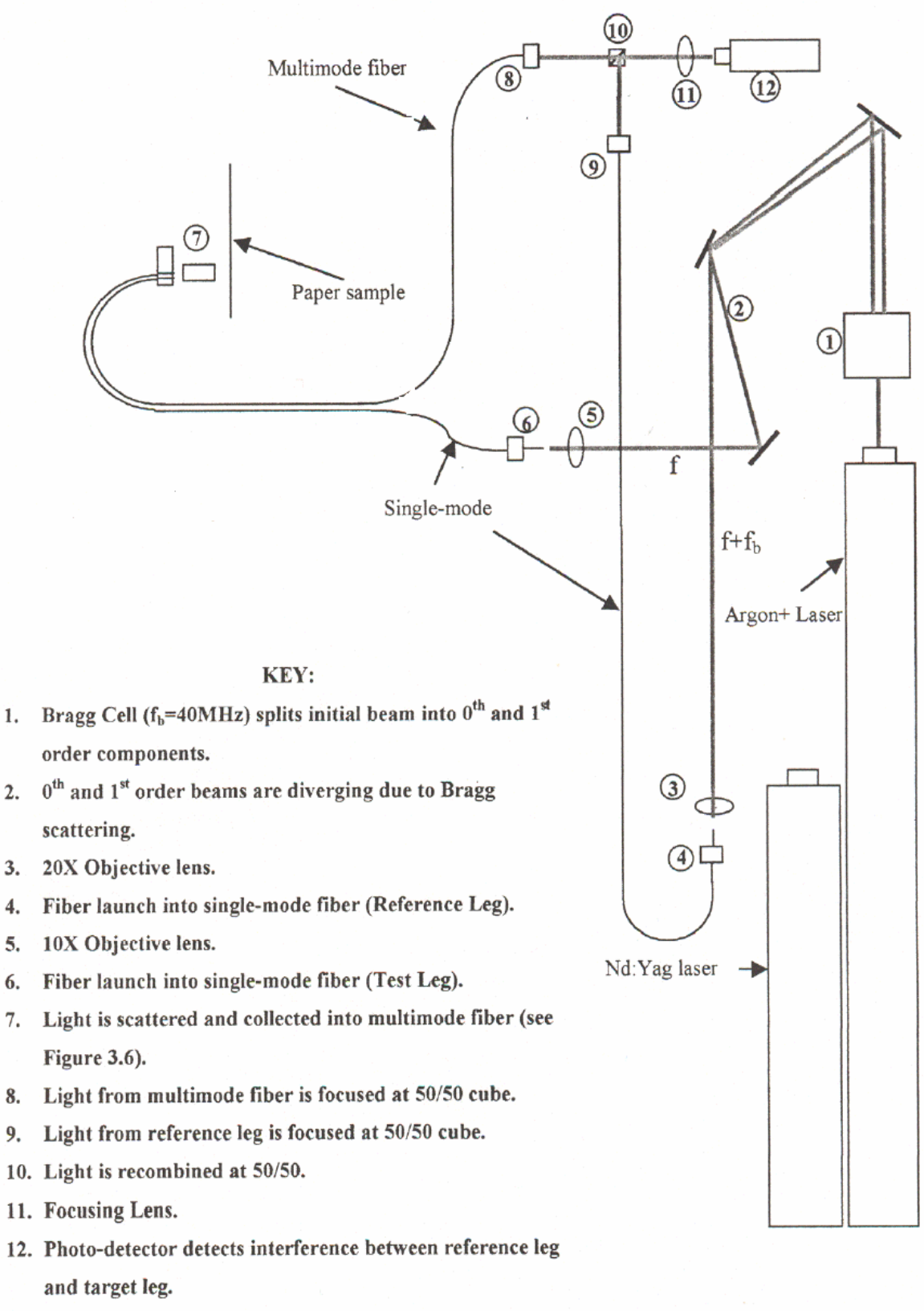

Figure 3.4.1. Diagram of modified Mach-Zehnder Interferometer. [16]

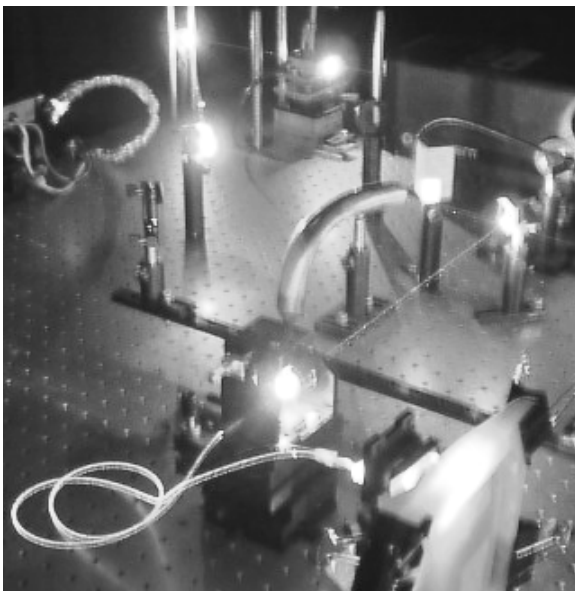

Figure 3.4.2. Picture of Interferometer during experimentation. In the foreground the target beam is seen being collected into a fiber by a fiber launcher and finally directed onto the paper sample.

through the multimode fiber the light exits onto another GRIN lens which focused its light onto a 50/50 cube where it was collimated and recombined with the reference beam laser light to produce interference at the Bragg frequency of 40 MHz.

The reference beam after leaving the Bragg cell was also transmitted through a fiber launcher. This fiber traveled to the point on the lab bench where recombination took place with the target beam. To ensure laser light coherence when using an Argon Ion laser the difference in distance between two beam paths must be less than one meter. The difference in distance between the reference beam and target beam during experimentation was about .3 m. The reference beam exited the fiber through a GRIN lens which focused the light onto the 50/50 cube where it was collimated and recombined with the target beam. The reference beam, while on its way to the 50/50 cube passed

through a waveplate after exiting its GRIN lens. This waveplate, similar to the waveplate used with the Nd: YAG laser beam, when used together with a polarizer limits the amount of light transmitted of the reference beam. In this manner, the light intensity of both the reference beam and target beam when recombined could be matched. This keeps the reference leg light from drowning out the light collected by the target beam, which is weaker in intensity since it is only a portion of scattered light off the paper sample. [39]

Now both the target beam and reference beam intersect each other on the 50/50 cube. As shown in Figure 3.4.3 this cube is designed to reflect at a 90° angle roughly 45% of a beam entering the cube and transmit 45% of the beam directly through the cube. By intersecting upon the 50/50 cube, the reference beam and target beam are collimated and combined once again. After the two beams were recombined this single beam

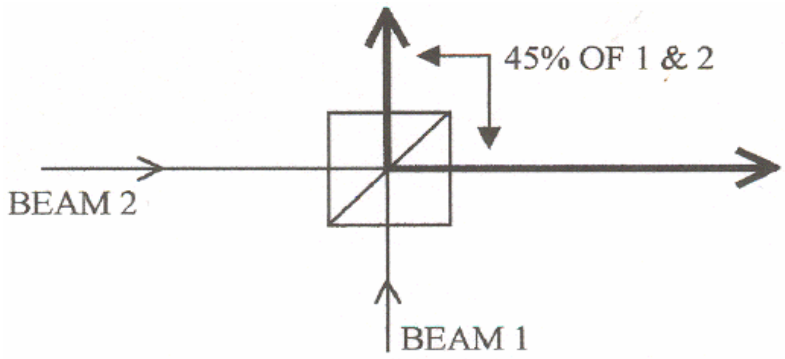

Figure 3.4.3. Path of two beams passing through a 50/50 cube.

was directed through a convex lens with a 5 cm focal length. The polarizer, which was mentioned previously in this chapter, works in combination with the waveplate to keep the reference leg from dominating the signal. The polarizer is secured to the backside of

this convex lens. See Figure 3.4.4. Finally, the light exited this convex lens and the polarizer and was focused onto a photodetector, which yielded a voltage that was proportional to the light intensity it detected.

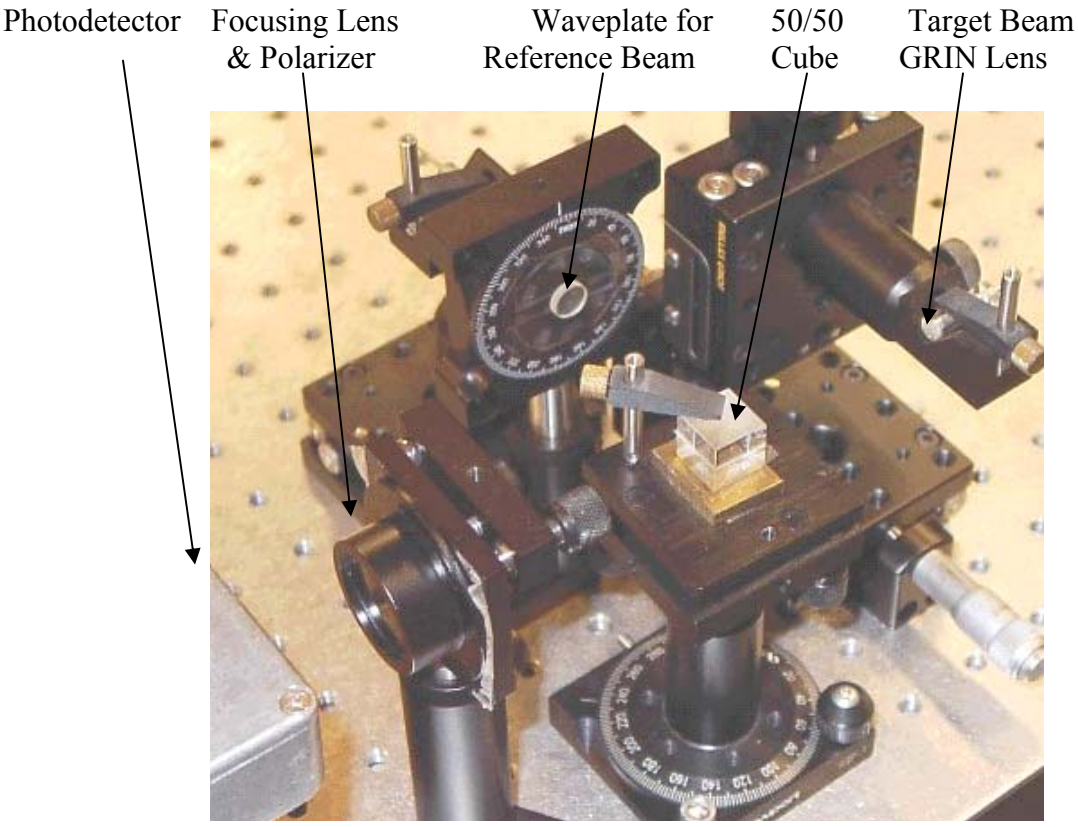

Figure 3.4.4. Experimental setup used by the interferometer to detect the recombined reference and target beams.

The output signal from the photodetector was first passed through a filter, specifically a DK-40-10P-B bandpass filter manufactured by TTE Inc. This filter only allowed a signal that was within a 36 MHz to 44 MHz filtering range to be transmitted. Next the signal was passed through an attenuator, specifically a Kay Elemetrics Corp. 837 attenuator. The attenuator was incorporated into the setup because the FM

discriminator, the next device the electronic signal travels to, could overload if a signal reached the discriminator with a peak to peak voltage above 225 mV. The FM discriminator demodulates the FM signal with a carrier frequency of 40 MHz. The output of the FM demodulator is therefore the Lamb wave signal. From the discriminator the signal traveled through a low noise preamplifier (SR 560). In addition to providing some gain to the signal, the preamplifier was set to filter out frequencies below 3 kHz and above 1 MHz, the same filtering range used during cMUT testing. Once the signal was filtered it was passed to the oscilloscope for recording and analysis. Some practical details concerning the optical alignment of the interferometer are given in Appendix F.

The testing procedure for the interferometer was very similar to the testing procedure for the cMUT. A 17 cm^2 piece of raw stock paper was clamped into the plastic frame. The plastic frame and paper were positioned perpendicular to the target beam light exiting the objective lens, as seen in Figure 3.4.5. Similar to cMUT testing, the frame was placed on a 13 mm translation stage that could move the frame and paper further or closer to the objective lens. The distance at which the frame was placed with respect to the objective lens was determined by slowly moving the translation stage towards or away from the objective lens until a position was reached at which the maximum amount of scattered light off the paper was reflected back into the objective lens. The maximum amount of scattered light was quantified by monitoring the amount of light exiting onto the 50/50 cube from the target beam leg. Fine adjustments were made to the entire interferometer setup to ensure that the intensity of the returning target beam upon the 50/50 cube was as high as possible. This intensity was not only monitored visually, but by also maintaining a steady 40 MHz signal upon an oscilloscope

that was fed continuously the electric signal created by the photodetector. A steady 40 MHz signal was indicative of excellent collimation and recombination of the two beams.

The source-to-receiver distance was measured during interferometer testing by firing the Nd: YAG laser once at a piece of light sensitive paper and recording the distance between the Nd: YAG laser mark on the paper to the mark created by the target beam on the heat sensitive paper. Then a piece of raw stock paper was placed in the plastic frame. The paper was adjusted to optimize the 40 MHz Bragg signal and then the Nd: YAG laser was fired. The resulting waveform was captured on the oscilloscope, the source-to-receiver distance was decreased by a set amount, similar to cMUT testing, and the process was repeated until all the source-to-receiver distances for that particular sample of paper were tested.

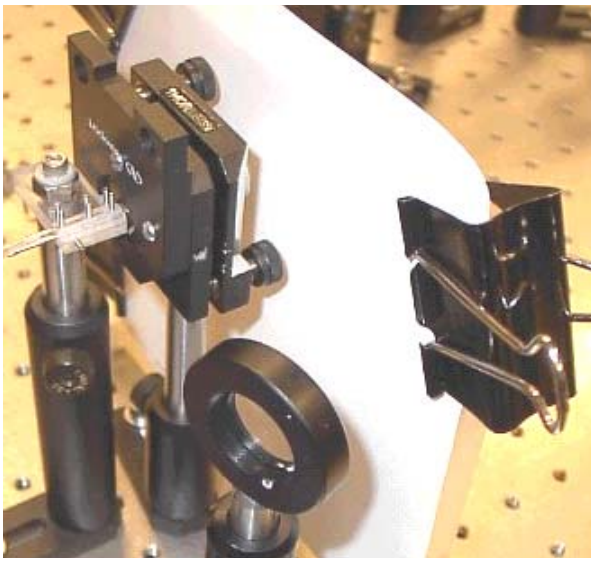

Figure 3.4.5. Picture of Nd: YAG laser focusing lens, plexiglass mount holding GRIN lenses, objective lens holder, and a sample of paper positioned as during interferometric testing.

CHAPTER 4

EXPERIMENTAL RESULTS

4.1 Sensitivity of the MEMS Microphone to Ultrasonic Lamb Waves

4.1.1. Sensitivity to Acoustic Pressure

The sensitivity, S, of the cMUT, in Volts/Pa, is defined as the output voltage of the cMUT for an incident acoustic pressure on the membrane. It was determined experimentally using the experimental arrangement shown in Figure 4.1.1.

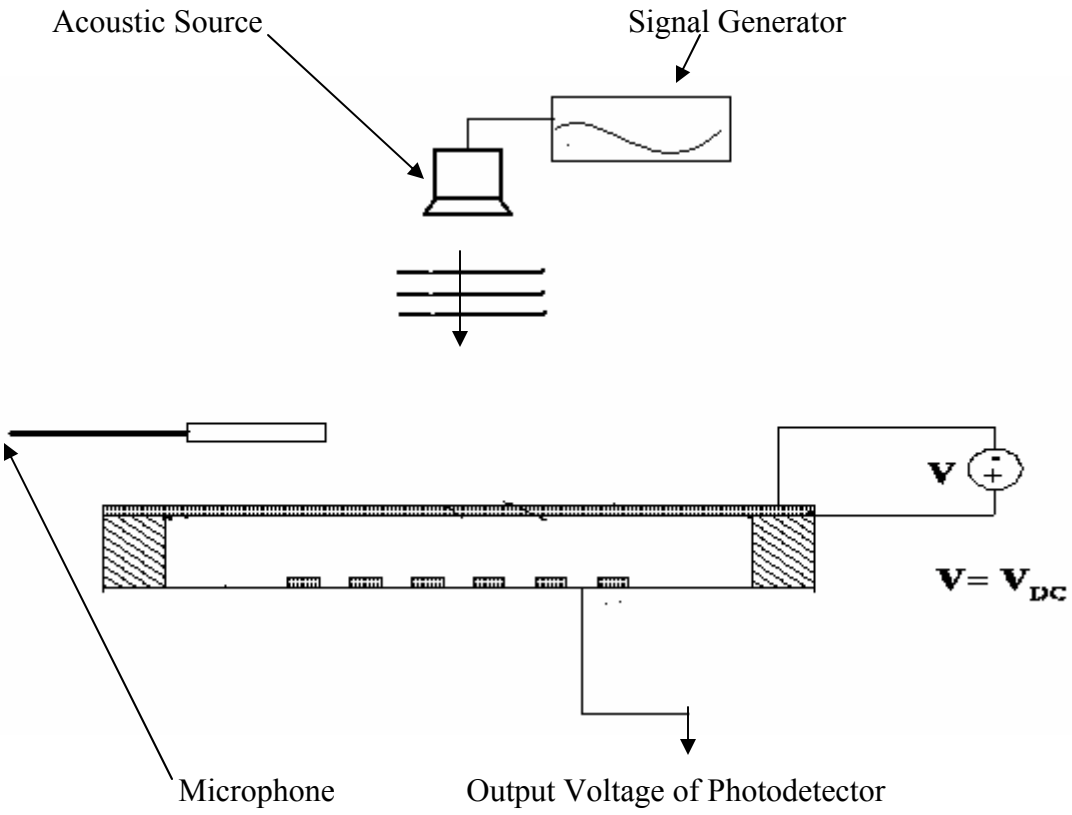

Figure 4.1.1. Schematic of experimental arrangement for cMUT sensitivity testing.

1. The backside of the cMUT was illuminated with a He/Ne laser light and the first diffraction order was collected by a photodetector.

2. A loudspeaker five inches in diameter was placed five inches from the front face of the MEMS chip and it put out continuously a 20 kHz acoustic signal.

3. The DC bias was set to 21.9 Volts.

4. As a result of the 20 kHz acoustic signal the first diffraction order displayed on the oscilloscope a 2.86 Volts peak to peak electric signal. This signal was a result of amplifying the signal from the photodetector 20 times and filtering low and high frequency noise below 3 kHz and above 1 MHz. The actual voltage output produced by the cMUT corresponds to .143 mV.

5. A free field microphone (G.R.A.S Prepolarized Type 40BE) was held very close to the MEMS chip to detect the acoustic signal produced by the speaker.

6. The free field microphone transmitted a 130 mV peak to peak electric signal for the previous conditions.

7. The microphone was calibrated at 4.48 mV/Pa, G.R.A.S (2001), so that the peak to peak pressure amplitude was 130 mV / 4.48 mV/Pa = 29 Pa.

8. The total sensitivity S by definition was calculated to be $\frac{.143mV}{29Pa} = \frac{.0049mV}{Pa}$

The sensitivity is therefore measured to be about 5 μV / Pa at 20 kHz before any amplification. 20 kHz was the frequency chosen as the acoustic signal because it was a typical frequency detected by the cMUT during Lamb wave testing in paper. See section 4.2.

4.1.2. Electrical Sensitivity

The electrical sensitivity is defined as the output voltage, V, of the cMUT for a given AC displacement of the membrane. As illustrated in Figure 4.1.2, V is the voltage output proportional to the light intensity of the first diffraction order upon the photodetector. The light intensity of the first diffraction order on the photodetector could vary from one experimental setup to the next for many reasons. The amount of incident laser light collected onto the cMUT and the angles at which this incident light reflected off the detection membrane are the main reasons. Therefore, the cMUT's electrical sensitivity varied day to day during experimentation.

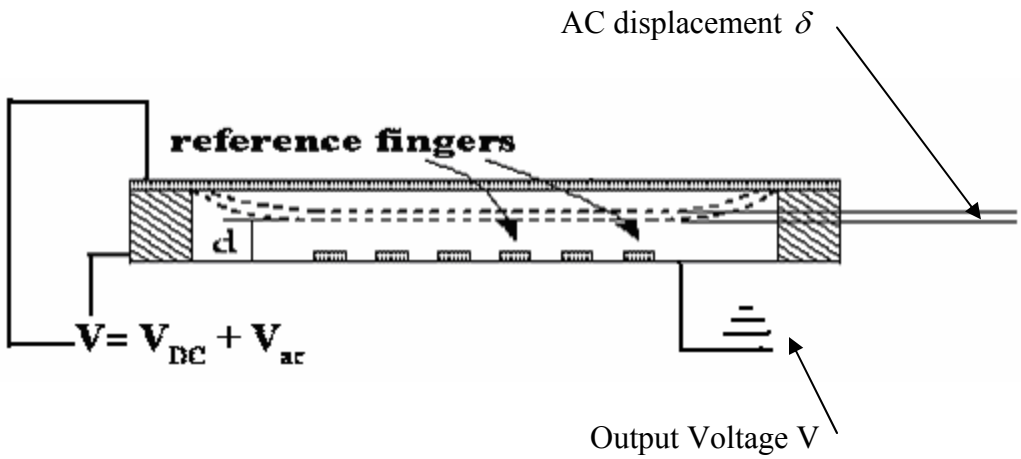

Figure 4.1.2. Side view illustration of a cMUT unit depicting the AC displacement, δ, of the membrane caused by V_{AC} input to simulate acoustic excitation. The optimum gap height, d, is controlled by DC bias voltage.

The electrical sensitivity is Se = V / δ, in Volts/Å. The displacement of the membrane was measured with a laser Doppler Vibrometer (Polytec OFV 055-PSV 200).

A Hewlett Packard HP 33120A signal generator was used to generate a 1 Volt peak to peak AC signal at 100 kHz. As explained in section 2.3, the output voltage depends also on the DC bias voltage supplied to the cMUT. The DC power supply (Dagatron 7202) was used to apply a DC voltage that could be adjusted between 0 and 50 Volts. The laser vibrometer measures the AC peak velocity (in mm/s) of the membrane. A typical result is shown in Figure 4.1.3 for a DC bias of 20 Volts. Results for other DC bias values are tabulated in Appendix C. The velocity can be converted to amplitude displacement by $\delta = (velocity / \omega)$, where $\omega = 2\pi f = 2\pi \times 10^5 \, rd / s$.

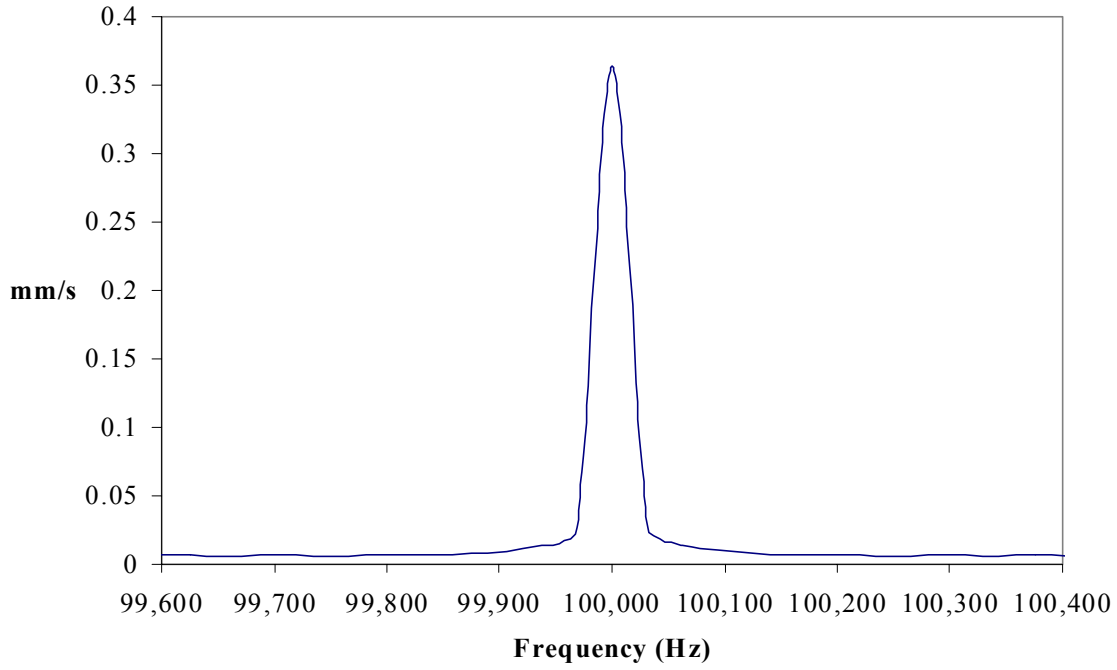

Figure 4.1.3. Velocity of a 160 μm cMUT detection membrane as recorded and displayed by the LDV at a DC bias voltage of 20 Volts and an AC electric potential of 1 Volt at 100 kHz.

The AC displacement can be measured for various DC bias voltages and the calibration curve is shown in Figure 4.1.4, for the case of an AC signal of 1 Volt amplitude and 100 kHz frequency. A linear regression indicates that the membrane deflection (in Angstroms) is related to the DC voltage by:

$$y = .417x - 3.1491 \tag{4.1}$$

where,

x=DC bias Voltage

y=membrane deflection in Angstroms.

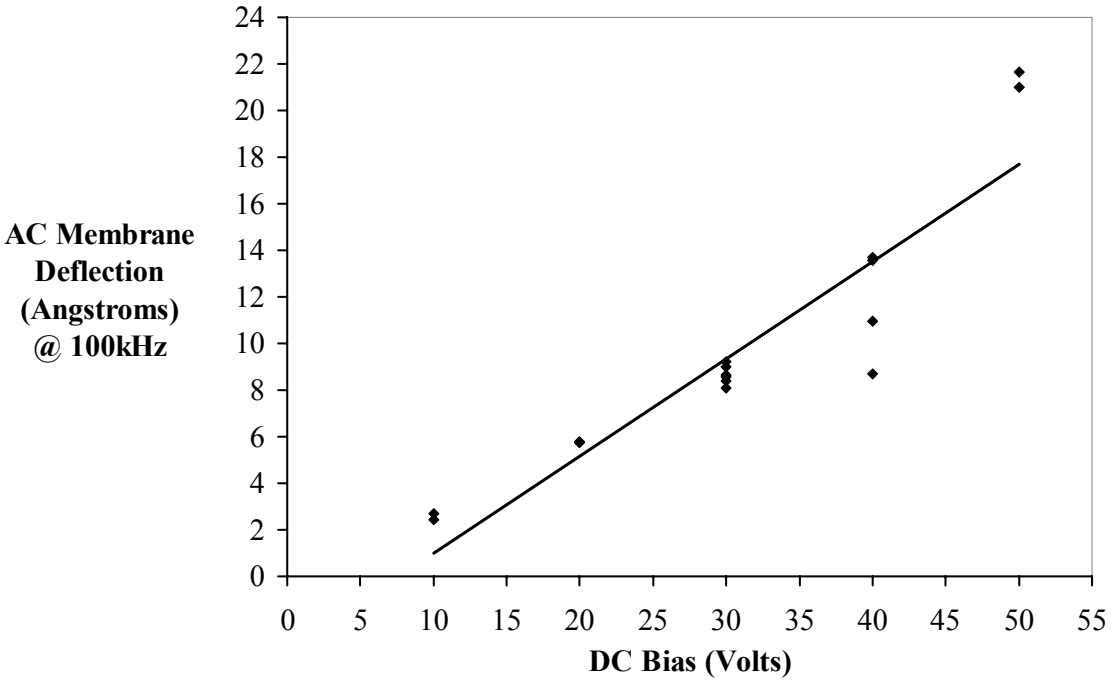

Figure 4.1.4. 160 μm cMUT detection membrane's deflection at various DC bias voltages and an additional electric potential of 1 Volt at 100 kHz.

Equation 4.1 applies only for the case of an AC input signal of 1 Volt at 100 kHz. A typical value of 21.9 Volts DC bias, measured an output voltage of .18 mV. The corresponding amplitude displacement is 6 Å (from equation 4.1), and the corresponding electrical sensitivity is: Se= 30 μV/Å.

4.1.3. Mechanical Sensitivity.

The mechanical sensitivity, Sm, characterizes the cMUT membrane response to an incident pressure. It is defined as the ratio of the AC displacement of the membrane to the acoustic pressure amplitude. As indicated in Figure 4.1.5, it is related to the sensitivity S and the electrical sensitivity Se by:

$$S = Se \times Sm = \left(\frac{V}{\delta}\right)\left(\frac{\delta}{P}\right) \tag{4.2}$$

where: S_m is in units of Angstroms per Pascal

S_e is in units of Volts per Angstroms.

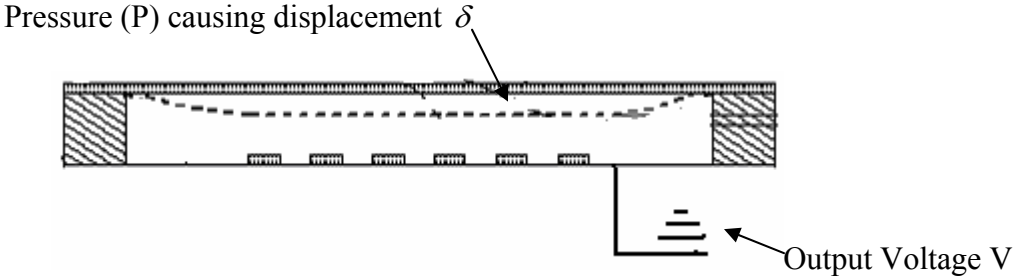

Figure 4.1.5. Side view illustration of cMUT experiencing an acoustic pressure, P. This pressure causes the detection membrane to deflect δ, subsequently altering the output voltage.

A frequency of 100 kHz was chosen as the driving frequency, the mechanical sensitivity is relatively independent of frequency between 10 kHz to 400 kHz, according to a mechanical sensitivity model, Figure 4.1.6, developed by N. Hall. [15] In addition, 100 kHz was chosen as the driving frequency, because according to the model in Figure 4.1.6 Sm values due to either electrostatic or acoustic actuation are similar in value, so a Sm value obtained by electrostatically actuating the cMUT can be a surrogate value for the Sm of the cMUT through acoustic actuation.

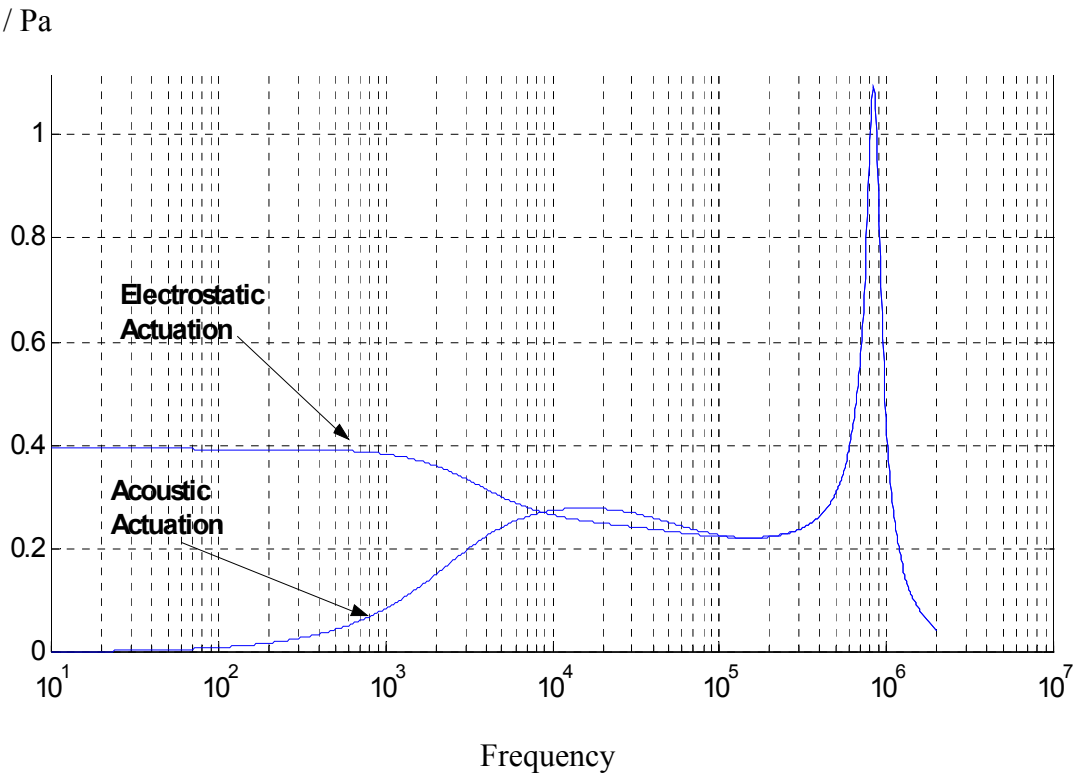

Figure 4.1.6. Model of cMUT's mechanical sensitivity due to both electrostatic and acoustic actuation at various frequencies. [15]

According to equation 4.2 and the values obtained thus far for Se and S, the mechanical sensitivity, $Sm = \frac{S}{Se} = \frac{.0049 mV / Pa}{.03 mV / Angstrom} = \frac{.163 Angstrom}{Pa}$.

This calculation assumes that Se is the same at 100 kHz and 20 kHz. The model developed by N. Hall estimates that the mechanical sensitivity, Sm, is .28 Å/Pa. The value of Sm determined experimentally from the calibration discussed above is .163 Å/Pa, a difference of 41%.

4.1.4. Sensitivity to Ultrasonic Waves

The sensitivity of the MEMS device to surface displacement in paper is another important characteristic of the cMUT that was tested. To calculate this value, two values were needed. First, the peak voltage of a Lamb wave detected in paper by the cMUT. As will be expanded upon further in this Chapter, a peak voltage of 300 mV was generally recorded by the oscilloscope after the cMUT signal of a wave in paper was amplified (x 20) and filtered. Second, the surface displacement amplitude of the paper, under the same excitation, was measured with a Laser Doppler Vibrometer (Polytec CLV). The Nd: YAG laser was fired at various source-to-receiver distances onto the paper sample, as during normal experimental trial runs, and the Vibrometer recorded the velocity of the out of plane motion of the paper. The recorded signal was simply integrated over 1 μs time steps to arrive at the surface displacement of the paper, as shown in Figure 4.1.7. The peak amplitude is shown to be about 200 nm. The estimated voltage to displacement sensitivity of the cMUT is therefore 7.5 μV / Å, without any signal amplification. Amplifying the signal (x 20) results in a 1.5 mV/Å sensitivity.

The Laser Doppler Vibrometer provides us with another Lamb wave detection signal of the out of plane displacement to compare cMUT detection signals with. Figure 4.1.8 is an FFT plot of the wave signal in Figure 4.1.7, which was detected by the Vibrometer. This plot shows a peak frequency at 8 kHz and at 25 kHz. Data will be presented later in this chapter (Section 4.6) that will show uniformity among the peak frequencies and their phase velocities for signals detected by the Vibrometer and the cMUT.

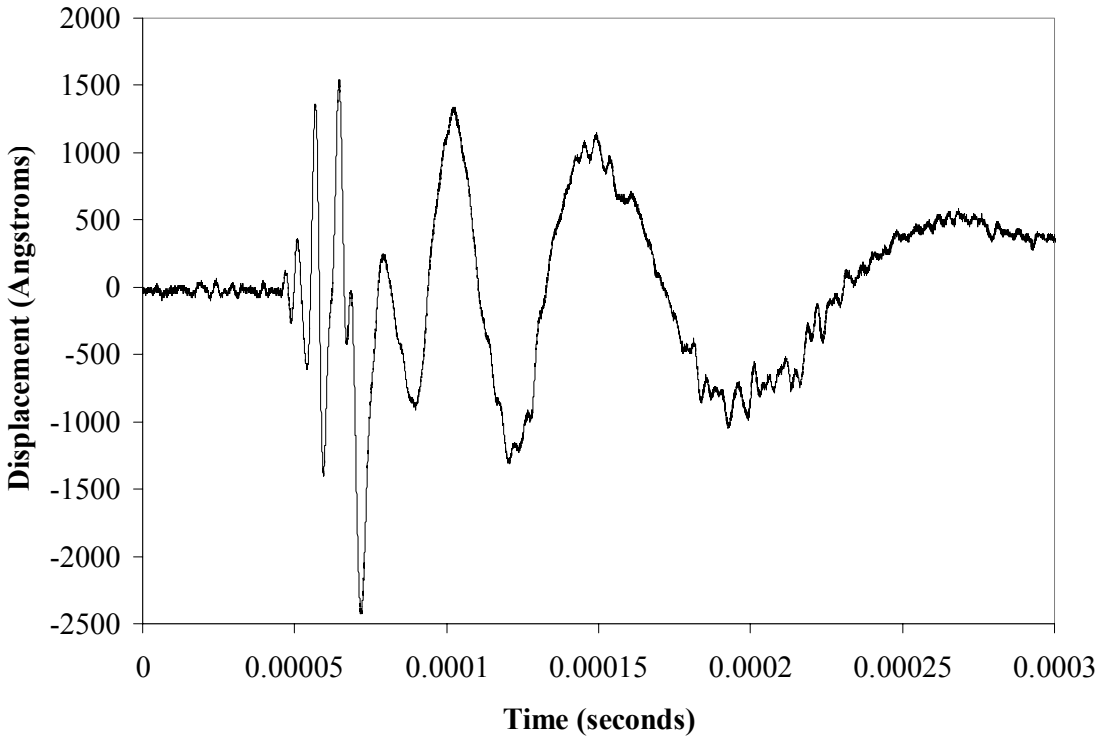

Figure 4.1.7. Paper displacement recorded by a Laser Doppler Vibrometer (LDV) at a source-to-receiver distance of 26 mm. Negative displacement simply indicates displacement away from the LDV.

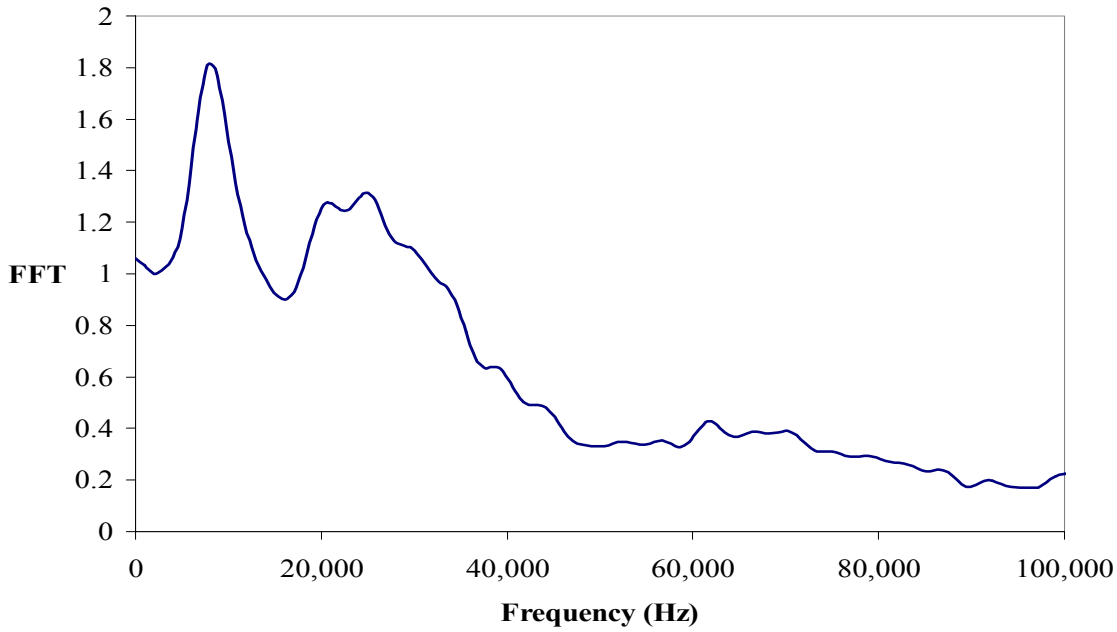

Figure 4.1.8. FFT of the Compact Laser Doppler Vibrometer signal, presented in Figure 4.1.7. The source-to-receiver distance is 26 mm.

4.2. Measurements at Various Source-To-Receiver Distances

Ultrasonic waveforms were detected with the cMUT sensor for several source-to-receiver distances. The Q-switched laser pulse was used to generate a Lamb wave in paper (Raw Stock 5914-3, 17 cm^2). The cMUT was placed as close as possible to the paper sample, without touching it. It is estimated that the stand-off distance between the paper and the cMUT membrane was about .3 mm. A DC bias voltage of 20 Volts was applied. The signal was amplified ($\times 20$) and filtered (3 kHz-1 MHz) and recorded on an oscilloscope. Figures 4.2.1(a) to (e) show the results (no averaging) for source-to-receiver distances of 29, 26, 23, 20, and 15 mm. The sensor clearly detects a Lamb wave. Figure 4.2.2(a) to (e) also presents resulting Lamb waves at similar source-receiver distances but at a stand-off distance of 1 mm.

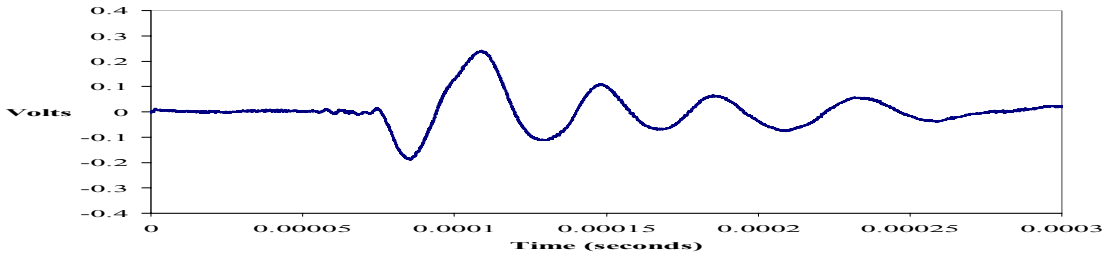

(a)

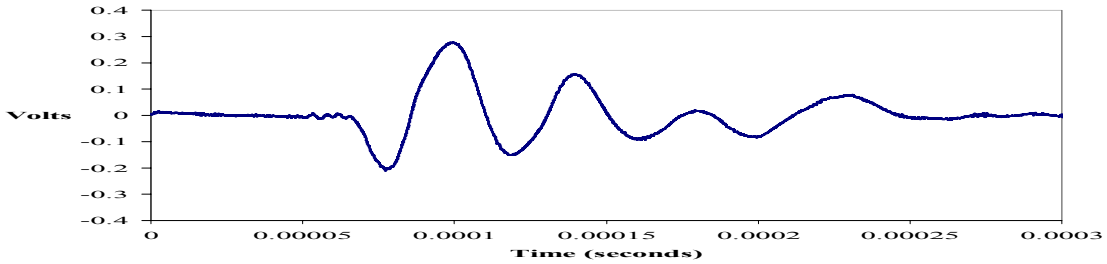

(b)

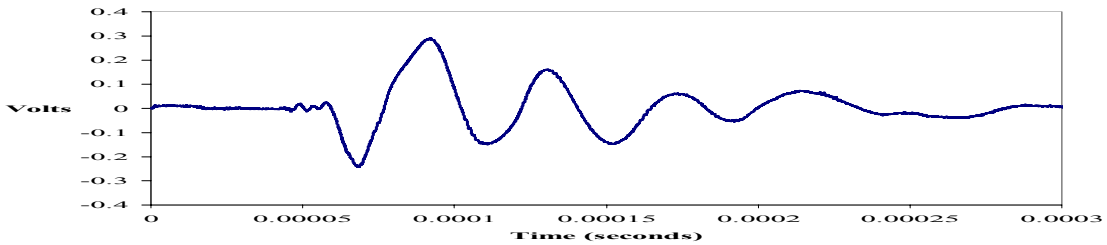

(c)

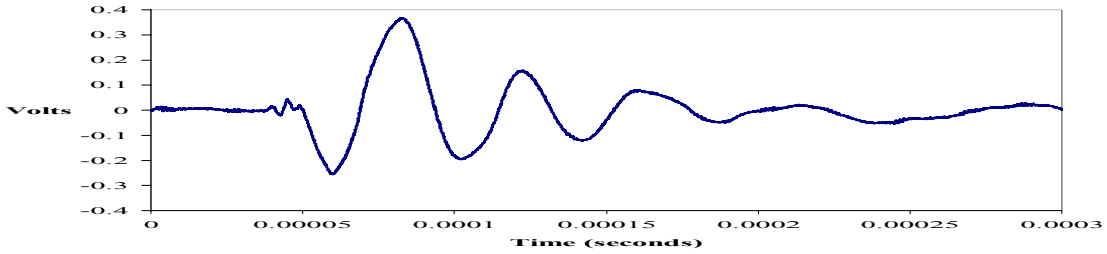

(d)

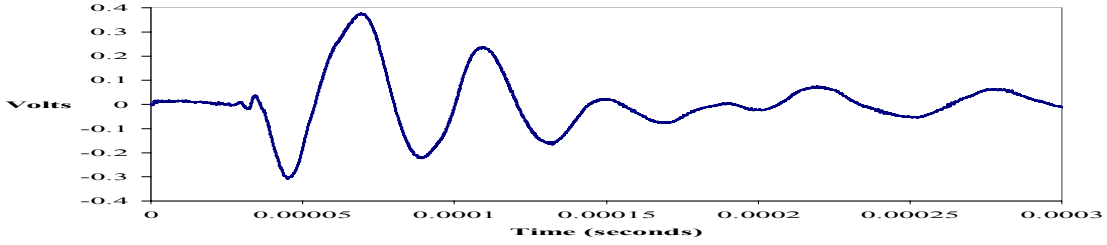

(e)

Figure 4.2.1. Lamb waves detected in paper by a 160 μ m cMUT at a source-to-receiver distance of (a) 29, (b) 26, (c) 23, (d) 20, and (e) 15 mm. The MEMS-to-paper stand-off distance was less than .3 mm.

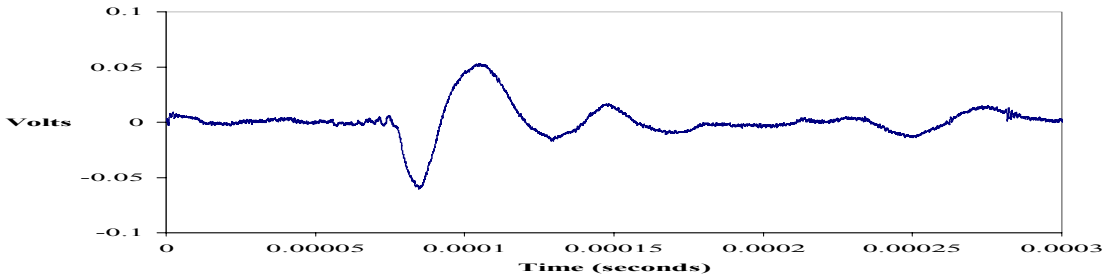

(a)

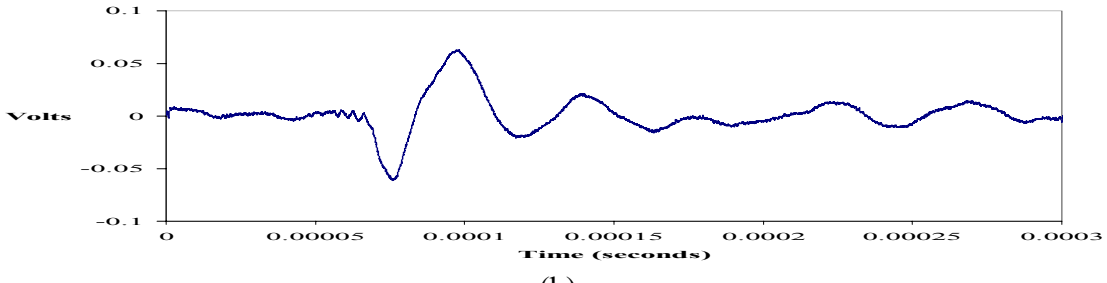

(b)

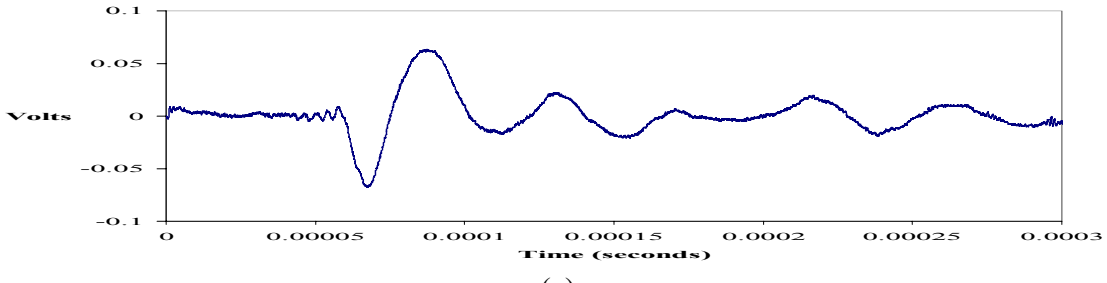

(c)

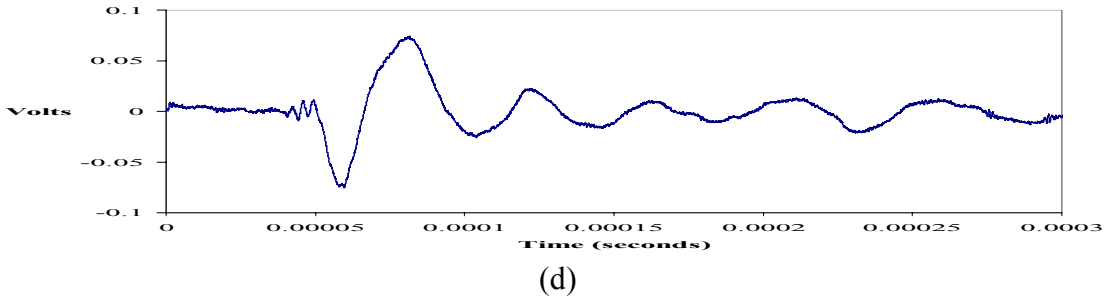

(d)

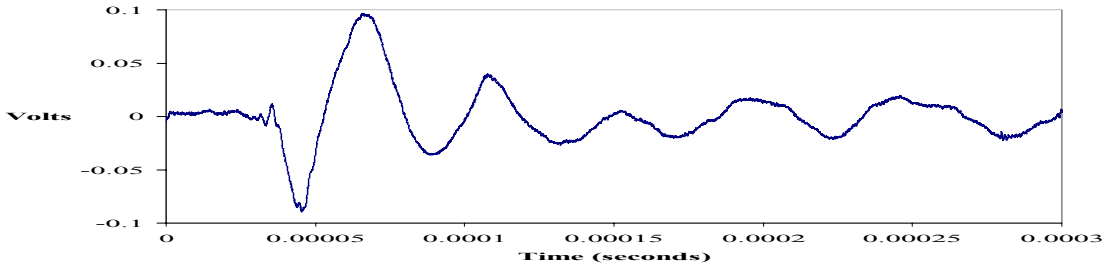

(e)

Figure 4.2.2. Lamb waves detected in paper by a 160 μ m cMUT at a source-to-receiver distance of (a) 29, (b) 26, (c) 23, (d) 20, and (e) 15 mm. The MEMS-to-paper stand-off distance is 1 mm.

The Lamb wave detected by the MEMS device shown in Figures 4.2.1 and 4.2.2 have little dispersion and a frequency content concentrated around 24 kHz. A direct measurement of the phase velocity at that frequency can be obtained from the time of arrival of the peaks of the waveform. Figure 4.2.3 shows the arrival times of the first peaks of the wave signals presented in Figure 4.2.1 as a function of source-receiver distance. The inverse of the slopes in Figure 4.2.3 is therefore a direct measurement of the phase velocity. It is found that the 24 kHz component of the Lamb wave detected with the MEMS device propagates at a phase velocity of about 349 m/s, +/- 5 m/s. Similar results were obtained when the same analysis was completed for the wave signals at stand-off distance of 1 mm, presented in Figure 4.2.2. Figure 4.2.4 presents the arrival times of the first peaks of the wave signal as a function of source-to-receiver distance and at a stand-off distance of 1 mm. At a stand-off distance of 1 mm the 24 kHz component of the Lamb wave propagated at a phase velocity of 350 m/s, +/- 6 m/s.

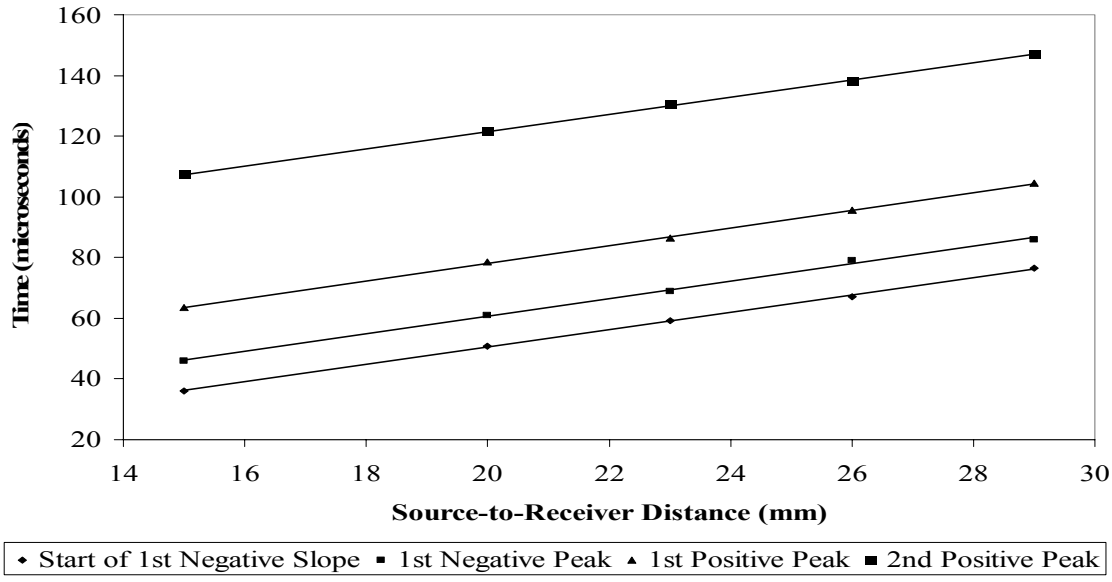

Figure 4.2.3. Arrival times for the first peaks of the Lamb waves detected by a 160 μm cMUT as a function of source-to-receiver distance at a MEMS-to-paper stand-off distance of less than .3 mm. Linear regression lines are presented for each peak.

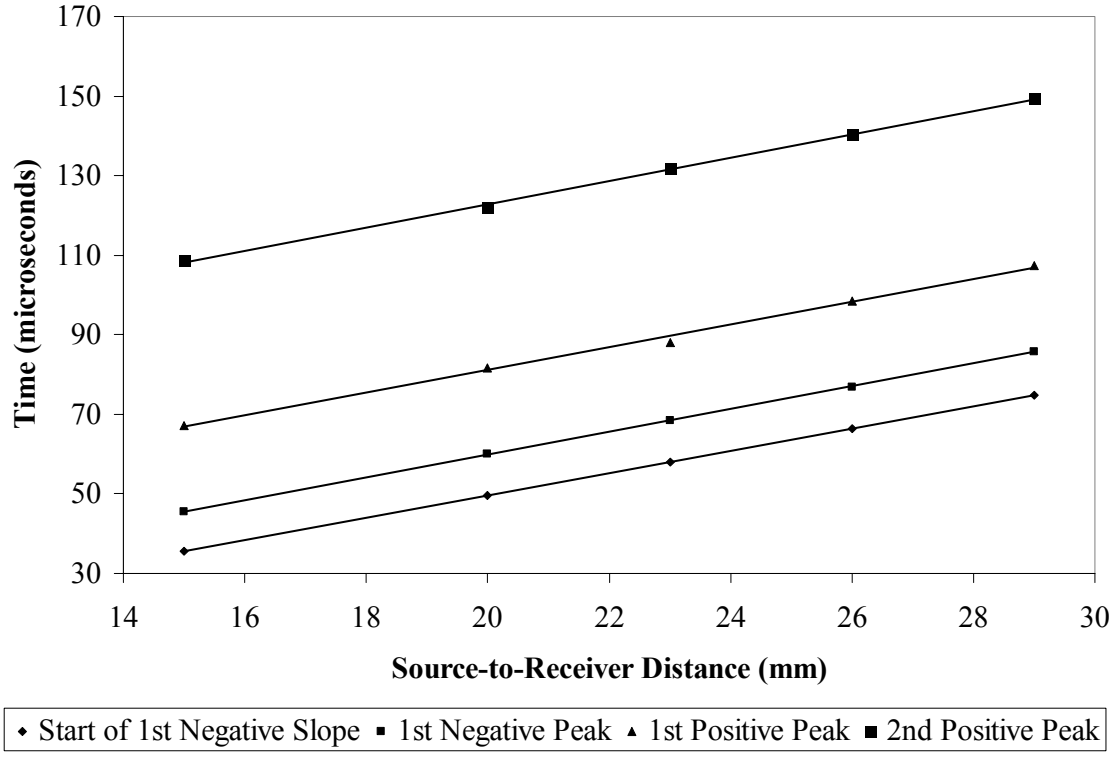

Figure 4.2.4. Arrival times for the first peaks of the Lamb waves detected by a 160 μm cMUT as a function of source-to-receiver distance at a MEMS-to-paper stand-off distance of 1 mm. Linear regression lines are presented for each peak.

.

One can also plot the amplitude dependence of the measured signal as a function of the source-receiver distance. Figure 4.2.5 and 4.2.6 show the amplitude of the first positive peak as a function of the source-receiver distance for stand-off distances of .3 mm and 1 mm. The decrease in amplitude for both stand-off distances is attributed to both the geometrical spreading associated with the propagation of the A_0 Lamb mode from a point source and also with the attenuation of the Lamb wave as it leaks energy into the surrounding air (on both sides of the paper sample). A detailed analysis of the leak rate of Lamb waves can be found in [38,44,45].

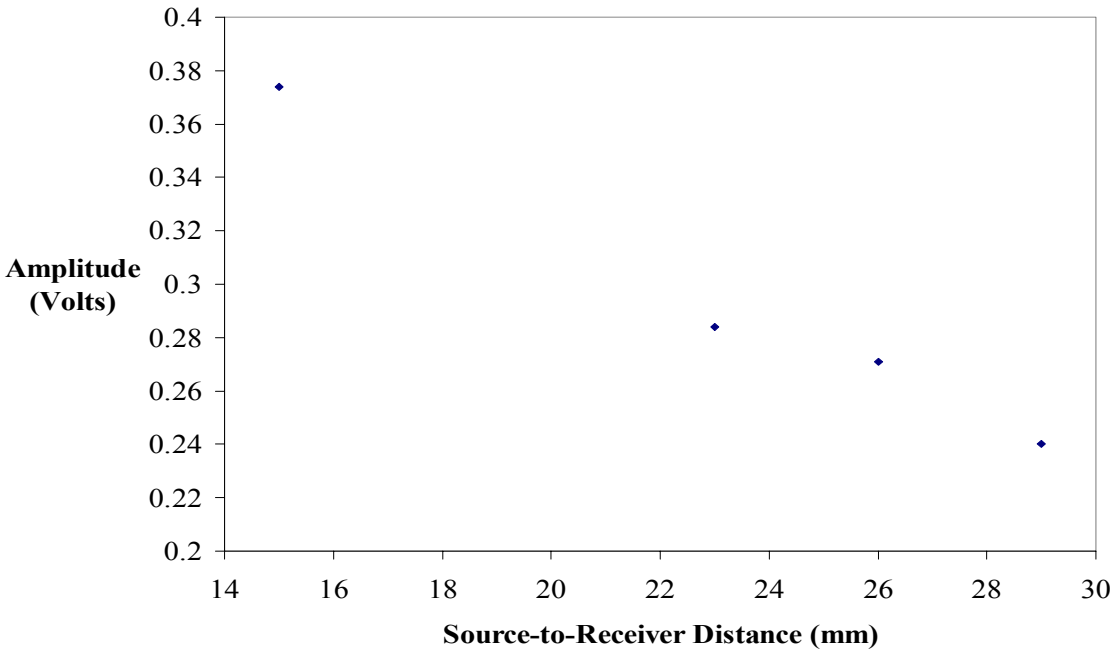

Figure 4.2.5. Amplitude of the first positive peak as a function of source-to-receiver distance for Lamb waves detected by a 160 μm cMUT at stand-off distance of less than .3 mm.

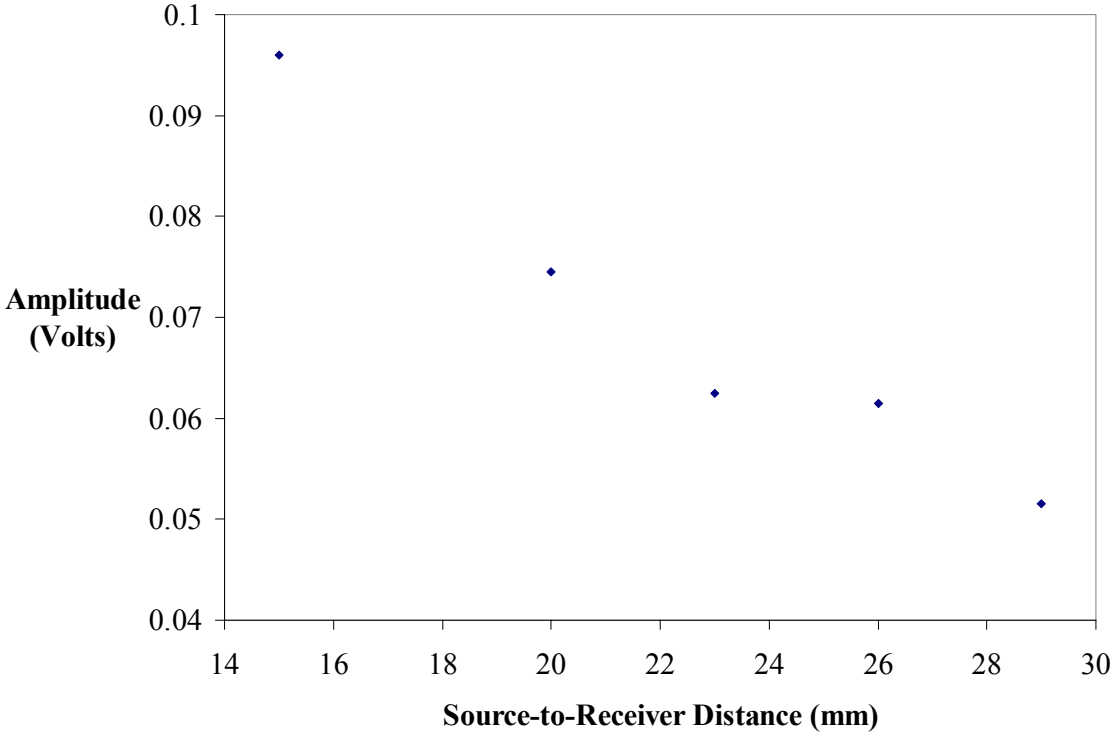

Figure 4.2.6. Amplitude of the first positive peak as a function of source-to-receiver distance for Lamb waves detected by a 160 μm cMUT at stand-off distance of 1 mm.

4.3 Measurements at Various Stand-off Distances

The next dependent variable that was tested was the effect of the MEMS-to-paper stand-off distance on the Lamb wave detection capabilities of the cMUT. Figure 4.3.1(a) depicts the waveform detected by the cMUT at a source-to-receiver distance of 15 mm and a MEMS-to-paper stand-off distance of less than .3 mm. It is apparent that the signal amplitude decreases with an increase in stand-off distance as Figures 4.3.1(b) to (d) depict. Also at larger source-to-receiver distances, as Figure 4.3.2(a) to (d) demonstrate, the wave signal decreases in amplitude with an increasing stand-off distance. This trend is graphically displayed in Figure 4.3.3. Finally, the wave signal also becomes increasingly noisy with greater stand-off distances as shown in both Figure 4.3.1 and 4.3.2. Instead of a clear waveform, more high frequency noise is present.

Nevertheless, it is interesting to note that even at a stand-off distance of 5 mm, the sensor detects a sharp negative pulse. Also, the results obtained at various stand-off distances convey that the arrival time of the wave signal is relatively independent of stand-off distance as Figures 4.3.4(a) and (b) convey. The calculated velocity of the first negative pulse for all stand-off distances at a source-receiver distance of 26 mm is 332 m/s, +/- 4 m/s. It is important to note that this value is within experimental error equal to the speed of sound in air. This will be discussed in more detail in Section 4.7.

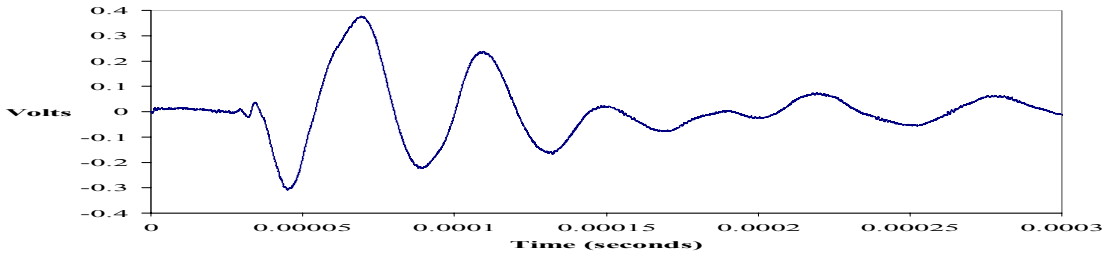

(a)

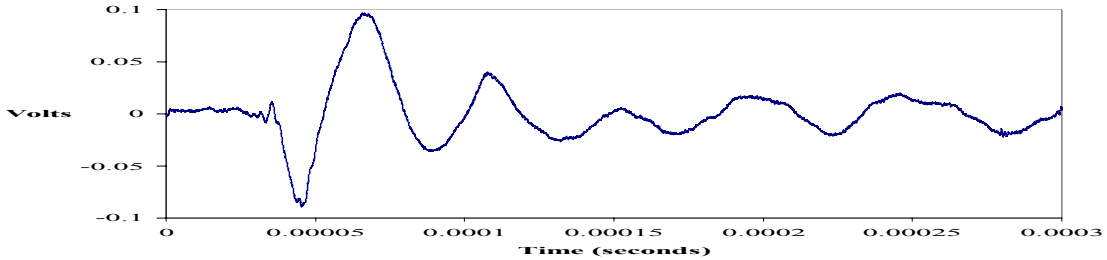

(b)

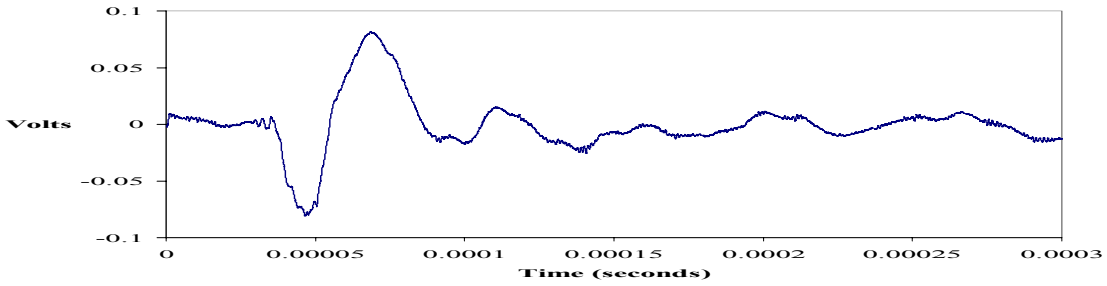

(c)

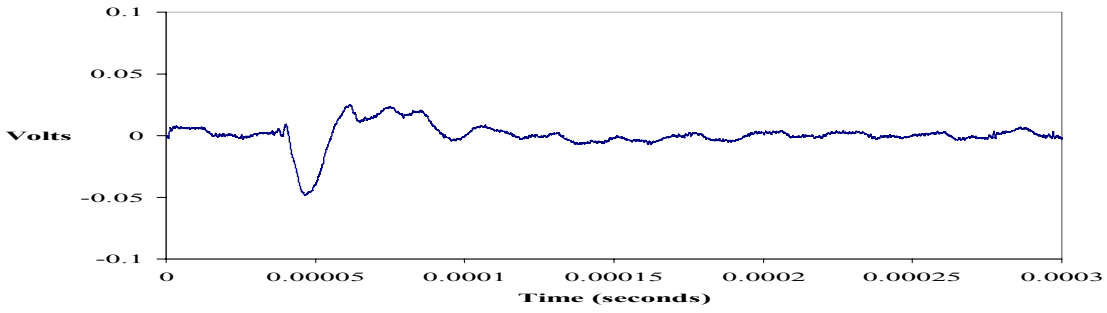

(d)

Figure 4.3.1. Waveforms detected by a 160 μm cMUT in raw stock 5914-3 paper at source-to-receiver distance of 15 mm and a MEMS-to-paper stand-off distance of, (a) .3 mm, (b) 1 mm, (c) 2 mm, and (d) 5 mm.

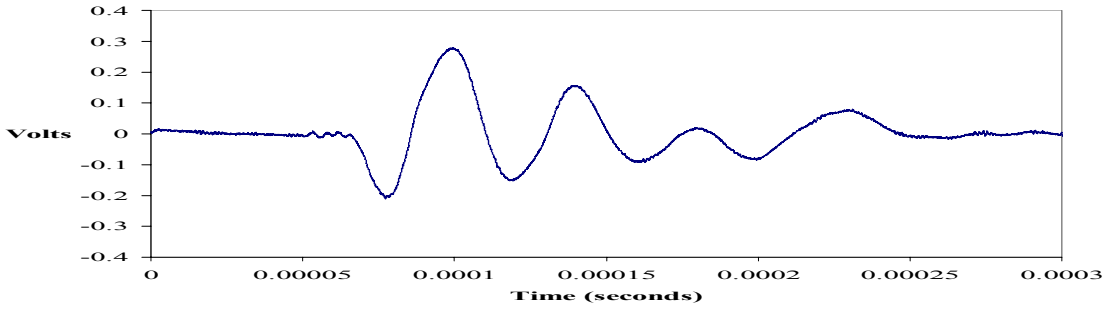

(a)

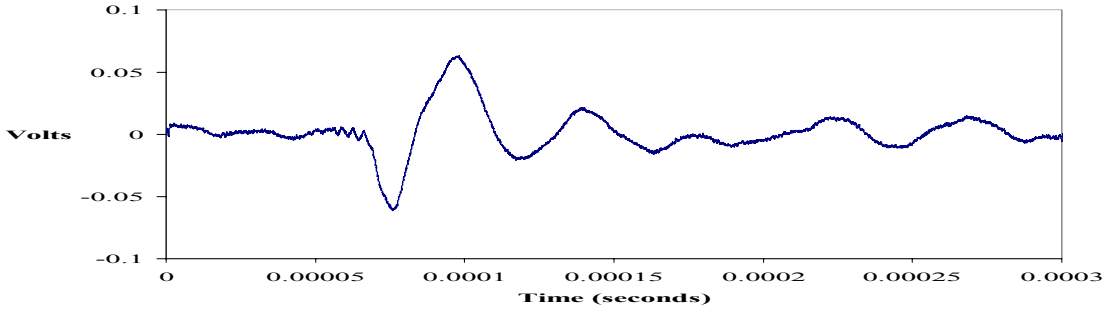

(b)

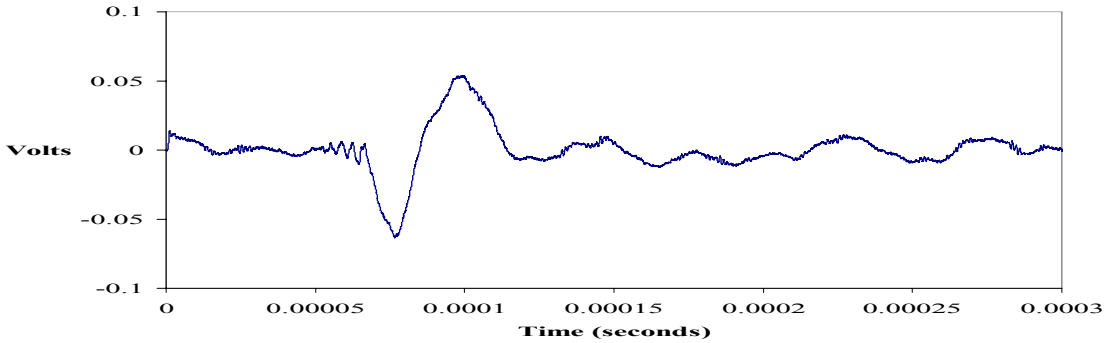

(c)

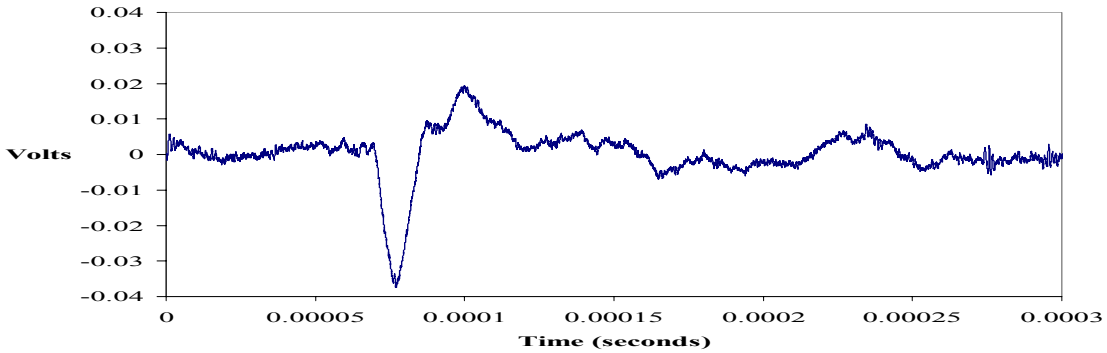

(d)

Figure 4.3.2. Waveforms detected by a 160 μm cMUT in raw stock 5914-3 paper at source-to-receiver distance of 26 mm and a MEMS-to-paper stand-off distance of, (a) .3 mm, (b) 1 mm, (c) 2 mm, and (d) 5 mm.

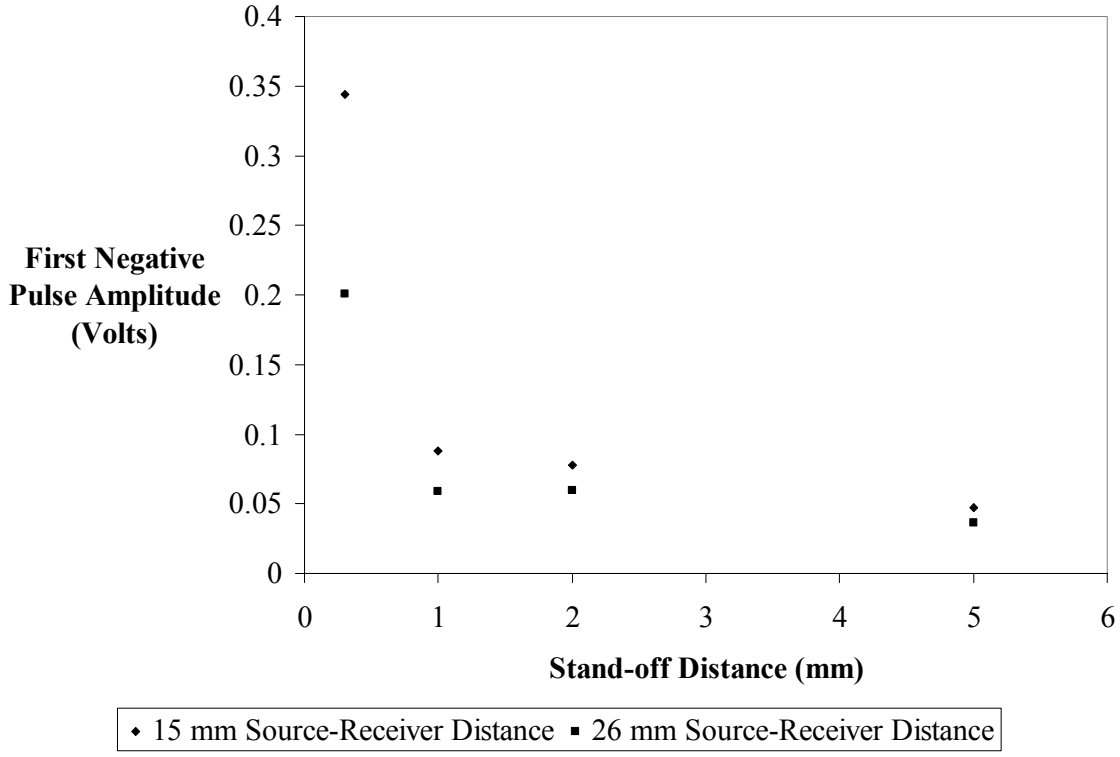

Figure 4.3.3. Amplitude of first negative peak for Lamb waves detected by a 160 μm cMUT as a function of stand-off distance. Source-receiver distances of 15 mm and 26 mm are presented.

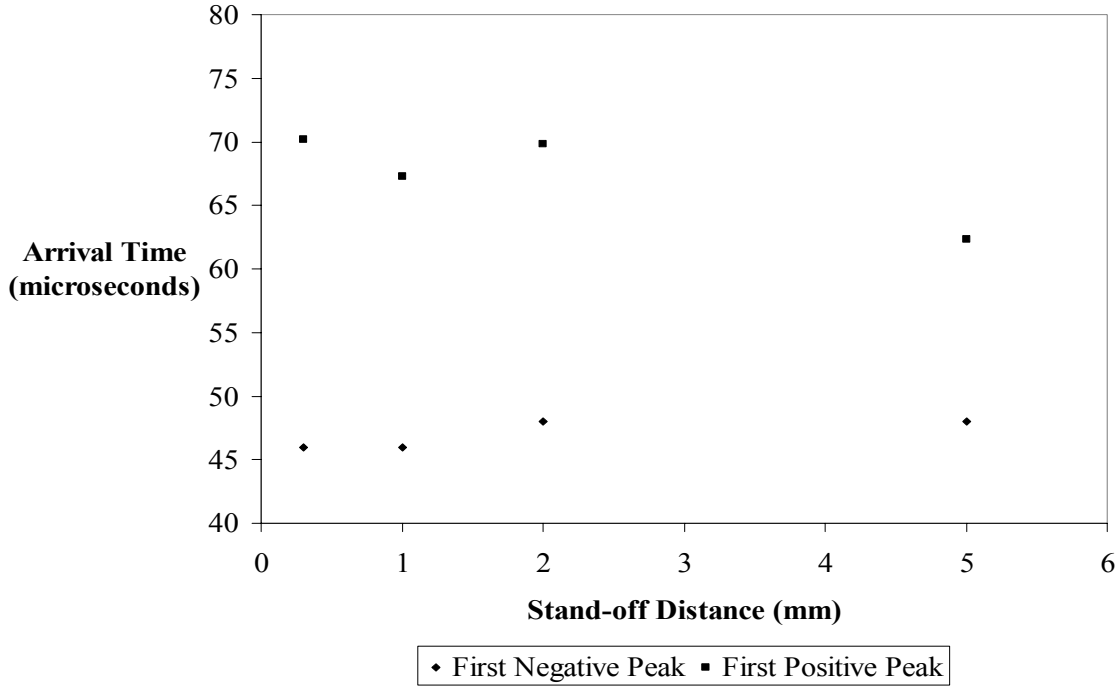

(a)

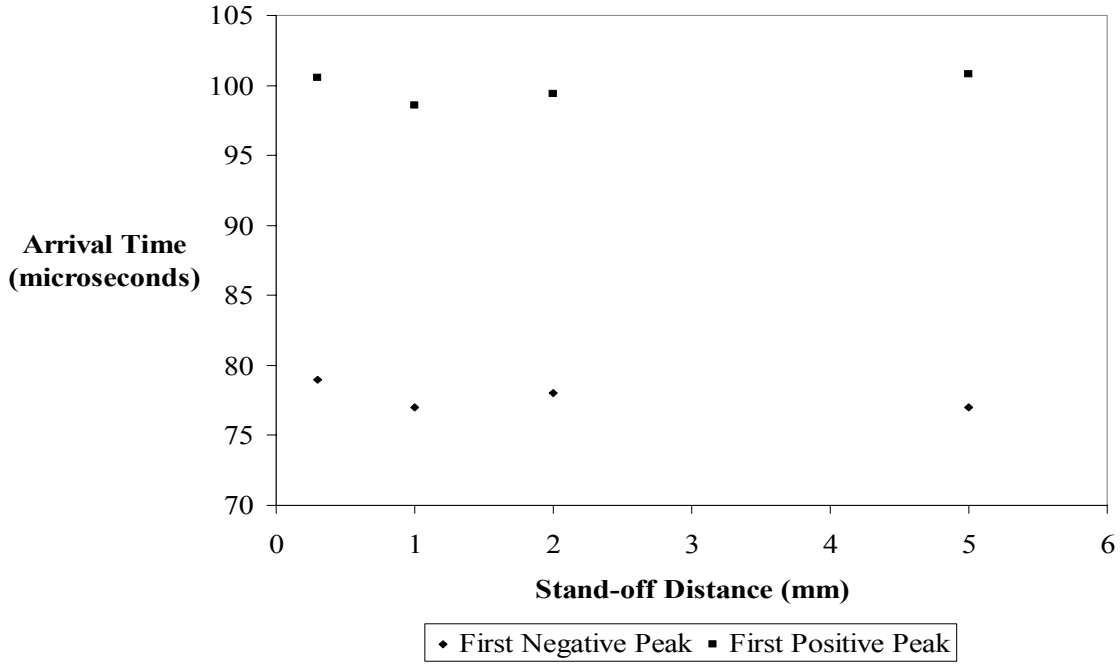

(b)

Figure 4.3.4. Arrival time of first negative and positive peaks for Lamb waves detected by a 160 μm cMUT at a source-to-receiver distance of (a) 15 mm and (b) 26 mm at a stand-off distance of .3, 1, 2, and 5 mm.

4.4. Signal-to-Noise Ratio

An estimate of the signal-to-noise ratio (SNR) can be obtained by computing the power spectral densities (PSD) of the signal detected by the cMUT and that of the noise. See Appendix D. The noise signal, of Figure 4.4.1, was obtained by blocking the Nd: YAG laser beam from hitting the sample of paper with a piece of cardboard. In this manner the fired Nd: YAG triggered the oscilloscope, but no ultrasonic wave was generated in the paper. The SNR was measured to be as high as 48 dB at the dominant frequency detected of 24 kHz. The frequency bandwidth of analysis used to the compute the FFTs of the signal is 1 kHz.

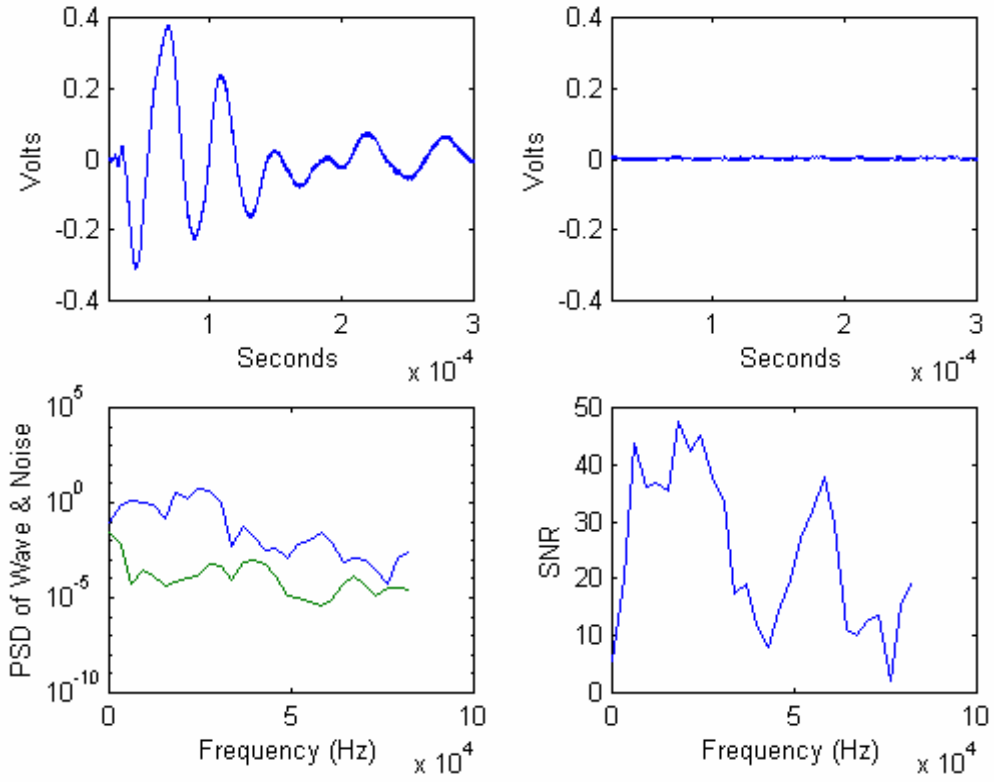

Figure 4.4.1. Beginning at top left plot and moving in a clockwise manner are the wave signal, noise signal, SNR, and power spectral density plots of a signal detected by a 160 μ m cMUT in raw stock 5914-3 paper at source-to-receiver distance of 15 mm and a MEMS-to-paper stand-off distance of less than .3 mm.

Figure 4.4.2 indicates that the SNR decreases, as expected, when the stand-off distance between the MEMS and the paper increases. The plots in Figure 4.4.2 explain this phenomenon by showing that the SNR decreases mainly due to the decrease in amplitude of the wave signal with increasing stand-off distance. The small plots to the left are close-up images of the first 25 μ s of the entire recorded signal to the immediate right . This portion of the signal magnified to the left is of the ambient noise the MEMS device detects before the signal arrives. Since the vertical scale is kept constant the background noise clearly decreases with an increase in stand-off distance.

It is important also to obtain a quantitative value of the SNR in decibels for the entire wave signal. This value was calculated according to equation 4.4.1, where $Vrms, signal$ is the root mean square of the amplitude, in volts, at each point in time of the detected signal and $Vrms, noise$ is the root mean square of the amplitude, in volts, at each point in time of the noise file.

$$SNR = 20\log_{10}\frac{Vrms, signal}{Vrms, noise} \tag{4.4.1}$$

The SNR of the wave signals in decibels decreased with increasing stand-off distances and decreased with increasing source-receiver distances. At a set stand-off distance the SNR varied no more than 5 dB when the source-receiver distance was adjusted. For instance, at a stand-off distance of .3 mm the SNR was calculated to be 29 dB and 34 dB at source-receiver distance of 29 mm and 15 mm respectively. The average SNRs for wave signals at a stand-off distance of .3, 1, 2, and 5 mm were calculated to be 32, 19, 18, and 16 dB respectively.

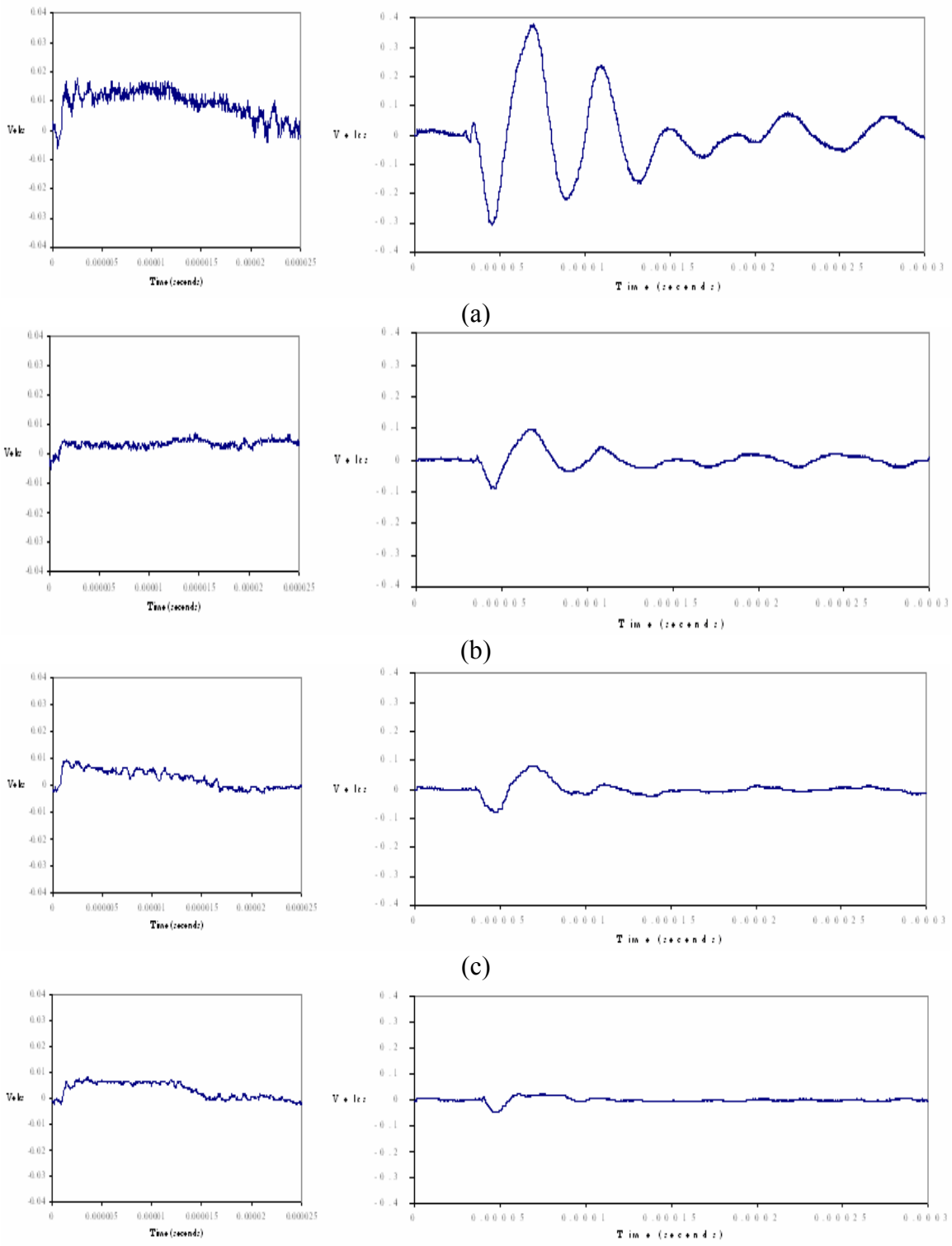

(a)

(b)

(c)

(d)

Figures 4.4.2. Plots on the right are of signals detected by a 160 μm cMUT in paper at varying stand-off distances of (a) .3 mm, (b) 1 mm, (c) 2 mm, and (d) 5 mm, but at a constant source-to-receiver distance of 15 mm. Plots on the left are close-up images of the first 25 μs of the corresponding wave signal to the immediate right.

4.5. Measurements with the Laser Interferometer

Figure 4.5.1 depicts an example of a waveform detected by the Mach-Zehnder Interferometer. This particular signal was recorded at a source-to-receiver distance of 26 mm. In Figure 4.5.1 higher frequencies arrive sooner and lower frequencies arrive later, similar to expected Lamb wave dispersive behavior. The SNR of the waveform in Figure 4.5.1 is presented in Figure 4.5.2. No portion of the signal has a SNR less than 20 and the group of frequencies surrounding 19 kHz exhibits an SNR as high as 50 dB. Both of these facts indicate that the signal detected by the interferometer is clearly a result of the Lamb wave generated by the Nd: YAG pulse laser. The SNR of the entire wave signal depicted in Figure 4.5.1 as defined previously by equation 4.4.1 is 22 dB.

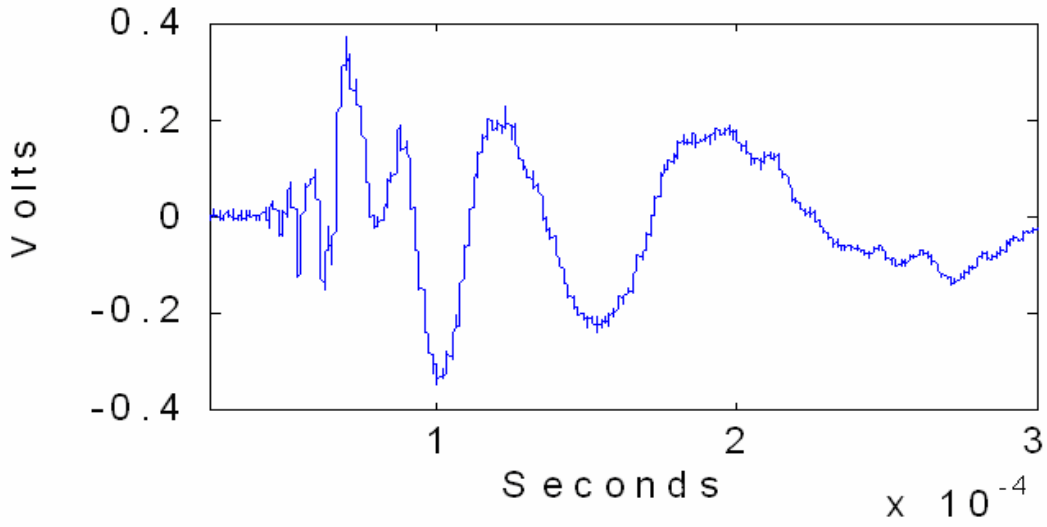

Figure 4.5.1. Waveform detected in raw stock paper 5914-3 by the interferometer. The source-to-receiver distance for this trial was 26 mm.

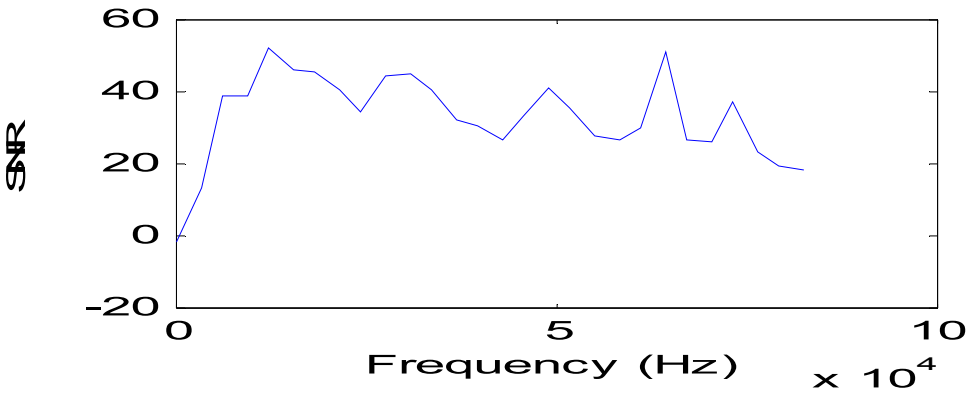

Figure 4.5.2. SNR plot generated for the waveform that was previously presented in Figure 4.5.1. The signal was detected in raw stock paper 5914-3 by the interferometer at a source-to-receiver distance of 26 mm.

4.6. Performance Comparisons of cMUT, Interferometer, & Laser Vibrometer

Figure 4.6.1 presents three Lamb waves at the same source-to-receiver distance of 26 mm. One Lamb wave is the signal detected by the cMUT at a stand-off distance of less than .3 mm. Another Lamb wave is a signal detected by the laser interferometer and the final wave is a Lamb wave generated computationally using material properties of paper and the A_0 dispersion curve.

By comparison of Figures 4.6.1(a) to (c) it is evident that the MEMS device does not detect high frequencies that are present in both the interferometer and predicted Lamb wave signals. The small ripples in the MEMS signal before the sharp negative dip is the MEMS' attempt at detecting these higher frequency Lamb waves. These ripples can be seen more clearly in the MEMS signals presented previously, such as, Figures 4.2.1(a) to (e).

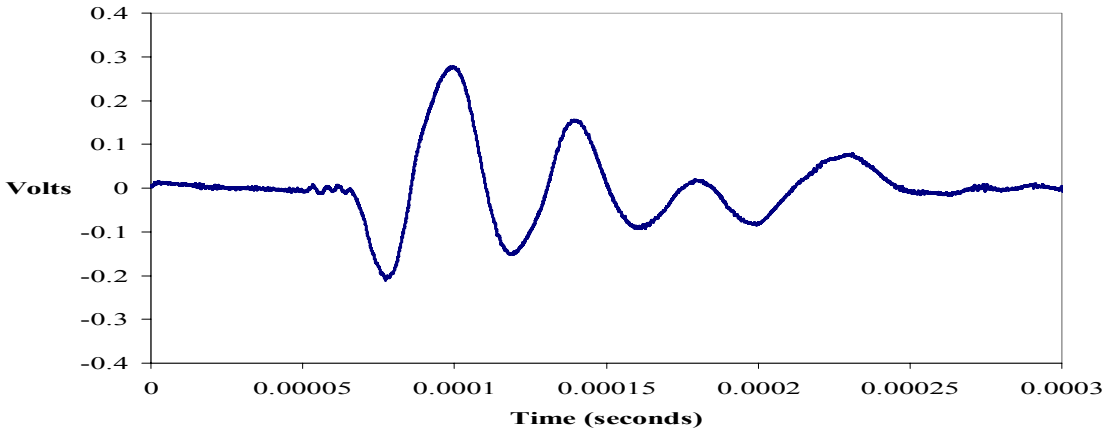

(a)

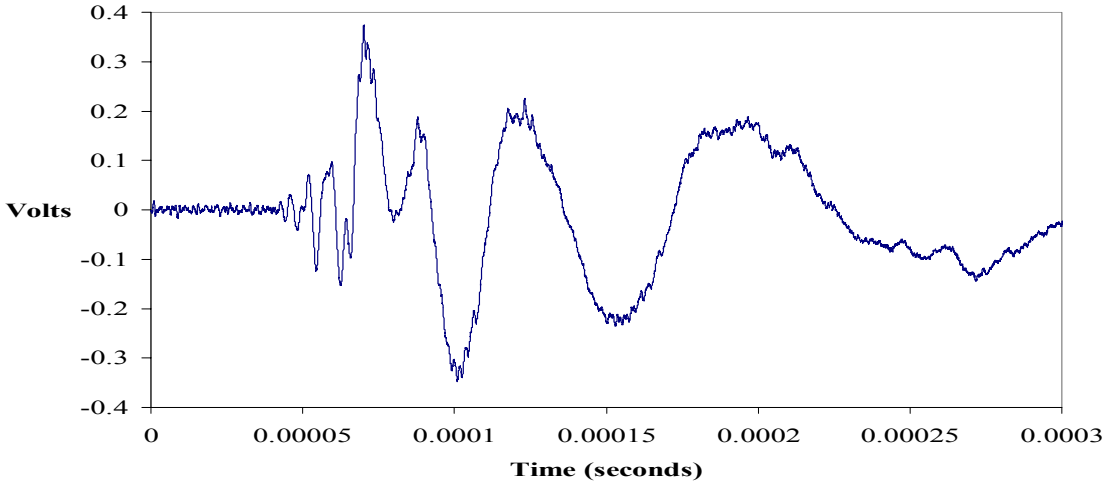

(b)

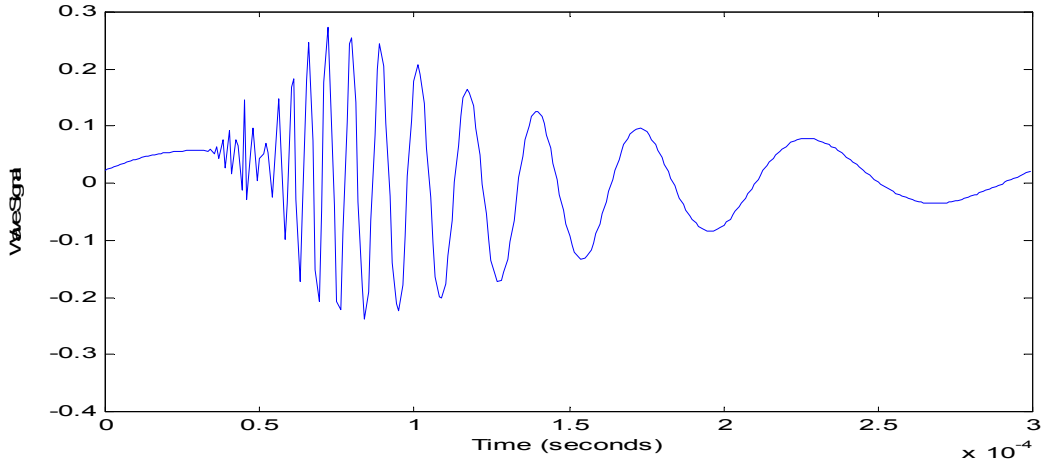

(c)

Figure 4.6.1. Lamb waves in raw stock paper 5914-3 at a source-to-receiver distance of 26 mm. (a) cMUT detection at a stand-off distance of less than .3 mm. (b) Inteferometer detection. (c) Predicted A_0 Lamb wave.

Beginning at the time of the first positive peak of the MEMS' signal, until 200 μs , in Figures 4.6.1(a) to (c), there is a uniform frequency among the three Lamb waves. Figure 4.6.2 displays FFT plots for wave signals detected by the cMUT and interferometer at a source-to-receiver distance of 26 mm. The frequency resolution of both plots is 1 kHz and magnitudes have not been adjusted. The first two peaks in the FFT of the cMUT signal are at 9 kHz and 15 kHz. The first two peaks of the FFT of the interferometer signal are at 8 kHz and 16 kHz. As discussed earlier in this thesis, and clearly shown in Figure 4.6.2, the cMUT's dominant frequency is a 24 kHz wave. Also demonstrated in Figure 4.6.2 is the cMUT's inability to detect higher frequency Lamb waves such as the 47 kHz and 58 kHz wave signals that the interferometer detects.

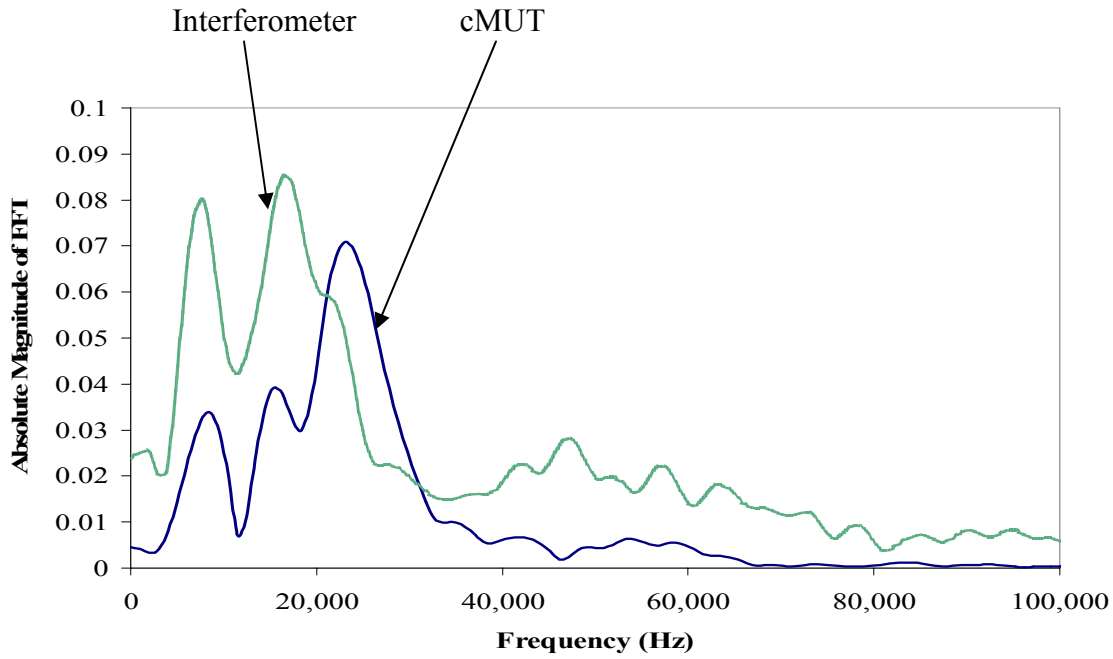

Figure 4.6.2. FFTs for wave signals detected by the interferometer and cMUT at a source-to-receiver distance of 26 mm. The wave signals for these FFTs are presented in Figure 4.6.1.

A performance comparison can also be made to the wave signals detected by the Compact Laser Vibrometer (CLV), mentioned previously in Section 4.1.4. Figure 4.6.3 and 4.6.4 present wave signals detected by the CLV at source-to-receiver distances of 26 mm and 23 mm respectively. As mentioned previously, the CLV detects a far greater range of frequencies than the cMUT at the given source-to-receiver distances. The peak of maximum positive displacement the paper experienced as recorded by the CLV in Figure 4.6.3 and 4.6.4 was hypothesized to be the main contribution of the 24 kHz signal detected by the cMUT. A direct measurement of the phase velocity of that component of the CLV signal can be obtained by comparing the time of arrival of that peak at two different source-receiver distances. Figure 4.6.5 shows the arrival times of this peak as a function of source-receiver distance. The inverse of the slope (2.9 $\mu s / mm$) in Figure 4.6.5 is a direct measurement of the phase velocity. It is found that this peak in the Lamb wave detected by the CLV propagates at a phase velocity of 345 m/s. This phase velocity is analogous to the phase velocity calculated in section 4.2 for the 24 kHz component of the wave signals detected by the cMUT.

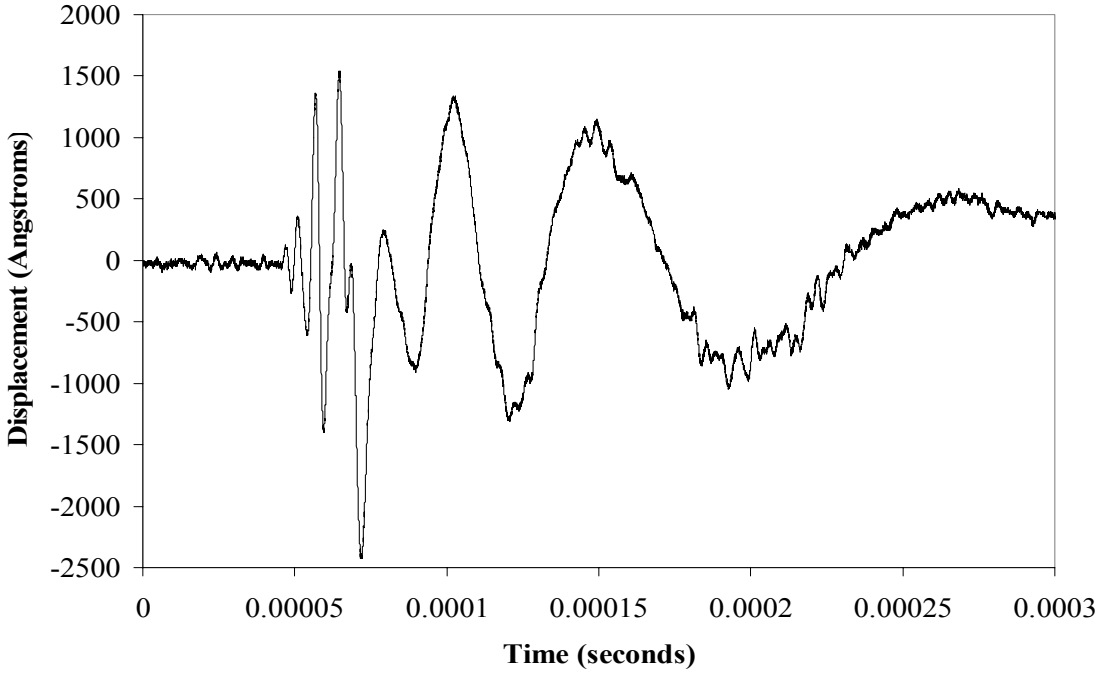

Figure 4.6.3. Paper displacement recorded by a Compact Laser Vibrometer at a source-to-receiver distance of 26 mm. Negative displacement simply indicates displacement away from the Vibrometer.

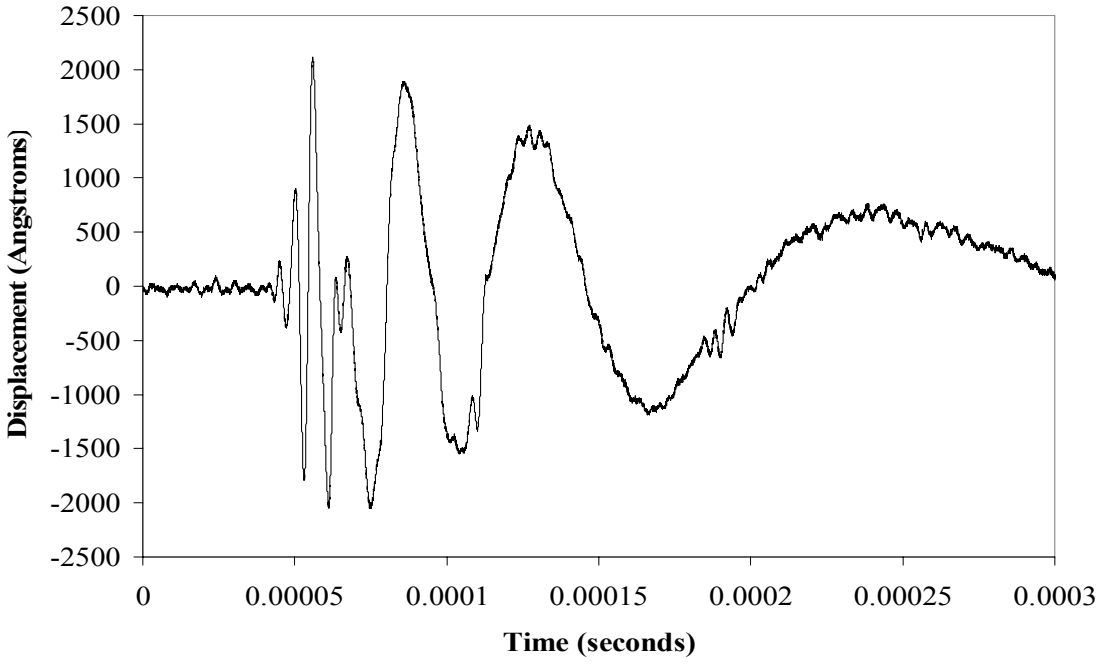

Figure 4.6.4. Paper displacement recorded by a Compact Laser Vibrometer at a source-to-receiver distance of 23 mm. Negative displacement simply indicates displacement away from the Vibrometer.

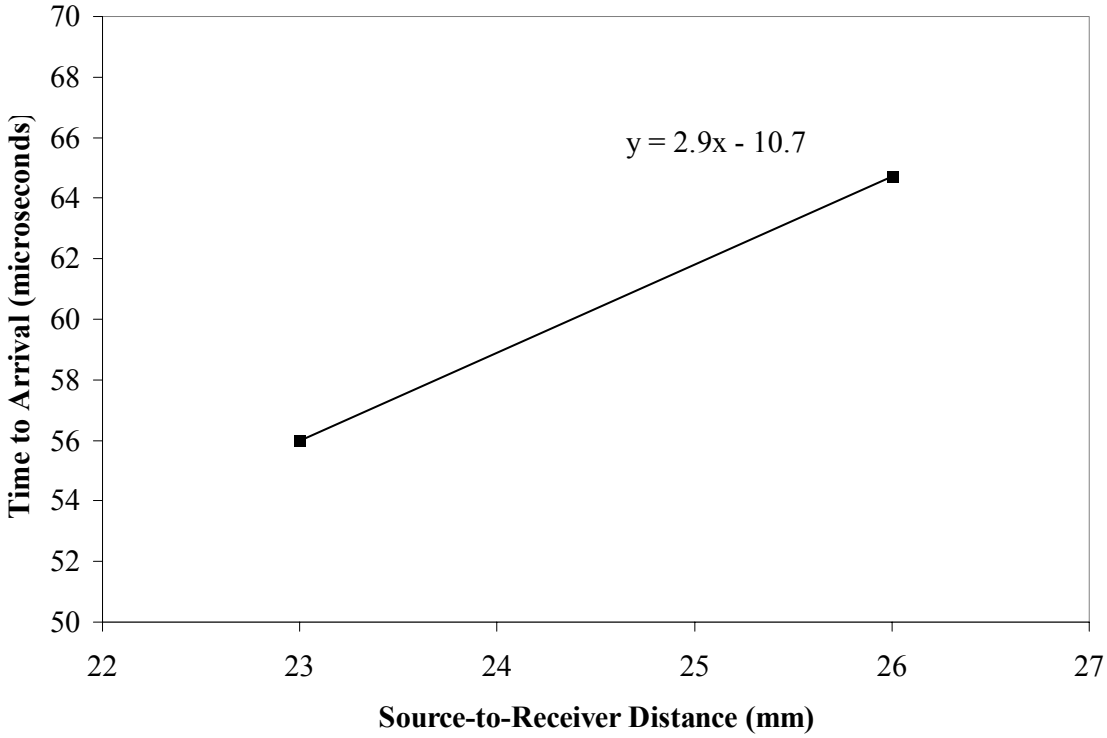

Figure 4.6.5. Arrival times of the positive peak with the greatest amplitude as a function of source-receiver distance for Lamb waves (see Figures 4.6.3 and 4.6.4) detected by a Compact Laser Vibrometer. A linear regression line and its corresponding equation is also displayed.

4.7. Discussion

As shown in Section 4.2 and Section 4.3, the MEMS sensor detects a pressure wave associated with the passage of an ultrasonic Lamb wave in the paper sample. The pressure wave is created in the air between the sample and the sensor by the so-called leaky Lamb wave mechanism [38,44,45]. Consider a harmonic Lamb wave (e.g. A_0 mode) propagating along the plate at a phase velocity C_{A0}. If $C_{A0} > C_0$, where C_0 is the sound speed in air, the Lamb wave is called supersonic and it sheds energy (leakage) into the surrounding medium. Physical considerations at the interface between the plate and

the air require that a plane wave be shed at an angle theta with respect to the normal such that $C_{A0} \sin(\theta) = C_0$., as shown in figure 4.7.1. In that case the normal velocity component of the Lamb wave, at the upper surface of the sample, is of the form

$$V(x,0,t) = V_0 \exp[j\omega(t - \frac{x}{C_{A0}})]\exp(-\alpha x) \qquad (4.7.1)$$

where alpha is the leak rate, i.e., the imaginary part of the propagation constant in the x direction.

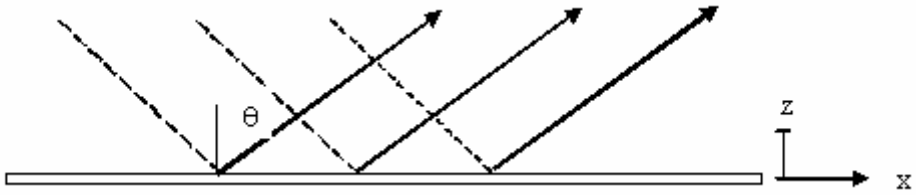

Figure 4.7.1. The supersonic Lamb wave leaks energy in the upper fluid and radiates sound. The dotted line represent the phase front, the solid arrows indicate the ray (wave vector) of the radiated wave. The amplitude of the traveling Lamb wave decreases exponentially as $\exp(-\alpha x)$.

It is well known that the leak rate is maximum, i.e., the acoustic pressure generated in air is maximum when the phase velocity of the Lamb wave exactly matches that in air, i.e., when $C_{A0}=C_0$. In that case, a traveling plane wave in air accompanies the traveling Lamb wave along the plate. The angle θ is equal to 90^o. This situation is illustrated in Figure 4.7.2.

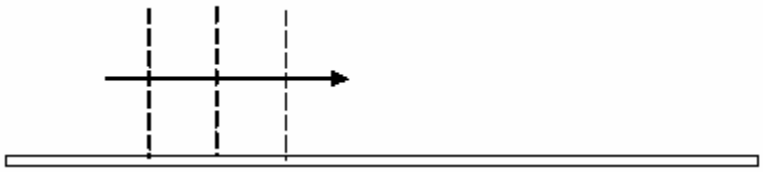

Figure 4.7.2. The Lamb wave travels exactly at the velocity of the sound speed in air. A plane wave is radiated along the plane. There is maximum leakage from the Lamb wave to the acoustic pressure wave.

When the phase velocity of the Lamb wave is less than the sound speed in the surrounding fluid, $C_{A0}<C_0$, the subsonic Lamb wave does not leak energy in the fluid. No sound is actually radiated from the plate to the fluid. The air is simply displaced hydrodynamically as the Lamb wave passes, but it is not compressed to produce a sound wave. In this subsonic case, the pressure disturbance in the fluid decays exponentially with height z. This type of pressure field is called an evanescent field, as illustrated in Figure 4.7.3.

Figure 4.7.3. The Lamb wave travels at a velocity that is below that of the sound speed in air. No sound is radiated into the air. The pressure amplitude decays exponentially from the plate.

Based on the data presented in Section 4.2 and 4.3, it appears that the pressure field generated by the Lamb wave corresponds to the transonic case illustrated in Figure

4.7.2. Indeed, the maximum acoustic pressure detected by the MEMS device corresponds to the case (maximum leak rate) where the Lamb wave travels at the sound speed in air. Even though the Lamb wave contains more than one frequency (as evidenced by direct measurement with the laser interferometer shown in Figure 4.1.7), the frequency that do not travel at the sound speed in air are attenuated either through the leakage (Figure 4.7.1) of supersonic waves or through exponential decay (Fig. 4.7.3) of subsonic waves. The result is that the MEMS device detects the frequency components that travel at the speed of sound in air, 24 kHz for the data shown in Figure 4.2.1 etc… Indeed, the phase velocity of the wave detected with the MEMS device is abut 350 m/s, +/- 5 m/s (see Figure 4.2.3) which corresponds to the sound speed in air, within experimental errors. Similarly, Figure 4.3.3, which shows the arrival times of the pressure signal (first negative pulse) as a function of stand-off distance, reveals that the arrival time is independent of stand-off distance, within experimental errors. This indicates that the wave front is indeed normal to the paper (θ=90^{o}). Also, the pressure amplitude does not vary drastically as the stand-off distance is increased (except for the case of a stand-off distance of 0.3 mm which will be discussed later). This also confirms that the wavefront is normal to the paper.

In reality, the situation is more complex than that just discussed because the MEMS device is placed in a wafer that acts as a rigid plate placed a small distance away from the paper sample, as illustrated in Figure 4.7.4. Under these circumstances, one can

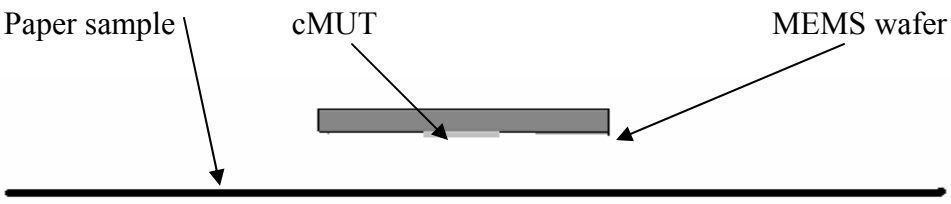

Figure 4.7.4. Illustration of cMUT attached to MEMS wafer close to the paper sample.

expect that acoustic waves in the air will be reflected back and forth between the paper sample and the upper plate, thus creating a waveguide effect. See Appendix E, which discusses the application of a cavity to the cMUT and its help in reducing the waveguide effect. If one models the upper plate and the paper sample as rigid interfaces, the lowest natural frequency would occur when the stand-off distance is half a wavelength in air. At a frequency of 24 kHz, one would expect such a resonance to occur when the gap is 344 / (2x24,000)= 7 mm. Waveguide effects can be expected for stand-off distances greater than 7 mm. In the present study, stand off distances were limited to 5mm so that waveguide effects can be ignored.

In summary, the data collected with the MEMS sensor seems to indicate that the sensor detects preferentially the Lamb wave frequency component that travels at the sound speed in air because it corresponds to the case of maximum leakage from the Lamb wave to the acoustic pressure wave.

CHAPTER 5

CONCLUSIONS & RECOMMENDATIONS

A MEMS optical microphone was used as a proximity sensor to detect ultrasonic plate waves propagating in paper. The ultrasound was generated by absorption of a Q-switched Nd: YAG laser pulse. The objective of the research was to investigate the capability of the MEMS sensor to detect such transient Lamb waves. The advantage of the MEMS detection over the more traditional non-contact method of laser interferometry is that many MEMS sensors can be placed on a single wafer, with a spacing of the order of a few millimeters that is particularly well suited for array detection at ultrasonic frequencies. This ability to detect ultrasound with large arrays of sensors, at a relatively low cost, offers new avenues for ultrasonic imaging.

A MEMS device designed and built in Dr. Degertekin's laboratory at Georgia Tech was tested in the context of Lamb wave detection. The sensitivity (output voltage for an incident pressure) of the sensor was found to be about 5 $\mu V / Pa$ at 20 kHz. The MEMS sensor was able to record signals with stand-off distances of 0.3 mm to 5 mm between the paper and the sensor. As expected, the signal amplitude detected with the MEMS sensor decreased when the stand-off distances increased. However, it was clearly observed that the arrival time of the signal did not increase by any statistically significant amount when the stand-off distance increased. The typical frequency detected by the MEMS sensor is around 24 kHz, with a corresponding measured Lamb wave velocity of about 350 m/s (+/- 6 m/s). This data seems to indicate that the sensor detects the Lamb wave frequency component that travels at the speed of sound in air.

The Lamb wave generated in the paper was also detected by a standard interferometer for comparison. Under our testing conditions, the typical positive displacement of the Lamb wave (A_0 mode) was measured to be about .2 μm and the corresponding voltage output from the MEMS sensor was about 300 mV, after amplification (x 20) and filtering.

The signal detected with the MEMS sensor had a narrower bandwidth (24 kHz +/- 1 kHz) than the signal detected by the optical interferometer (6 to 90 kHz, mostly centered in the 20-30 kHz range). Because of the narrow bandwidth of the signal detected with the MEMS sensor, the signal did not exhibit fully the standard A_0 mode dispersion characteristics with the higher frequencies arriving first, followed by the lower frequencies. Nevertheless, it was noted that the arrival time of the wave packet detected with the MEMS device was always defined very clearly (sharp negative pressure peak), even at the larger standoff distances of 5 mm. This offers excellent resolution when measuring Lamb wave velocities directly by time-of-flight (TOF).

The work presented in this thesis is completely experimental. It is intended only as a "proof-of-concept" validation that the MEMS device can be used as a proximity sensor to detect ultrasonic Lamb waves. Future work should include some detailed modeling of the Lamb wave interaction with the surrounding medium (air) in the presence of the MEMS wafer. A finite element code (ANSYS) could be used to better quantify the structure-fluid-structure interaction problem, and possibly to improve the design of the MEMS sensor for subsonic or supersonic Lamb wave detection. A second avenue of research would be to use the array detection capability of the sensor for directional detection in a preferential direction.

Appendix A

Matlab Program for Predicting A_0 Lamb Waveforms in Raw Stock 5914-3 Paper

```
L=26e-3; %propagation distance (m)

%%% source %%%
%%%%%%%%%%%%%%

T=300e-6;
delta=1e-6;
N=T/delta;
w=5e-6;

for j=0:N-1;
    t(j+1)=j*T/N;
    y(j+1)=(t(j+1)<=w)*sin(pi*t(j+1)/w);
end

figure(1); plot(t,y,'-bo'); grid;
xlabel('time (seconds)'); ylabel('source signal');

Y=fft(y);
Y_1=Y(1:round(N/2+1));

f=0:1/T:N/2*1/T;
om=2*pi*f;
figure(2); stem(f,abs(Y_1)); grid;
xlabel('frequency (Hz)'); ylabel ('abs(FFT(y))');


D=8.67e-4;
BW=.087; %grammage of my paper
mc=(D/BW)^.25;

for j=1:N/2+1
    beta(j)=2/mc*sqrt(om(j));
    R(j)=Y_1(j)*exp(-i*L*beta(j));
end

for j=N/2+1:N-1
    R(round(j+1))=conj(R(round(N-j+1)));
end

R_time=ifft(R);


figure(3); plot(t,real(R_time));
   xlabel('Time (seconds)'); ylabel('Wave Signal');
```

Appendix B

Predicted A_0 Lamb Waves in Raw Stock Paper 5914-3

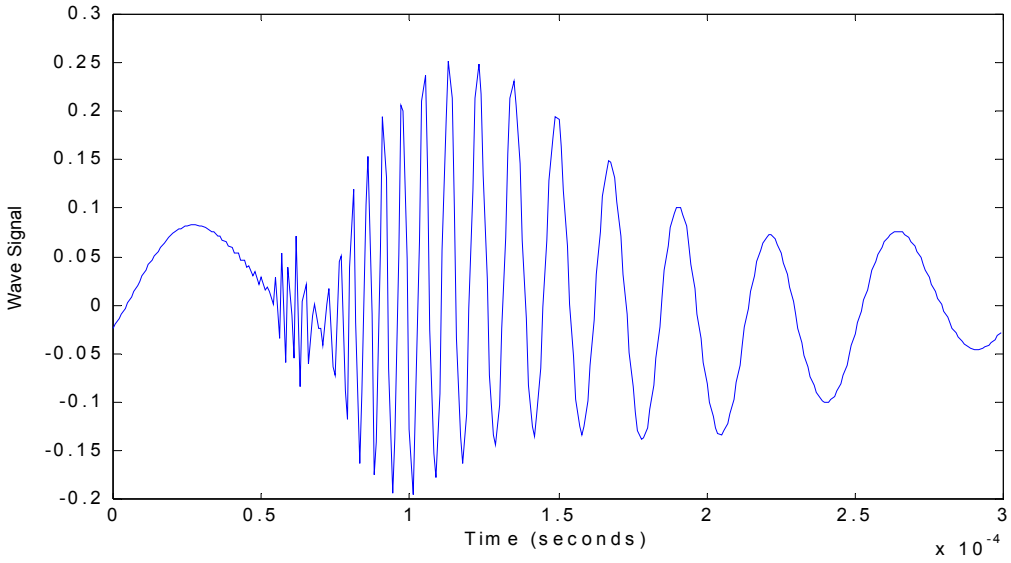

Figure B.1. Predicted A_0 Lamb wave at a source-to-receiver distance of 29 mm.

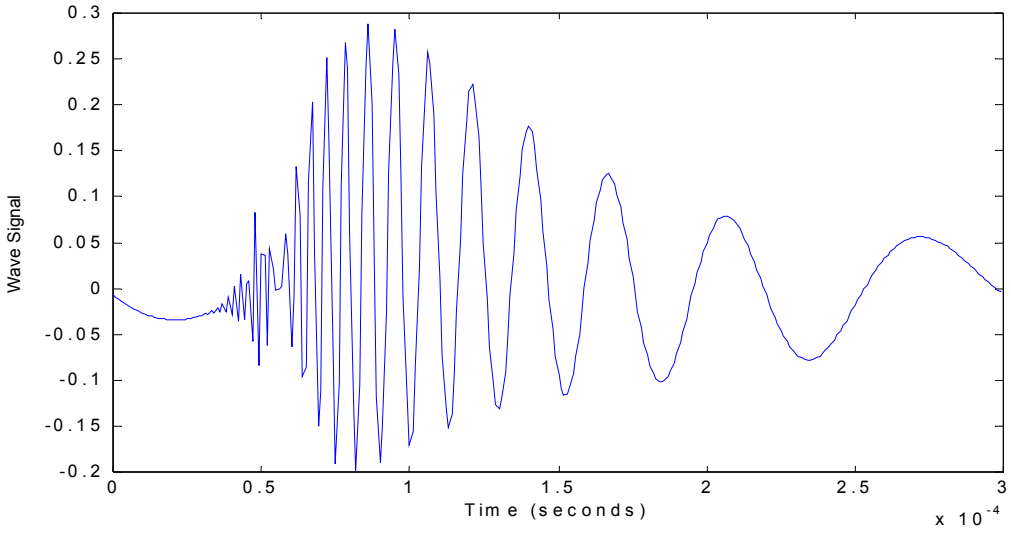

Figure B.2. Predicted A_0 Lamb wave at a source-to-receiver distance of 23 mm.

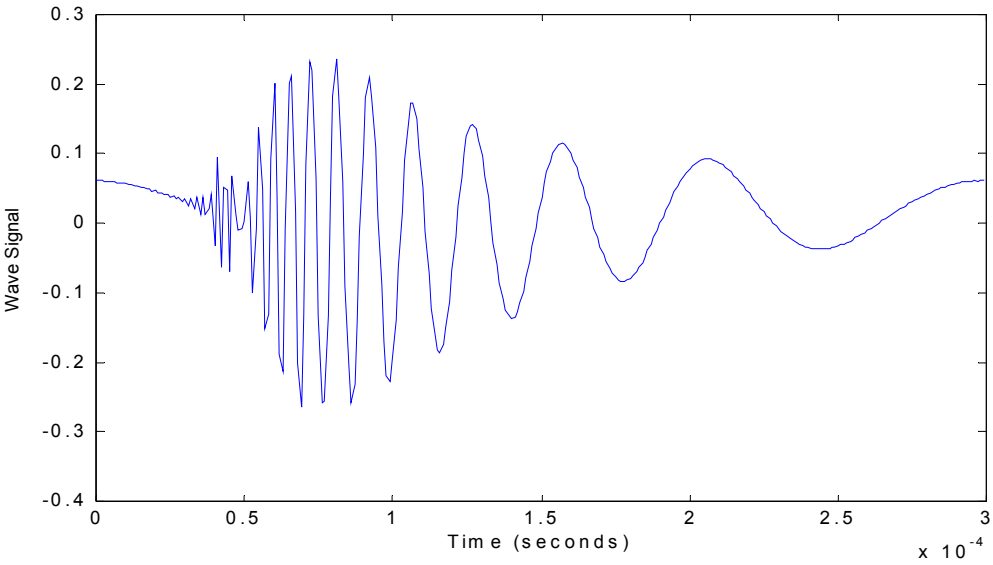

Figure B.3. Predicted A_0 Lamb wave at a source-to-receiver distance of 20 mm.

Appendix C

Spreadsheet with Results from LDV Calibration

DC Volts	μm/s	Membrane Deflection (μm/cycle)	Membrane Deflection (Å/cycle)
Traversing Up in Volts			
10	169.5	0.00026977	2.698
20	361.4	0.00057519	5.752
30	579.75	0.00092270	9.227
40	860.5	0.00136953	13.695
50	1360	0.00216451	21.645
Traversing Down in Volts			
10	151.64	0.00024134	2.413
20	363.1	0.00057789	5.779
30	509.2	0.00081042	8.104
30	544.7	0.00086692	8.669
30	564.4	0.00089827	8.983
30	537.81	0.00085595	8.560
40	688.5	0.00109578	10.958
40	852.5	0.00135680	13.568
Traversing Up in Volts			
30	526.84	0.00083849	8.385
40	547.1	0.00087074	8.707
50	1320	0.00210085	21.008

Appendix D

Matlab Program to Determine the Signal-to-Noise Ratio (SNR) of Recorded Waveforms

```
clc
clear
% Signal-to-noise ratio
%filename;
[filename, datadir] = uigetfile('*.txt','Choose data file to open');
fullfilename=fullfile(datadir,filename);
cd(datadir);
%noisefilename;
[noisefilename, noisedir] = uigetfile('*.txt','Choose noise file to
open');
noisefullpath=fullfile(noisedir,noisefilename);
[t,xb]=textread(noisefullpath,'%f%f');
[t,xa]=textread(fullfilename,'%f%f');

L=length(xa)                % length is usually 15000 points
NFFT=6800;                  % number of points in each FFT  (must be
less than L)


fs=25E6;                    %sampling rate =25Ms/s
dt=1/fs;                    %time resolution
T=300e-6;                   % duration

xa1=625;                    %row # of starting time for 25us MUST ADJUST
xa2=7500;                   %row # of ending time for 300us MUST ADJUST
xsignala=xa(xa1:xa2);       %received signal

xb1=625;                    %row # of starting time for 25us MUST ADJUST
xb2=7500;                   %row # of ending time for 300us  MUST ADJUST
xsignalb=xb(xb1:xb2);       %received signal


t1 = 25E-6;                 %starting time of window   MUST ADJUST
t2 = 300E-6;                %ending time of window   MUST ADJUST
t = t1:dt:t2;

xa(1:xa1) = 0;                 %zero padding for wave signal
xa(xa1:xa2)=xsignala;
xa(xa2:NFFT) = 0;

xb(1:xb1) = 0;                 %zero padding for noise signal
xb(xb1:xb2)=xsignalb;
xb(xb2:NFFT) = 0;

PSDxsignala=psd(xsignala,NFFT,fs);     % Power Spectral Density of
x1(Welch's average)
PSDxsignalb=psd(xsignalb,NFFT,fs);     % Power Spectral Density of x2
(Welch's average)

f=fs*(0:(NFFT/2-1))/NFFT;              % frequency axis
```

```
SNR=10*log10(PSDxsignala./PSDxsignalb);% signal-to-noise ratio  (per 1
Hz band)

subplot(2,2,1)
plot(t,xsignala)
AXIS([25E-6 T -.4 .4])
xlabel('Seconds')
ylabel('Volts')

subplot(2,2,2)
plot(t,xsignalb)
AXIS([25E-6 T -.4 .4])
xlabel('Seconds')
ylabel('Volts')

subplot(2,2,3)
Nmax=28;                    % max frequency index for the plot
semilogy(f(1:Nmax),PSDxsignala(1:Nmax),f(1:Nmax),PSDxsignalb(1:Nmax))
xlabel('Frequency (Hz)')
ylabel('PSD of Wave & Noise')

subplot(2,2,4)
plot(f(1:Nmax),SNR(1:Nmax))
xlabel('Frequency (Hz)')
ylabel('SNR')
```

Appendix E

Cavity Application to cMUT & Resulting Lamb Wave Detection Results

At certain frequencies Lamb waves are capable of traveling faster in planar material than sound waves travel in air. If this condition occurs pressure waves created by the Lamb wave can be detected by the cMUT after the actual arrival of the wave. This problem is more importantly compounded by the close proximity of the paper to the large MEMS chip holding the cMUTs. The small stand-off distance allows for pressure waves to reflect off the MEMS chip and reflect again off the paper muddling the resulting pressure wave that the cMUT finally detects.

Earlier, in Chapter 2 of this report, equation 2.5 was developed that modeled the A_0 Lamb wave group velocity as a function of the paper's flexural rigidity, basis weight, and angular frequency. This equation was formed by taking the limit of the group velocity as the Angular frequency approached zero. The disparity between the actual group velocity and the equation 2.5 was negligible until a frequency of around 20 kHz was reached.

$$C_{gr} = 2\sqrt{\omega}\left(\frac{D}{BW}\right)^{1/4} \tag{2.5}$$

According to equation 2.5 the critical frequency at which Lamb waves begin propagating in this type of paper supersonically, above 344 m/s, is 47 kHz. Based on the Lamb waves detected and discussed in this report, frequency values of 47 kHz can be expected to be detected. The cMUT has no way of adjusting the information it relays to the photodetector for subsonic or supersonic Lamb waves. Nor can the cMUT unsnarl the

wave reflections that occur between the paper and MEMS chip and only extract the actual Lamb wave propagating in the paper. We believed that attaching a cavity to the cMUT might help direct only pressure waves that were formed in front of the detection membrane onto the detection membrane itself.

Figure E.1 presents a side view illustration of the cavity and how it was incorporated into the experimentation to detect Lamb waves in paper. The cavity was simply made of a circular sheet of plastic 1.5 mm in diameter and .25 mm thick. A circular hole, .2 mm wide, was drilled in its center. The cavity was glued to the MEMS chip so that the drilled hole was directly above the cMUT detection membrane, creating a cavity around the cMUT unit being tested. All the aforementioned testing procedures and variables were held constant.

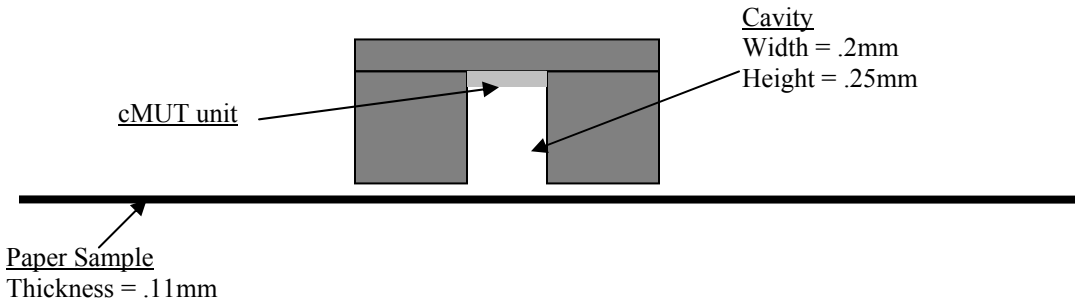

Figure E.1. Illustration of a cMUT with an attached cavity surrounding its detection surface.

The resulting waveform detected by the cMUT with a cavity attached to the MEMS chip can be seen in Figure E.2. The quality of the waveform does not seem much improved or to hold new information when compared to a waveform detected under

similar conditions without a cavity, Figure 4.2.1. With a cavity the waveform detected still exhibits a sharp time of arrival for all source-to-receiver distances. There was no appreciable difference in time of arrival for Lamb waves detected by the cMUT with the cavity to waves detected without the cavity. Another distinguishing characteristic of the waveform detected by the cMUT with an attached cavity is the sharp drop in the first peak of the wave.

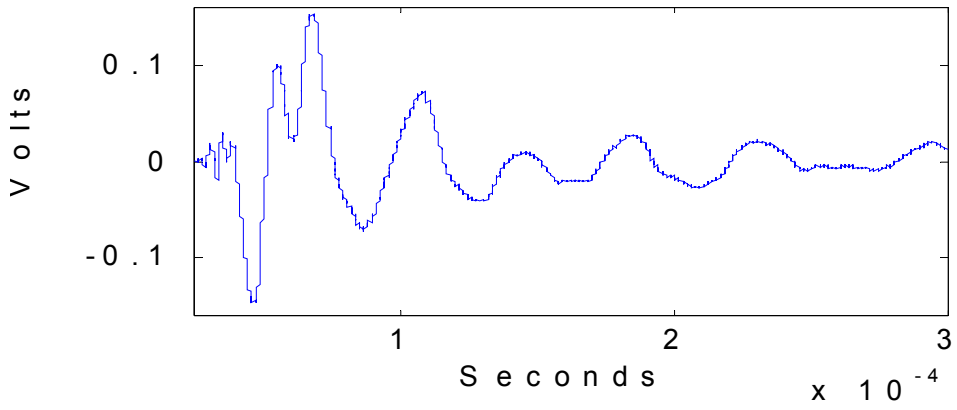

Figure E.2. Waveform detected by a 160 μm cMUT with an attached cavity in raw stock 5914-3 paper at source-to-receiver distance of 15 mm and a MEMS-to-paper stand-off distance of less than .3 mm.

With regard to deciphering the true wave arrival time for frequencies that propagated in paper above the speed of sound, a conclusion could not be reached based on the resulting signals. Expected improvements in the SNR of the waveform did not occur either with the attachment of the cavity. The SNR of the entire wave signal detected by the cMUT with a cavity was calculated to be 31 dB. Similar SNR values were obtained from signals detected by the cMUT without a cavity. A reduction in SNR of 20 dB at certain frequencies however is evident for the cMUT signal detected with a cavity, Figure

E.3. When compared to the SNR plot of a cMUT signal detected without a cavity at the same source-to-receiver distance, Figure 4.4.1, the reduction is noticeable. Similar to the cMUT results obtained without a cavity, the FFT of signals detected by the cMUT with a cavity, such as Figure E.4, demonstrate a dominant frequency around 24 kHz propagating with a phase velocity of about 350 m/s.

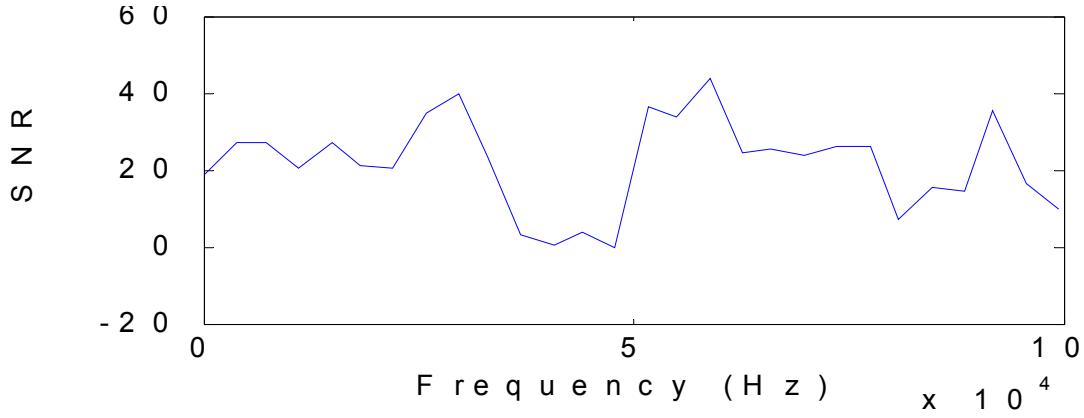

Figure E.3. SNR of the waveform, shown in Figure E.2, that was detected by a 160 μ m cMUT with an attached cavity in raw stock 5914-3 paper at source-to-receiver distance of 15 mm and a MEMS-to-paper stand-off distance of less than .3mm.

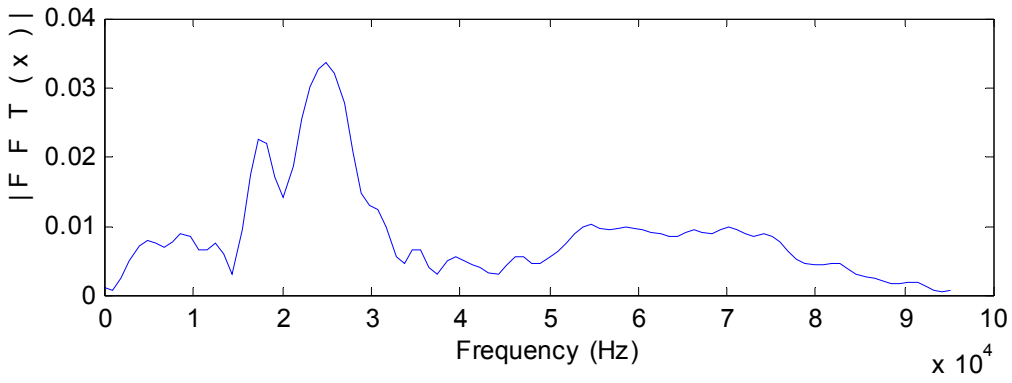

Figure E.4. FFT of the waveform, shown in Figure E.2, that was detected by a 160 μ m cMUT with an attached cavity in raw stock 5914-3 paper at source-to-receiver distance of 15 mm and a MEMS-to-paper stand-off distance of less than .3mm.

Appendix F

Optical Alignment Techniques for Laser Interferometer

Three portions of the experimental setup involving the laser interferometer need extended explanations: GRIN lens alignment, collimation, and the maintaining a 40 MHz Bragg signal.

F.1. GRIN Lens Alignment

The GRIN lenses of the target beam that transmitted and received laser light from the 20X objective lens near the paper sample could be carefully positioned so to increase the amount of scattered light off the target that was captured by the interferometer. The following procedure was performed to achieve this end:

1. The objective lens and paper target were removed from the experimental setup.
2. A sheet of white paper (a few inches square) was taped to a flat piece of cardboard of similar dimensions. The cardboard was positioned in a perpendicular manner approximately 2 feet from the exit of the entering fiber's GRIN lens. A green spot would appear on the sheet of paper from the Argon laser.
3. A He/Ne laser beam was directed into the return fiber's GRIN lens, which during experimentation transmits the target beam onto the 50/50 cube. Now a red spot from the He/Ne laser beam can be seen on the sheet of paper on the cardboard in addition to the green spot created by the Argon laser beam originating from the entering fiber. In summary the GRIN lenses were directing two different color beams onto the paper. See Figure F.1.

4. Using the screws shown in Figures F.1 the GRIN lenses and fiber cables could be positioned so to have both the red He/Ne laser spot and the green Argon laser spot overlap upon one another. Having the beams overlap at this distance from the target beam exit of the GRIN lenses ensured that the maximum amount of scattered light off the paper target during experimentation would be directed into the multimode fiber.
5. The He/Ne laser beam was turned off and removed from the lab bench and the interferometer was prepared further for experimentation.

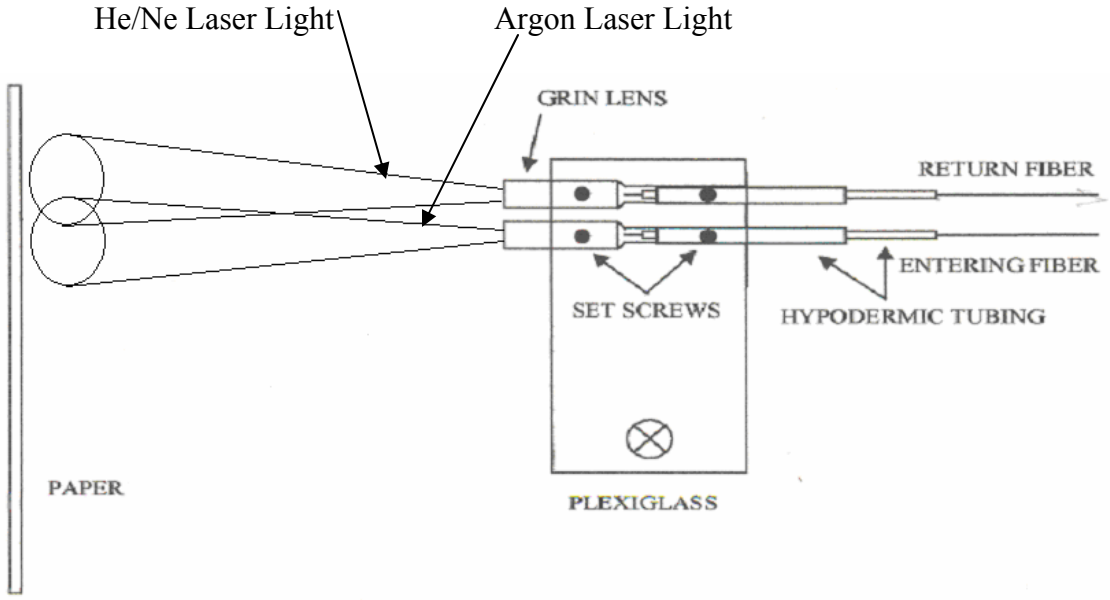

Figure F.1. Top view schematic of GRIN lens alignment method for the laser interferometer.

F.2. Collimation

Collimation used the same two laser beam methodology that was used for GRIN lens alignment. This time however the He/Ne laser beam was directed into the return fiber at the GRIN lens nearest to the target, so the He/Ne laser beam entered the

return fiber just at the scattered light from the target enters the return fiber. See Figure F.2. The following procedure was performed to achieve collimation:

1. The Objective lens and paper target were removed from the lab bench.

2. A piece of paper was placed a few feet away from the 50/50 cube so that a green spot a few inches in diameter, from the reference beam laser light, appeared on the paper.

3. As illustrated in Figure 3.4.3 the 50/50 cube would also reflect at 90° angle 50% of the beam that was transmitted through the cube. The He/Ne laser beam is reflected at such an angle and it creates a spot a few inches in diameter on the piece of paper in it's path.

4. The translation stages holding the GRIN lenses directing laser light upon the 50/50 cube are adjusted so the two different color spots overlap upon the paper. When the spots overlap at any given distance the paper is held from the 50/50 cube beam collimation has been reached.

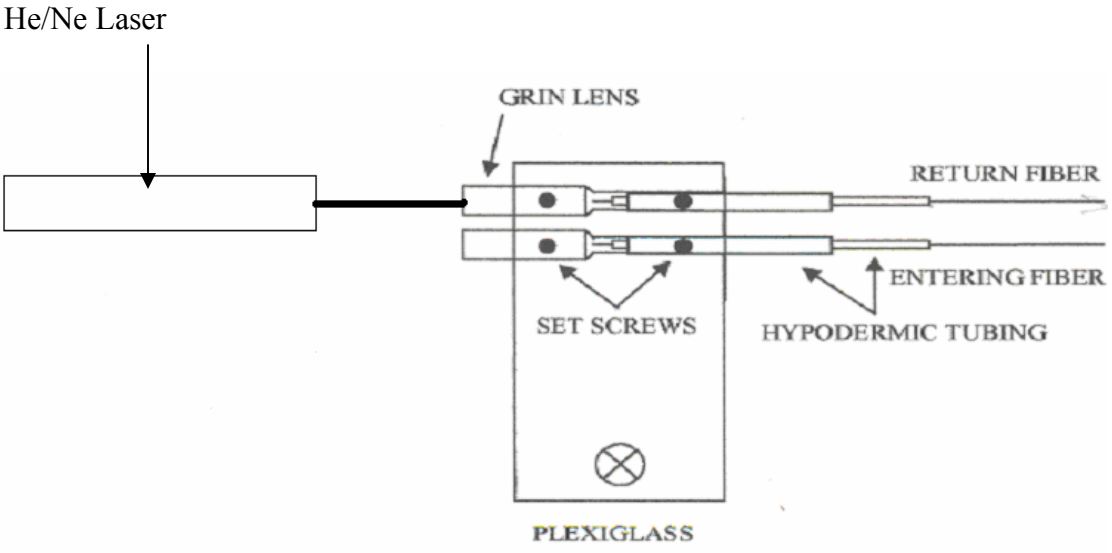

Figure F.2. Top view schematic of how the He/Ne laser was applied to collimate the target and reference beam of the laser interferometer.

F.3. Maintaining a 40MHz Bragg Signal

After the GRIN lenses have been aligned and the target and reference beam have been collimated and recombined and are directed onto the photodetector a 40 MHz Bragg signal needs to be obtained to begin interferometric testing. The following procedure was performed to achieve a 40 MHz Bragg signal:

1. The bandpass filter and attenuator were removed from the path of the BNC cable that connected the photodetector with an oscilloscope in the lab.
2. The paper target was positioned at the optimum distance from the objective lens, so the return fiber collected the maximum amount of scattered light. As explained earlier in the report, this is done visually by monitoring the intensity of the light exiting the target beam onto the 50/50 cube. By adjusting the translation stage that the paper and frame are attached to the maximum intensity can be reached.
3. Now all the translation stages are adjusted to bring a reasonable 40 MHz signal to the oscilloscope.
4. Once a 40 MHz signal is obtained the bandpass filter is placed in the path of the electrical signal traveling from the photodetector to the oscilloscope.
5. Again all the translation stages are adjusted to maximize the peak to peak voltage of the 40 MHz signal. This is an iterative process. For example, once the translation stage holding the return fiber of the target beam is adjusted, all the other translation stages need to be finely tuned again. Likewise, once the translation stage holding the paper sample is positioned to a point that maximizes the 40 MHz signal the translation stages of the other components of the

interferometer need to be maximized once more. This is continuously done until a max peak to peak voltage is reached for the 40 MHz signal. For our experimentation a 2 Volt peak to peak voltage of 40 MHz was obtained with a power output setting of 3.5 mW from the Argon laser.

REFERENCES

[1] M. Cornwell, Y. H. Berthelot, and C. C. Habeger, "Noncontact determination of the bending stiffness of paper using laser ultrasonics and wavelet analysis: effects of temperature and moisture content," Appeared in the Proceedings of the 2001 IEEE International Ultrasonics Symposium (2002).

[2] P. L. Ridgway, A. J. Hunt, M. Quinby-Hunt, and R. E. Russo, "Laser ultrasonics on moving paper," Ultrasonics, Vol. 37, 395-403 (1999).

[3] Hall, Neal A. and F. Levent Degertekin, "Self Calibrating Micro machined Microphones with Integrated Optical Displacement Detection", G.W. Woodruff School of Mechanical Engineering Georgia Institute of Technology Atlanta GA 30332 (2002).

[4] Neal A. Hall and F. Levent Degertekin, "Integrated Optical Interferometric Detection Method for Micro machined Capacitive Acoustic Transducers", Applied Physics Letters, Volume 80, Number 20, 2002.

[5] C.B. Scruby and L.E. Drain, Laser Ultrasonics: Techniques and Applications, Adam Hilger, Bristol, Philadelphia and New York (1990).

[6] M. A. Johnson and Y. H. Berthelot, "Laser ultrasonics in copy paper," Opt. Eng. Vol. 36, No. 2, 408-416 (1997).

[7] I. Ladabaum, B. T. Khuri-Yakub, and D. Spolianski, Appl. Phys. Lett. 68, 7 (1996).

[8] K.F. Graff, Wave Motion in Elastic Solids. Dove, New York P. 236 (1975).

[9] D. A. Griggs, " A laser-based ultrasonic system to measure the mechanical properties of paper products in a controlled," Master Thesis, Georgia Institute of Technology, April 2001.

[10] Y. H. Berthelot, E.F. Lafond, Contactless Real-Time Monitoring of Paper Mechanical Behavior During Papermaking, Phase I, Institute of Paper Science and Technology, Georgia Institute of Technology, P.44, 154, 172 (1998).

[11] C. C. Habeger, R. W. Mann, and G. A. Baum, "Ultrasonic plate waves in paper", Ultrasonics, Vol. 17, 57-62 (1979).

[12] D. A. Hutchins and K. A. Lundgren, "A laser study of transient Lamb waves in thin materials," J. Acoust. Soc. Am., Vol. 85 (4), 1441-1448 (1989)

[13] Hall, Neal A., "Micromachined Broadband Acoustic Transducers with Integrated Optical Displacement Detection," in Proposal pp.4-6, (Nov. 2003)

[14] D. E. Chimenti, "Guided waves in plates and their use in materials characterization," Appl. Mech. Rev., 50(5), 247-284 (1997)

[15] Hall, Neal A, Matlab generatated Mechanical Sensitivity model for cMUT at various frequencies.

[16] M. A. Cornwell, " Determination of the bending stiffness of copy paper and its dependence on temperature and moisture using laser ultrasonics Lamb waves", Master Thesis, Georgia Institute of Technology, December 2001.

[17] Zhao, Yanzhu, Research Report, Unpublish, Georgia Institute of Technology, (August, 2002)

[18] M. Luukkala, P. Heikkila, and J. Surakka, "Plate wave resonance- a contactless test method," Ultrasonics, Vol. 10, 201-208 (1971)

[19] M. Khoury, G. Tourtollet, and A. Schroder, "Contactless measurement of elastic Young's modulus of paper by an ultrasonic technique," Ultrasonics, Vol. 37, 133-139 (1999).

[20] D. Schindel and D. A. Hutchins, "Applications of micro-machined capacitance transducers in air-coupled ultrasonics and nondestructive evaluation," IEEE Trans. Ultrason. Ferroelec. Freq. Control, Vol 42(1), 51-58 (1995)

[21] M. Castaings and P. Cawley, "The generation, propagation, and detection of Lamb waves in plates using air-coupled ultrasonic ransducers," J. Acoust. Soc. Am., Vol.100(5), 3070-3077 (1996)

[22] K. L. Telschow and V. A. Deason, "Imaging laser ultrasonics measurement of the elastodynamic properties of paper," ," Appeared in the Proceedings of the 2001 IEEE International Ultrasonics Symposium (2002).

[23] A. Bonnin, R. Huchon, and M. Deschamps, "Ultrasonic waves propagation in absorbing thin plates: Application to paper characterization," Ultrasonics, Vol. 37, 555-563 (2000).

[24] B. Hosten, "Reflection and transmission of acoustic plane waves on an immersed orthotropic and viscoelastic solid layer," J. Acoust. Soc. Am., 89(6), 2745-2752 (1991)

[25] A. G. Every and W. Sachse, "Determination of the elastic constants of anisotropic solids from acoustic wave group velocity measurements," Phys. Rev. B 42, 8196-8205 (1990)

[26] B. Castagnède, J. T. Jenkins, and W. Sachse, "Optimal determination of the elastic constants of composite materials from ultrasonic wave-speed measurements," J. Appl. Phys. 67(6), 2753-2761 (1990)

[27] B. Castagnède, K. Y. Kim, W. Sachse, and M. O. Thompson "Determination of the elastic constants of anisotropic materials using laser-generated ultrasonic signals," J. Appl. Phys. 70(1), 150-157 (1991)

[28] S. I. Rokhlin and W. Wang, "Double through-transmission bulk wave method for ultrasonic phase velocity measurement and determination of elastic constants of composite materials," J. Acoust. Soc. Am., 91 (6), 3303-3312 (1992)

[29] S. I. Rokhlin and W. Wang, "Measurements of elastic constants of very thin anisotropic plates" J. Acoust. Soc. Am., 94 (5), 2721-2730 (1993)

[30] J.-C. Cheng and Y. H. Berthelot, "Theory of laser-generated transient Lamb waves in orthotropic plates," J. Phys. D: Appl. Phys. 29, 1857-1867 (1996)

[31] J.-C. Cheng and S.Y. Zhang, "Quantitative theory for laser-generated Lamb waves in orthotropic thin plates," Appl. Phys. Lett., 74(14), 2087-2089 (1999)

[32] M. Deschamps and C. Bescond, "Numerical method to recover the elastic constants from ultrasound group velocities," Ultrasonics, 33(3), 205-211 (1995)

[33] B. Audoin, C. Bescond, and M. Deschamps, "Measurement of stiffness coefficients of anisotropic materials from pointlike generation and detection of acoustic waves," J. Appl. Phys., 80(7), 3760-3771 (1996)

[34] S. Guilbaud and B. Audoin, "Measurement of the stiffness coefficients of a viscoelastic composit material with laser-generated and detected ultrasound," J. Acoust. Soc. Am., 105(4), 2226-2235 (1999)

[35] N. Leymarie, C. Aristégui, B. Audoin, and S. Baste, "Identification of complex stiffness tensor from waveform reconstruction," J. Acoust. Soc. Am., 111(3), 1232-1244 (2002)

[36] J.-B. Han, J.-C. Cheng, and Y. H. Berthelot, “Wavelet analysis of ultrasonic Lamb waves excited by pulsed laser in a composite plate,” Review of Progress in Nondestructive Evaluation, Vol. 18, edited by R. Thompson and D. Chimenti, Plenum, New York, 1999. pp. 695-701.

[37] A. Abbate, D. Klimek, P. Kotidis, and B. Anthony, “Analysis of dispersive ultrasonic signals by the ridges of the analytic wavelet transform,” Review of Progress in Nondestructive Evaluation, Vol. 18, edited by R. Thompson and D. Chimenti, Plenum, New York, 1999. pp. 703-710.

[38] B. A. Auld, Acoustic Fields and Waves in Solids, second edition, Volume I, Krieger, Malabar, Florida, 1990.

[39] M. Born and E. Wolf, Principles of Optics, Sixth edition, Pegamon Press, 1980. p. 21.

[40] A. D. Pierce, Acoustics: An Introduction to Its Physical Principles and Applications, McGraw Hill, New York, 1981. p. 128.

[41] A. D. Degtyar and S. I. Rokhlin, "Comparison of elastic constant determination in anisotropic materials from ultrasonic group and phase velocity data," J. Acoust. Soc. Am., Vol. 102 (6), 3458-3466 (1997)

[42] C. Habeger and J. Jong, "Paper A0 Signal Analysis", Institute of Paper Science and Technology, Private Communication (February 2000). A useful reference for the case of an isotropic plate is J. W. S. Rayleigh,The Theory of Sound, Second Edition, Dover, New York, Volume I, art. 188 pp. 296-297 (1945).

[43] J. Yang, J.-C. Cheng, and Y. H. Berthelot, "An inversion method to determine the elastic constants of fiber-reinforced composite plates by means of wavelet transforms and artificial neural networks" J. Acoust. Soc. Am., 111(3), 1245-1250, (2002).

[44] G. Kino , Acoustic Waves, Prentice Hall, Englewoods Cliffs, NJ)1987)

[45] F. L. Degeretekin et al., "Micromachinable ultrasonic leaky wave air transducers" Appl. Phys. Letters 73(6) 741-744 (1998)

[46] I.A. Viktorov, Rayleigh and Lamb Waves, Plenum Press, NY, 1967